9-12-2014

Intracavity coherent interaction of mode-locked pulse train with resonant medium

Koji Masuda

Koji Masuda

Candidate

Optical Science and Engineering

Department

This dissertation is approved, and it is acceptable in quality and form for publication:

Approved by the Dissertation Committee:

Jean-Claude Diels , Chairperson

Ladan Arissian

Francisco Elohim Becerra Chavez

Adam Hecht

Intracavity coherent interaction of mode-locked pulse train with resonant medium

by

Koji Masuda

B.S., Mount Union College, 2005
M.S., Optical Science and Engineering, University of New Mexico, 2010

DISSERTATION

Submitted in Partial Fulfillment of the
Requirements for the Degree of

Doctor of Philosophy
Optical Science and Engineering

The University of New Mexico

Albuquerque, New Mexico

July, 2014

Dedication

To my parents and to the memory of my Grandma Chitoshi

今日からお前は、富士山だ！　－松岡修造

Acknowledgments

Many people have helped this project in numerous ways. The names mentioned here are in no way complete and I offer my apologies to anyone who are wrongfully omitted. This work would not have been possible without the help of my advisor Prof. Jean-Claude Diels. I would like to thank him for his patience and support and for providing challenges and encouragement when they were needed. The members of my dissertation committee: Dr. Ladan Arissian, Prof. Elohim Becerra and Prof. Adam Hecht, have provided helpful input to this dissertation work through discussions and by lending equipments for my experiments. The members of my research group have all been good colleagues and have done their share in creating a nurturing work environment. In particular, I would like to mention Dr. Ladan Arissian, Dr. Andreas Schmitt-Sody and Erin Vaughan whose work is a substantial part of this dissertation. Other group members who helped me in my research are Dr. Xuan Luo, Dr. Xiaozhen Xu, Shermineh Rostami, Chengyong Feng, Amin Rasoulof, James Hendrie, Dr. Jeremy Yeak, Mikael Hosatte, Dr. Daniel Mirrel, Dr. Andreas Velten and Dr. Alex Braga. Other members of the UNM research community who have provided valuable insights through discussions and helped out with equipment are Prof. Ivan Deutsch, Dr. Peter Schwindt, Dr. Luke Emmert, Dr. Marvin Morris to name a few. Without help from John DeMoss and Anthony Gravagne of the physics machine shop, many experiments would not have been possible. Our collaborators at the Université de Neuchâtel, Gaetano Mileti and Matthew Pellaton, have prepared experimental equipments and provided data to verify the results of my experiments. Lastly, I would like to thank all of my friends who have provided tremendous support through friendship, with special thanks to Dr. Taisuke and Pricilla Ohta and Hannah Bowen.

Intracavity coherent interaction of mode-locked pulse train with resonant medium

by

Koji Masuda

B.S., Mount Union College, 2005
M.S., Optical Science and Engineering, University of New Mexico, 2010
Ph.D., Optical Science and Engineering, University of New Mexico, 2014

Abstract

Resonant interactions of a mode-locked pulse train with intracavity samples, namely rubidium-87 (^{87}Rb) vapor and Fabry-Perot etalon, placed inside a laser cavity are studied in the light of developing ultra-sensitive laser sensors to measure a small magnetic field and a minute change of index of refraction of a sample material, respectively.

A ^{87}Rb vapor provides an opportunity for a compact high-sensitivity atomic magnetometer due to its accessibility by the standard laser sources and to the large ensemble magnetization. By employing the ultra-sensitive interferometric technique utilizing the intracavity properties of a mode-locked laser, the performance of the ^{87}Rb magnetometer can be further improved. The fundamental properties of coherent interaction between a mode-locked pulse train and a ^{87}Rb vapor are studied in

numerical calculations of 3×3 density matrix equations and the reduced wave equation, which are then examined in experiments. In particular, a coherent dark-state is created by the pulse train and is further enhanced by means of spectral shaping or polarization modulation of the excitation pulse train. Experiments performed inside a laser cavity show that the atomic coherence is still preserved due to the coherent nature of interaction between the ^{87}Rb vapor and the ultrashort pulses occurred within a short time scale compared to the atomic relaxation times, which results in nonlinear propagation of the pulses as well as an observation of the dark-line resonance inside the laser cavity.

A Fabry-Perot etalon is a type of optical cavity and serves as a tuning element of the frequency of cw-lasers. By inserting a Fabry-Perot etalon inside a mode-locked laser, the cavity resonance modes are modified due to a coupling between the two cavities, which leads to unique temporal and spectral characteristics of the resultant pulse train and its frequency comb. Both the temporal and spectral properties of the pulse train are studied in detail in experiments as well as in numerical calculations. In particular, it will be shown that the coupling between low frequency modes from the laser repetition rate and high frequency modes from the Fabry-Perot pulse train can be exploited for a new interferometric technique to measure a minute change in the index of refraction of the etalon.

Contents

List of Figures

List of Tables

Glossary

E	Complete description of the electric field
P	Complete description of the polarization
$\tilde{\mathcal{E}}$	Complex electric field pulse envelope
E_0	Peak electric field amplitude
τ_s	1/e of the hyperbolic secant electric field
τ_p	FWHM of pulse intensity
p	Dipole transition
$\mathcal{W}$	Pseudo-polarization vector
ρ_{ij}	An element of the density matrix $\hat{\rho}$
Γ_{ij}	Spontaneous or collisional (incoherent) decay of the density matrix $\hat{\rho}$
σ_+	Atomic transition $m_F \rightarrow m_{F+1}$
σ_-	Atomic transition $m_F \rightarrow m_{F-1}$
m_F	Magnetic quantum number

L	Orbital angular momentum
S	Electron spin angular momentum
J	Total electron angular momentum
I	Nuclear spin angular momentum
F	Total atomic (electron + nucleus) angular momentum
n_p	Phase index of refraction
n_g	Group index of refraction

Chapter 1

Introduction

1.1 Intracavity spectroscopy

1.1.1 Absorption measurement

Exploitation of the highly sensitive response of a laser spectrum to an intracavity resonant medium began in the early times of laser development. The first demonstrations of intracavity absorption spectroscopy were performed by placing an absorbing gas inside a dye laser [6, 7]. Strong extinction of spectral components that overlap with an atomic absorption line was observed. An enhancement of sensitivity by several orders of magnitude compared to extracavity spectroscopic techniques was demonstrated. The underlying principle of absorption spectroscopy is the existence of a multi-path configuration inside a cavity, which effectively increases the length of the absorber. Due to a homogeneously broadened gain medium, the spectral power lost in the absorber is distributed to surrounding modes, leaving a distinct fingerprint in the resultant laser spectrum (Figure 1.1) [1].

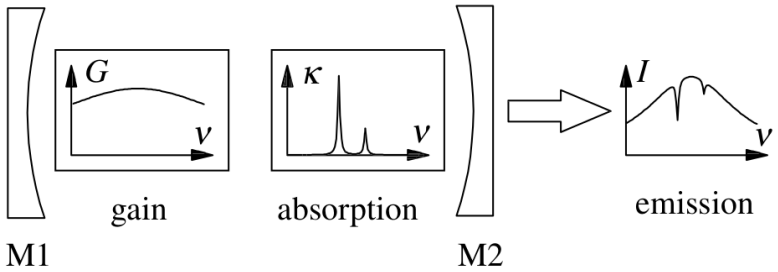

Figure 1.1: Concept of intracavity absorption spectroscopy. Borrowed from [1]

1.1.2 Phase measurement

The finite response time of the dipole oscillation implies that there is an associated dispersion, which is a necessary consequence of causality. Mathematically, the real and imaginary parts of the electronic susceptibility are related through the Kramers-Kronig relations [8].

The response of the laser to an intracavity absorber is therefore not only limited to the extinction of certain spectral components, but is also observed in terms of the phase response. In the presence of an intracavity dispersive medium, the cavity round-trip phase of a mode of the laser is modified according to [9]

$$\varphi(\Omega) = \frac{\Omega P}{c} \times \left[1 + \frac{d}{2P}\chi'(\Omega)\right] = 2m\pi \tag{1.1}$$

where P is the perimeter of the cavity, d is the length of the dispersive medium, χ' is the real part of susceptibility, c is speed of light and m is an integer. Therefore, depending on the magnitude of χ', the frequency is adjusted to keep the resonance condition.

It is this property of lasers that will be exploited for an ultra-sensitive phase spectroscopic sensor. It should also be noted that measurement of the frequency shift employs heterodyne detection to measure a beat frequency between the shifted and reference frequencies. As in the case of frequency-modulation (FM) radio signals,

which are less noisy than amplitude-modulation (AM) radio signals, the measurement is based on change in frequency rather than amplitude.

1.2 Mode-locked laser for sensing

1.2.1 Frequency comb

A mode-locked laser generates a broadband spectrum with a comb-like mode structure arising from a periodic train of ultrashort pulses, known as the frequency comb [10]. To understand the properties of the frequency comb, let us begin with the construction of a train of ultrashort pulses. With an envelope of a single pulse defined as $\tilde{\mathcal{E}}(t) = \mathcal{E}(t)\exp(i\varphi_e)$, a carrier frequency ω_ℓ and a delay between successive pulses τ_{RT}, a pulse train can be expressed as

$$\begin{aligned} E_{\text{train}} &= \sum_{q=0}^{\infty} \tilde{\mathcal{E}}(t - q\tau_{RT}) e^{i\omega_\ell (t - q\tau_{RT})} \\ &= e^{i\omega_\ell t} \sum_{q=0}^{\infty} \tilde{\mathcal{E}}(t - q\tau_{RT}) e^{-iq\omega_\ell \tau_{RT}} \\ &= e^{i\omega_\ell t} \sum_{q=0}^{\infty} \tilde{\mathcal{E}}(t - q\tau_{RT}) e^{-iq(2N\pi - \varphi_p)} \end{aligned} \tag{1.2}$$

where $\omega_\ell \tau_{RT} = 2N\pi - \varphi_p$ has been substituted to obtain the laser equation. The Fourier transform of the first pulse ($q = 0$) of the pulse train defined in Eq. (1.2) is

$$\tilde{E}(\Omega) = \int_{-\infty}^{\infty} \tilde{\mathcal{E}}(t) e^{-i\Omega t} e^{i\omega_\ell t} dt = \tilde{\mathcal{E}}(\Omega - \omega_\ell) \tag{1.3}$$

and for the q-th pulse, delayed by $q\tau_{RT}$,

$$\tilde{E}_q(\Omega) = \tilde{\mathcal{E}}(\Omega - \omega_\ell) e^{-iq\tau_{RT}(\Omega - \omega_\ell)} \tag{1.4}$$

Summing over q, the infinite series of imaginary exponentials leads to a comb of evenly spaced delta-functions (Dirac comb),

$$\tilde{E}(\Omega) = \tilde{\mathcal{E}}(\Omega - \omega_\ell) \sum_{p=-\infty}^{\infty} \delta\left[\Omega - \omega_\ell - \frac{2p\pi}{\tau_{RT}}\right] \tag{1.5}$$

Since $\omega_\ell \tau_{RT} = 2N\pi - \varphi_p$, the spectral locations of the delta functions are given by

$$\begin{aligned} \Omega_m &= \frac{1}{\tau_{RT}}(2N\pi - \varphi_p + 2p\pi) \\ &= \frac{1}{\tau_{RT}}(2m\pi - \varphi_p) \end{aligned} \tag{1.6}$$

where $m = N+p$. The last equation Eq. (1.6) indicates that the modes of a frequency comb can be completely specified in terms of the mode spacing f_{rep} and an offset f_0 as

$$f_m = f_0 + m f_{rep} \tag{1.7}$$

where

$$f_{rep} = \frac{1}{\tau_{RT}} \quad : \text{Repetition rate} \tag{1.8}$$

$$f_0 = \frac{\Delta\varphi}{2\pi\tau_{RT}} \quad : \text{Carrier to envelope offset (CEO)} \tag{1.9}$$

Notice that the modes in a frequency comb is fully specified by only two parameters, f_0 and f_{rep}. The "carrier-to-envelope phase", $\Delta\varphi$, arises because of the difference between the group and phase velocity in the cavity. Therefore, the carrier-to-envelope offset frequency, f_0, can be expressed as

$$f_0 = \frac{\Delta\varphi}{2\pi\tau_{RT}} = \frac{\left(\frac{1}{v_g} - \frac{1}{v_p}\right)\omega_\ell P}{2\pi\tau_{RT}} = \frac{(n_g - n_p)\,\omega_\ell P/c}{2\pi\tau_{RT}} \tag{1.10}$$

where P is the perimeter of the cavity, and n_g and n_p are respectively the group and phase index of refraction of the cavity. A pictorial description of a frequency comb is shown in Figure 1.2.

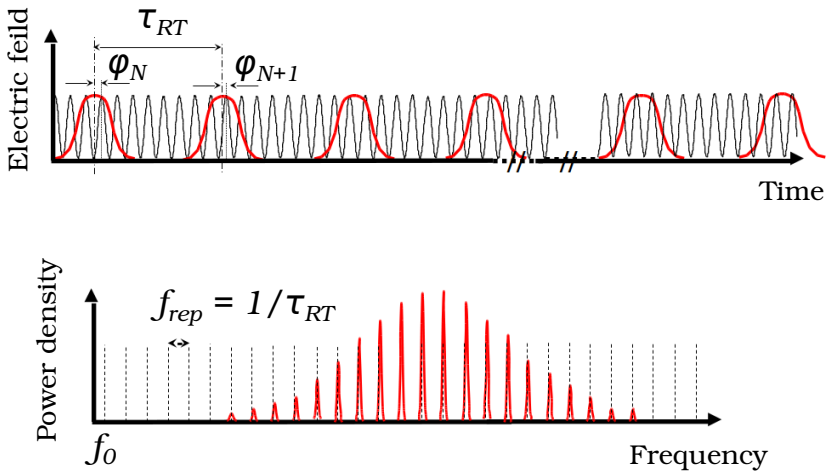

Figure 1.2: A round-trip phase slippage, $\Delta\varphi$, between the pulse envelope and the carrier frequency in time domain results in the carrier-to-envelope offset frequency, f_0, in frequency domain. The mode spacing is determined by the repetition rate of the pulse train, f_{rep}.

1.2.2 Advantages of mode-locked lasers over free-running lasers

By utilizing the broadband spectrum and the resolved individual modes of the frequency comb, a simultaneous detection of resonance structures of multiple molecular species has been demonstrated based on intracavity absorption measurements [11]. As discussed earlier in Section 1.1, the near-resonance dispersion of an intracavity medium also modifies the resonance condition of the cavity, which results in a shift of the modes of the frequency comb. For a frequency comb where there is a fixed phase between the modes, *all* modes are shifted by the same amount determined by the carrier-to-envelope offset f_0. This property provides a tremendous advantage over measurements based on free-running lasers, as following. A train of ultrashort (ps $\sim$ fs) pulses with the repetition rate of the order of 100 MHz contains as many as $10^4 \sim 10^6$ optical modes in its spectrum. By employing a heterodyne detection against a reference frequency comb with the same mode spacing, but with f_0 not nec-

essarily equal, all the pairs of modes contribute to a single beat frequency. Therefore, the signal-to-noise ratio is significantly increased.

1.2.3 Intracavity phase interferometry (IPI)

The remarkable property of the frequency comb that all the modes are strictly evenly spaced by f_{rep} and shifted by f_0, which completely characterize a frequency comb as in Eq. (1.7), can be exploited for an ultra-sensitive measurement of a differential intracavity phase shift.

Suppose there is a laser cavity in which two pulses are counter-propagating, sharing the same cavity perimeter. When mode-locking is realized by a saturable absorber, the two counter propagating pulses cross each other at the saturable absorber, and mutually saturate the absorption. It is a known fact that the mutual saturation couples the envelopes of the counter propagating pulses and locks their average group velocity in the cavity, or equivalently the group index of refraction of the cavity n_g [12].

Now, suppose there is an intracavity element with length d and different phase indices of refraction n_p between clock-wise (CW) and counter-clock wise (CCW) propagation directions. Since the group indices of refraction are locked between the CW and CCW pulse trains, the difference in the phase index of refraction results in frequency combs with different f_0 but with the same mode spacing, f_{rep}, according to Eq. (1.10). As shown in Figure 1.3, when both pulse trains are picked out from the cavity and overlapped on a photodetector, after a proper delay the beat frequency between the pulse trains is generated:

$$\Delta\nu = f_{01} - f_{02} = \frac{(n_{p1} - n_{p2})d}{\lambda_\ell \tau_{RT}} \tag{1.11}$$

where λ_ℓ is the carrier wavelength. Therefore, the beat note carries the information about the phase shift between the CW and CCW pulse trains.

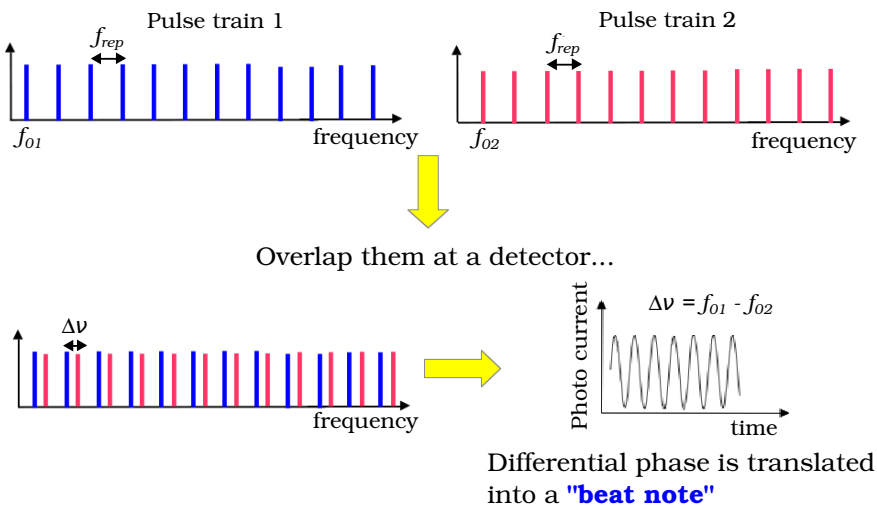

Figure 1.3: The differential phase shift between the CW and CCW pulse train sharing the same cavity results in a beat note when they are overlapped on a photodetector.

This is a novel interferometric technique, known as the intracavity phase interferometry (IPI). IPI has been demonstrated to measure electro-optic coefficients, a nonlinear index of refraction [13] and birefringence of circular polarization due to an applied magnetic field [2], which is described next.

Demonstration of IPI for magnetic field sensing using a crystal

The Faraday effect is a magneto-optical phenomenon that rotates the polarization plane of a linearly polarized beam propagating in a medium under a magnetic field. The angle of polarization rotation ϕ is proportional to the magnetic flux along the beam propagation direction:

$$\phi = VBd \tag{1.12}$$

where V is the Verdet constant given in unit of degree per unit length per magnetic flux density and B is the magnetic flux density along the direction of beam

propagation. The physical origin of the Faraday effect is a differential phase shift between left-circular polarization (LCP) and right-circular polarization (RCP) in an anisotropic medium possessing non-zero net magnetization.

An IPI magnetic sensor using a magnetizable crystal has been demonstrated as a proof-of-principle experiment for IPI magnetometry [2]. In this experiment, a Terbium Gallium Garnet (TGG) which is a common material for optical isolators with Verdet constant of $4.5 \times 10^3\ ^\circ T^{-1}$, is placed between two quarter-wave plates ($\lambda/2$) in a ring titanium-sapphire mode-locked laser cavity, as shown in Figure 1.4. The laser is designed to have two counter propagating pulse trains with crossing points made once at a saturable absorber and another time in air a half way around the cavity. With one half-wave plate at a set position and two quarter-wave plates at both sides of the TGG crystal, the counter propagating pulses become LCP and RCP at the crystal.

In the presence of a current in the solenoid, a non-zero net magnetization of the crystal causes a differential phase shift between LCP and RCP. The beat note generated by overlapping the two pulse trains is given by

$$\Delta\nu = \frac{\Delta\varphi}{2\pi\tau_{rt}} = \frac{VB\ell}{(180^\circ)\tau_{rt}} \tag{1.13}$$

As shown in right panel in Figure 1.4, a linear relationship between the magnetic field and the beat-note has been measured, as expected. The slope agrees with the listed Verdet constant, and the resolution of the apparatus is measured to be 30 nT/Hz, which corresponds to 8×10^{-9} rad.

Ultra-sensitive IPI magnetometer using atomic sample

A proof of principle experiment for IPI magnetometry using a magnetized crystal demonstrates the superb performance of the IPI magnetometry scheme. Further

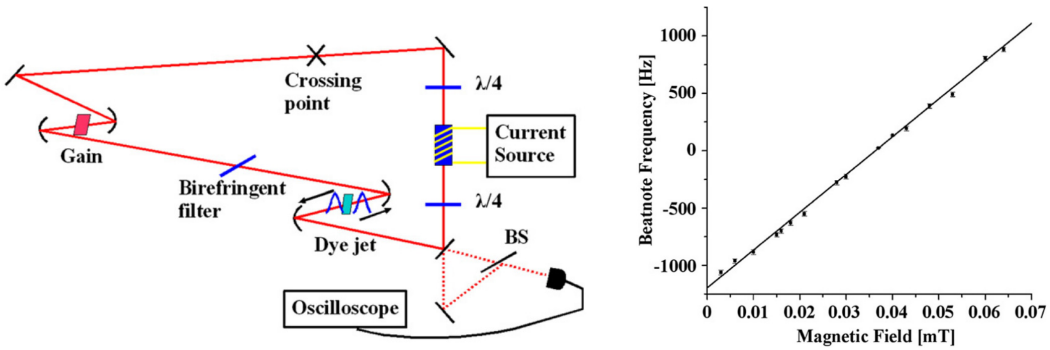

Figure 1.4: Left: Experimental setup for IPI magnetometry using a TGG crystal (a blue rectangle with yellow lines). Left: a measurement of beat frequency as a function of magnetic field [2].

improvement of the sensitivity of an IPI magnetometer can be achieved with an atomic vapor which has orders of magnitude larger Verdet constant compared to the crystal sample.

The basic principle of atomic magnetometers is based on creating a net spin polarization of an atomic ensemble by near-resonant light and subsequently measuring the absorptive or dispersive response of a spin precession of the ensemble under a magnetic field [14]. The study of responses of a precessing atomic ensemble to near-resonant light field has a long history, starting with the pioneering work by Dehmelt [15] and Bell and Bloom [16, 17].

One of the requirements for operating an ultra-high sensitivity atomic magnetometer is to create a long-lived ground state coherence. There are various types of atomic magnetometers operating on different physical principles including coherent population trapping (CPT) magnetometers [18, 19] and spin-exchange relaxation free (SERF) [20] magnetometers. The CPT magnetometers exploit a sharp resonance of a long-lived coherent dark-state formed between field-sensitive Zeeman sublevels. The SERF magnetometers make use of a counter-intuitive property of a high density vapor where sufficiently rapid spin-exchange collisions increases the ground state

coherence.

The ultimate sensitivity of atomic magnetometers when measurement is performed for a time T with a vapor of volume V, density n with coherence time τ is given by [14]

$$\delta B \simeq \frac{1}{g\mu_B}\frac{\hbar}{\sqrt{nV\tau T}} \tag{1.14}$$

where μ_B is the Bohr magneton, g is the ground state Landé factor, and $\hbar$ is the Planck's constant. Atomic magnetometers with sensitivity reaching sub-femtotesla level have been demonstrated [21].

Higher sensitivity is usually obtained in experiments based on the dispersive response of an atomic polarization, which can be measured by the rotation of polarization or by an interferometric detection [22]. Since an atomic polarization exhibits circular birefringence, it is feasible that IPI magnetometry provides an opportunity for constructing an ultra-sensitive atomic magnetometer, which could in principle exceed the performance of current state-of-the-art atomic magnetometers.

1.2.4 Intracavity measurement of refractive index in a coupled cavity mode-locked laser

In the latter half of this dissertation, studies of a new class of coupled-cavity mode-locked laser system will be presented. The novelty of the new coupled-cavity mode-locked laser system is an intricate structure of the frequency comb generated through a coupling of two cavities, namely an intracavity Fabry-Perot etalon and the laser cavity. Since the lengths of the two cavities are different, the resultant comb is composed of two different mode spacings. In addition, due to time-dependent gain of the oscillator and due to the coupling of the resonance modes, the mode spacings are coupled in counter-intuitive fashion. Despite those complications, however, it can

be shown that it is possible to extract information about relative changes between two cavities based on the fact that the modes are simultaneously resonant with both cavities. An example of such measurement would be a measurement of small changes of the index of refraction of the Fabry-Perot etalon.

1.3 Scope of this dissertation

As mentioned, the responses of mode-locked lasers to an intracavity phase perturbation provides tremendous advantages for the frequency measurements, as oppose to the traditional measurement of amplitude changes. The general motivation of this dissertation is to perform fundamental studies towards realization of an ultra-sensitive intracavity laser sensor based on the frequency measurement of an intracavity differential phase shift. In particular, two systems are investigated: one is a mode-locked laser with ^{87}Rb atoms for the development of an ultra-sensitive magnetometer based on the IPI technique, and the other one is a coupled cavity mode-locked laser for a measurement of a minute change in the index of refraction of an intracavity Fabry-Perot etalon. In both cases, the sensitivity of the system is enhanced because of the near-resonance feature of the respective media.

This dissertation is organized as following. In Chapter 2, the repetition rate spectroscopy of coherent population trapping (CPT) of a ^{87}Rb vapor, including the response of the CPT resonance to a magnetic field in different geometry is presented. In Chapter 3, a method to enhance the CPT signal contrast via spectral shaping is presented. Observation of shifted CPT resonance is discussed. Chapter 4 is dedicated to experimental investigations of the dynamical pumping of the CPT resonance by sending a pulse train with alternating circular polarization, which simulates the interaction scheme of an IPI magnetometer. Intracavity experiments of coherent propagation of ultrashort pulses in a ^{87}Rb vapor is presented in Chapter 5. Ob-

servation of the CPT resonance excited by an intracavity pulse train is discussed. Lastly, detailed studies of a new type of frequency comb, which is discovered during experiments presented in Chapter 3, are presented in Chapter 6. A potential application for the measurement of minute changes in the index of refraction of a sample is discussed.

Chapter 2

Coherent population trapping of ^{87}Rb using a mode-locked laser

2.1 Introduction

The ground state in alkali-metal atoms, including sodium (Na), potassium (K), rubidium (Rb) and cesium (Cs), has two hyperfine states [5, 23]. Together with an excited state connected by a dipole transition a so-called Λ-system, due to its shape, is formed [24]. The significance of the Λ-system is a narrow resonance of the ground state hyperfine transition, which can be induced by a two-photon process. The narrow resonance is the consequence of both the absence of a direct electric dipole transition between the hyperfine states and the Doppler-free configuration. The Λ-system of the ground state alkali metal atoms has been extensively exploited for precision atomic spectroscopy [25], metrology [26, 27] and in various applications of nonlinear optics [28, 29, 30, 31]. The narrow resonance of the ground state hyperfine transition also offer opportunities for implementing high-precision frequency standards [26] and high-sensitivity optical magnetometers [22].

Traditionally, the ground state hyperfine transition is induced by applying a resonant microwave to excite a magnetic dipole [32]. Since the invention of the laser, optical excitation via two-photon transition has become an alternative approach [33]. In both cases, a strong coherence between the ground states is induced at the resonance. The optical approach is especially known as the phenomenon of coherent population trapping (CPT). In CPT, the optically resonant fields applied on the two optical transitions of the Λ system cause an inherent quantum destructive interference of the transitions, leaving the atoms in the ground state coherence [25]. The CPT resonance occurs when the difference frequency of the applied fields matches the ground state hyperfine splitting. Since a direct dipole transition between the ground states is forbidden, the coherence established between the ground state levels last for a long time, leading to a very narrow resonance feature.

Recently, CPT of alkali-metal atomic vapor has drawn a great deal of attentions due to combined benefit of its accessibility with inexpensive laser sources which can be sufficiently stabilized without significant effort [34, 35, 36] and the potential for miniaturization for field applications. High performance chip-scale atomic clocks [37] and magnetometers [19] have been demonstrated.

On the other hand, it is interesting to realize that the first experimental demonstration of CPT was performed with a multi-mode laser [33]. Experimental demonstration of CPT by means of pulsed excitation was performed by applying a Q-switched pulse train to a sodium (Na) vapor [38]. The pulse width was sufficiently short such that the pulse spectrum overlaps with both the ground states to induced coherence between them. The resonance was observed when the repetition rate of the laser matched to a submultiple (i.e. $1/N$ where $N = 1, 2, \cdots$) of the ground state sodium hyperfine splitting.

In the late 1990's it was discovered that a mode-locked laser generated a so-called frequency comb. The extraordinary properties of the frequency comb include

the strictly equally spaced modes and their well-defined absolute positions [10]. The frequency comb technology has then revolutionized the field of optical metrology as it directly links optical frequency to radio frequency [39, 40]. Since then, efforts to combine the best of the narrow resonance of CPT and the frequency comb technology have been made. A theoretical analysis showed that when the period between subsequent pulses was shorter than the relaxation time of the ground state coherence, the atomic coherence accumulates over interaction with many pulses[41]. An experimental demonstration using a picosecond mode-locked laser and a ^{87}Rb vapor was also preformed [42]. The authors identified that the CPT linewidth depended on the experimental parameter "area" but not on the phase of the individual pulses. Using this property, the authors proposed a potential application to auto-stabilization of the repetition rate.

In this chapter, a previously demonstrated method to establish CPT in a ^{87}Rb vapor using a frequency comb, which is known as the repetition rate spectroscopy [42], is briefly reviewed. Also, CPT with a frequency comb also has an advantage that it can be integrated into the IPI scheme, as described in chapter 1. Therefore, for a potential application for an ultra-sensitive magnetometry based on the IPI technique, the responses of the CPT resonance to an applied magnetic field is also investigated.

2.2 Representation of ^{87}Rb vapor

2.2.1 Rubidium-87 isotope

Rubidium can be found in the leftmost column on the periodic table, a member of alkali metal atoms including Li, Na, K, Cs. Rubidium has 37 electrons, one of which is an unpaired valence electron. There are two naturally occurring rubidium isotopes; ^{85}Rb (72.2% in natural abundance) which is stable and ^{87}Rb (27.8% in

natural abundance) which is weakly radioactive. Both isotopes provide a platform for CPT experiments. In this work, CPT of ^{87}Rb atoms is studied.

2.2.2 Energy structure of ^{87}Rb atoms

Coarse value of the lowest energy of ^{87}Rb atoms is determined by the distance between the nucleus to the orbit of the valence electron. Because of the quantum nature of the electron orbit, the electron can only take discrete values of energy E_n where n is the principle quantum number ($n = 5$ for the valence electron of ground-state ^{87}Rb).

The next coarse assignment of the energy arises due to the coupling of the electron orbital angular momentum L and spin angular momentum S, known as the fine structure [43]. The vector nature of angular momentum allows the total electron angular momentum to be represented as a vector sum:

$$J = L + S \tag{2.1}$$

The upper-bound and lower-bound of the values of J are given by

$$|L - S| \geq J \geq L + S \tag{2.2}$$

Moreover, the quantum nature of the angular momentum restricts the values of J to be discrete. For example, when $L = 0$ and $S = 1/2$, the total angular momentum takes only one value: $J = 1/2$. For $L = 1$ and $S = 1/2$, there are two values of J: $J = 1/2$ and $J = 3/2$. These different energy states are labelled by an alphabet and numbers to indicated the angular momentum. An alphabet represents the value of L: S for $L = 0$, P for $L = 1$, D for $L = 2$, and so on. The ground state ^{87}Rb, where $L = 0$ and $J = L + S = 1/2$, is denoted as $5S_{1/2}$ where the first number represents the principle quantum number n and the subscript represents the value of J.

The first two excited states are in the P-orbital with $J = 1/2$ and $J = 3/2$, or using the short-hand notation just introduced, $5P_{1/2}$ and $5P_{3/2}$. The transition from the ground state to the first P-orbital ($5S_{1/2} \rightarrow 5P_{1/2}$) is induced by exciting an electric dipole with light at 795 nm (377 THz), which is dubbed the D1 line. The transition to the second P-orbital ($5S_{1/2} \rightarrow 5P_{3/2}$), dubbed the D2 line, is excited at 780 nm (384 THz). Since the fine structure splitting of ^{87}Rb , which is approximately 15 nm, is large enough to be resolved by many lasers including picosecond mode-locked lasers, D1 and D2 transitions are treated separately. Throughout this dissertation, only the interaction of light with the D1 line is considered.

Each of the fine structure is further split due to the coupling of the nuclear spin I and the electron spin S, known is the hyperfine structure. The total angular momentum of the atomic system is then given by

$$F = I + J \tag{2.3}$$

The values of F are separated by integer steps in the range given by

$$|J - I| \geq F \geq J + I \tag{2.4}$$

For ^{87}Rb, $I = 3/2$. Thus, for example, the ground state ^{87}Rb where $J = 1/2$, the total atomic angular momentum takes two values, $F = 1$ and $F = 2$. Similarly, $5P_{1/2}$ state has two hyperfine states with $F = 1$ and $F = 2$.

The Hamiltonian describing the hyperfine structure in the D1 line is [5]:

$$H_{fhs} = A_{hfs} I \cdot J, \tag{2.5}$$

and the corresponding energy splitting is given by

$$\Delta E_{hfs} = \frac{1}{2} A_{hfs} K \tag{2.6}$$

where

$$K = F(F + 1) - I(I + 1) - J(J + 1)) \tag{2.7}$$

where A_{hfs} is the magnetic dipole constant. The values of A_{hfs} for $5S_{1/2}$ and $5P_{1/2}$ are listed in Table 2.1. The hyperfine splitting of $5S_{1/2}$ state is 6.834 GHz, while that of $5P_{1/2}$ is 0.814 GHz. The energy diagram of the D1 line of ^{87}Rb is shown in Figure 2.1.

Magnetic dipole constant, $5S_{1/2}$	$A_{5S_{1/2}}$	$h \cdot 3.417\ 341\ 305\ 452\ 145(45)$ GHz
Magnetic dipole constant, $5P_{1/2}$	$A_{5P_{1/2}}$	$h \cdot 404.24(77)$ MHz

Table 2.1: Rubidium 87 D1 transition hyperfine structure constants.

2.2.3 Simplification to a Λ-system

In an atomic vapor ^{87}Rb atoms, each homogeneously broadened energy level is further broadened due to the Doppler broadening. The Doppler width at room temperature is approximately 500 MHz [43]. In the inhomogeneously broadened rubidium vapor, the ground state hyperfine levels separated by 6.834 GHz are well resolved, as can be seen in Figure 2.1. On the other hand, the excited hyperfine states separated by 814 MHz are only partially resolved. Strictly speaking, a ^{87}Rb vapor at room temperature is thus a four-level system. However, a numerical calculation for CPT in a four-level ^{87}Rb shows that an inclusion of the second excited state does not significantly change the basic principle of the phenomenon [44]. Therefore, in the analysis treated in this chapter and in the rest of this dissertation, the D1 line is reduced to a simple three-level system where there are two ground state hyperfine states and a single excited state, forming a Λ-system, as shown in the right figure in Figure 2.1. The name Λ-system comes from the shape of the transition schematic, as in Figure 2.3.

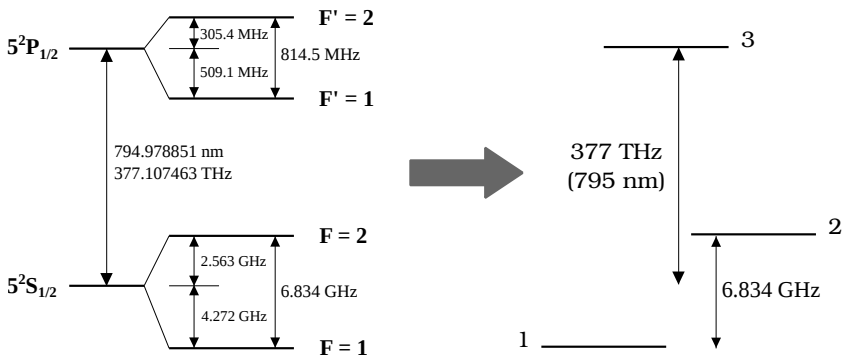

Figure 2.1: Energy diagram of D1 line. A ^{87}Rb vapor at room temperature can be simplified to a Λ-system.

2.3 Interaction with mode-locked pulses

2.3.1 Density matrix representation of a Λ-system

Interactions of an ensemble of quantum systems with optical fields are conveniently described by the time evolution of the density matrix due to the energy transported by the fields. An ensemble of three-level atoms is represented by a 3×3 density matrix [45],

$$\hat{\rho} = \begin{pmatrix} \rho_{11} & \tilde{\rho}_{12} & \tilde{\rho}_{13} \\ \tilde{\rho}_{21} & \rho_{22} & \tilde{\rho}_{23} \\ \tilde{\rho}_{31} & \tilde{\rho}_{32} & \rho_{33} \end{pmatrix} \tag{2.8}$$

The diagonal elements ρ_{ii} represent atomic population in the energy level $|i\rangle$ and the off-diagonal elements $\tilde{\rho}_{ij}$ represent coherence between the two energy levels $|i\rangle$ and $|j\rangle$ which are written in a complex form. Time evolution of $\hat{\rho}$ is given by the Liouville-von Neumann equation:

$$\frac{d\hat{\rho}}{dt} = -\frac{i}{\hbar}\left[\hat{H}, \hat{\rho}\right] + \hat{\mathcal{R}}\hat{\rho} \tag{2.9}$$

where $\hat{\mathcal{R}}$ represents relaxation processes of the density matrix elements. The total evolution Hamiltonian, $\hat{H} = \hat{H}_0 + \hat{H}_{int}$, consists of an unperturbed atomic Hamilto-

nian $\hat{H}_0$ and a dipole interaction Hamiltonian $\hat{H}_{int}$ [45]:

$$\hat{H}_0 = \sum_i \hbar\omega_i \left|i\right\rangle \left\langle i\right| \tag{2.10a}$$

$$\hat{H}_{int} = \sum_{i\neq j} \left\langle i\right| \left(-\hat{p}\cdot\tilde{E}\right) \left|j\right\rangle \left|i\right\rangle \left\langle j\right| = -\sum_{i\neq j} V_{ij} \left|i\right\rangle \left\langle j\right| \tag{2.10b}$$

where $\hbar\omega_i$ is the eigenenergy of i state, p_{ij} is a dipole moment of the transition between i and j states and $V_{ij} = p_{ij}\tilde{E}$.

Calculating Eq. (2.9) with Eq. (2.10), the differential equations for each matrix element are found as

$$\begin{aligned}
\frac{d\rho_{11}}{dt} &= -\frac{i}{\hbar}(\tilde{V}_{31}^*\tilde{\rho}_{21} - \tilde{\rho}_{31}^*\tilde{V}_{31}) + \frac{\Gamma_3}{2}\rho_{33} \\
&= -\frac{2p_{31}}{\hbar}\mathrm{Im}(\tilde{E}^*\tilde{\rho}_{31}) + \frac{\Gamma_3}{2}\rho_{33} && (2.11a)\\
\frac{d\rho_{22}}{dt} &= -\frac{i}{\hbar}(\tilde{V}_{32}\tilde{\rho}_{32}^* - \tilde{\rho}_{32}\tilde{V}_{32}^*) - \frac{\Gamma_3}{2}\rho_{33} \\
&= \frac{2p_{32}}{\hbar}\mathrm{Im}(\tilde{E}^*\tilde{\rho}_{32}) - \frac{\Gamma_3}{2}\rho_{33} && (2.11b)\\
\frac{d\rho_{33}}{dt} &= \frac{2p_{31}}{\hbar}\mathrm{Im}(\tilde{E}^*\tilde{\rho}_{31}) + \frac{2p_{32}}{\hbar}\mathrm{Im}(\tilde{E}^*\tilde{\rho}_{32}) - \Gamma_3\rho_{33} && (2.11c)\\
\frac{d\tilde{\rho}_{21}}{dt} &= -i(\omega_2-\omega_1)\tilde{\rho}_{21} + i\frac{\tilde{V}_{32}^*}{\hbar}\tilde{\rho}_{31} - i\frac{\tilde{V}_{31}}{\hbar}\tilde{\rho}_{32}^* - \Gamma_{21}\tilde{\rho}_{21} \\
&= -i\omega_{21}\tilde{\rho}_{21} - i\frac{\tilde{p}_{31}\tilde{\mathcal{E}}}{\hbar}\tilde{\rho}_{32}^* + i\frac{\tilde{p}_{32}\tilde{\mathcal{E}}^*}{\hbar}\tilde{\rho}_{31} - \Gamma_{21}\tilde{\rho}_{21} && (2.11d)\\
\frac{d\tilde{\rho}_{31}}{dt} &= -i(\omega_3-\omega_1)\tilde{\rho}_{31} - i\frac{V_{31}}{\hbar}(\rho_{33}-\rho_{11}) + i\frac{\tilde{V}_{32}}{\hbar}\tilde{\rho}_{21} - \Gamma_{31}\tilde{\rho}_{31} \\
&= -i\omega_{31}\tilde{\rho}_{31} - i\frac{p_{31}\tilde{\mathcal{E}}}{\hbar}(\rho_{33}-\rho_{11}) + i\frac{\tilde{p}_{32}\tilde{\mathcal{E}}}{\hbar}\tilde{\rho}_{21} - \Gamma_{31}\tilde{\rho}_{31} && (2.11e)\\
\frac{d\tilde{\rho}_{32}}{dt} &= -i(\omega_3-\omega_2)\tilde{\rho}_{31} - i\frac{V_{32}}{\hbar}(\rho_{33}-\rho_{22}) + i\frac{\tilde{V}_{31}}{\hbar}\tilde{\rho}_{21}^* - \Gamma_{32}\tilde{\rho}_{32} \\
&= -i\omega_{32}\tilde{\rho}_{32} - i\frac{p_{32}\tilde{\mathcal{E}}}{\hbar}(\rho_{33}-\rho_{22}) + i\frac{\tilde{p}_{31}\tilde{\mathcal{E}}}{\hbar}\tilde{\rho}_{21}^* - \Gamma_{32}\tilde{\rho}_{32} && (2.11f)
\end{aligned}$$

where Γ_i are the relaxation rate of population in $|i\rangle$ and Γ_{ij} are the relaxation rate

of coherence between $|i\rangle$ and $|j\rangle$. The following operations are also made; $\mathrm{Im}(z) = -i(z - z^*)/2$ and $\omega_{ij} \equiv \omega_i - \omega_j$.

Since the time evolution of the system occurs in a time scale much longer than optical oscillation, the electric field $\tilde{E}$ and the matrix elements $\tilde{\rho}_{31}$ and $\tilde{\rho}_{32}$ can be expressed in terms of their slowly varying envelope and the rapidly varying term oscillating at ω_ℓ of the laser frequency:

$$\tilde{\rho}_{31} = \frac{1}{2}\tilde{\sigma}_{31}e^{i\omega_\ell} \tag{2.12}$$

$$\tilde{\rho}_{32} = \frac{1}{2}\tilde{\sigma}_{32}e^{i\omega_\ell} \tag{2.13}$$

$$\tilde{E} = \frac{1}{2}\tilde{\mathcal{E}}e^{i\omega_\ell} \tag{2.14}$$

This transformation, known as the rotating wave approximation (RWA) [46], eliminates the fast oscillating terms from the differential equations, Eq. (2.11):

$$\frac{d\rho_{11}}{dt} = -\frac{\kappa}{2}\mathrm{Im}(\tilde{\mathcal{E}}^*\tilde{\sigma}_{31}) + \frac{\Gamma_3}{2}\rho_{33} \tag{2.15a}$$

$$\frac{d\rho_{22}}{dt} = -\frac{\kappa}{2}\mathrm{Im}(\tilde{\mathcal{E}}^*\tilde{\sigma}_{32}) + \frac{\Gamma_3}{2}\rho_{33} \tag{2.15b}$$

$$\frac{d\rho_{33}}{dt} = \frac{\kappa}{2}\mathrm{Im}(\tilde{\mathcal{E}}^*\tilde{\sigma}_{31}) + \frac{\kappa}{2}\mathrm{Im}(\tilde{\mathcal{E}}^*\tilde{\sigma}_{32}) - \Gamma_3\rho_{33} \tag{2.15c}$$

$$\frac{d\tilde{\sigma}_{31}}{dt} = (-\Gamma_{31} - i\Delta_{13})\tilde{\sigma}_{31} - i\kappa\tilde{\mathcal{E}}(\rho_{33} - \rho_{11}) + i\kappa\tilde{\mathcal{E}}\tilde{\rho}_{21} \tag{2.15d}$$

$$\frac{d\tilde{\sigma}_{32}}{dt} = (-\Gamma_{32} - i\Delta_{23})\tilde{\sigma}_{32} - i\kappa\tilde{\mathcal{E}}(\rho_{33} - \rho_{22}) + i\kappa\tilde{\mathcal{E}}\tilde{\rho}^*_{21} \tag{2.15e}$$

$$\frac{d\tilde{\rho}_{21}}{dt} = (-\Gamma_{21} - i\Delta_{12})\tilde{\rho}_{21} - i\frac{\kappa}{4}\tilde{\mathcal{E}}^*\sigma_{31} - i\frac{\kappa}{4}\tilde{\mathcal{E}}\tilde{\sigma}^*_{32} \tag{2.15f}$$

where $\kappa = p_{ij}/\hbar$ and $\Delta_{ij} = \omega_{ij} - \omega_\ell$ is detuning between the optical frequency and the corresponding atomic resonance. $\kappa\tilde{\mathcal{E}}$ is identified as the Rabi frequency.

2.3.2 CPT via resonant repetition rate

The evolution of the density matrix elements in Eq. (2.15) can be solved numerically. For excitation with a pulse train, the electric field $\mathcal{E}$ is given a standard pulse envelope

function. A pulse train is simulated by giving a proper time period between the pulse envelopes, τ_{RT}. A detailed analysis of the roles of various parameters appearing in Eq. (2.11) has been presented in ref. [44]. In the following paragraphs, the main results from the aforementioned reference are summarized.

Dark-line resonance

One of the important results is the observation of a dark-line resonance occurred when the mode spacing of a frequency comb is brought into resonance. The left panel in Figure 2.2 shows a result of numerical integration of Eq. (2.15) as a function of pulse period τ_{RT}. When the inverse of the pulse interval becomes equal to a submultiple of the ground state hyperfine splitting, the probability of atoms to be in the excited state, ρ_{33}, is significantly reduced. The resonance is observed as a reduction of fluorescence, thus named dark-line resonance.

The physical origin of the dark-line resonance is a creation of a coherent superposition of the ground state hyperfine states [25]. In the dressed atom basis [45], the dark-state can be expressed as $|\psi\rangle$:

$$|\psi\rangle = \frac{p_{31}\mathcal{E}_1 |1\rangle - p_{32}\mathcal{E}_2 |2\rangle}{\sqrt{|p_{31}\mathcal{E}_1|^2 + |p_{32}\mathcal{E}_2|^2}} \tag{2.16}$$

where $\mathcal{E}_1$ and $\mathcal{E}_2$ are the electric field components corresponding to the transitions from each ground state to the excited state. It is easy to show that this superposition state $|\psi\rangle$ has a vanishing eigenvalue for the Hamiltonian in Eq. (2.10). Physically, the simultaneous excitations with the near-resonant optical fields, represented as $\mathcal{E}_1$ and $\mathcal{E}_2$, cause an interference of the probability amplitudes of the dipole transitions induced by the fields. When the difference frequency of the two fields matches the ground state hyperfine splitting, $\omega_1 - \omega_2 = \Delta_{12}$, a destructive interference of the probability amplitudes occurs, and the excited state population vanishes; the atoms are said to be coherently "trapped" in the ground state. Thus, the name coherent

population trapping (CPT) has been given to this phenomenon [25]. Notice that since the direct dipole transition between the ground state hyperfine states is forbidden, the coherent superposition in Eq. (2.16) lasts for a long time, resulting in a very narrow resonance.

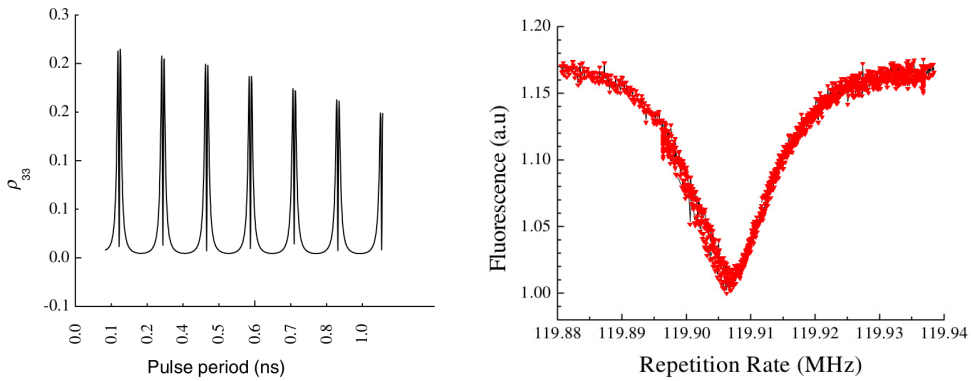

Figure 2.2: Right: The excited state population ρ_{33} as a function of pulse period. Population vanishes from the excited state, or trapped in the ground state when the inverse of pulse period is an integer sub-harmonic of the hyperfine splitting. Here, the dark-resonances corresponding to first 7 sub-harmonics are shown. Left: an experimental observation of the dark-line when the repetition rate is tuned to 1/57th harmonic of hyperfine splitting.

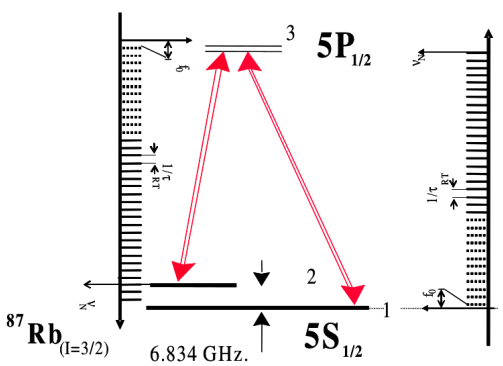

Figure 2.3: A schematic of interaction of a frequency comb with ground state ^{87}Rb atoms. Not drawn to scale.

For excitation with a mode-locked pulse train, it is the modes of the frequency comb that interact with the atomic lines, as shown in Figure 2.3. The right panel in

Figure 2.2 shows an experimental observation of the dark-line resonance in a ^{87}Rb vapor. The repetition rate is scanned across 1/57th of the 6.8 GHz hyperfine splitting. In this experiment, the vapor cell is not filled with buffer gas nor coated with anti-relaxation coating. At room temperature (22 °C), the mean thermal velocity is 138 m/s, which implies that the transit-time of ^{87}Rb atoms through a 2 mm laser beam is $\tau_{\text{transit}} = 14.5\ \mu$s, and therefore the linewidth is dominated by the transit-broadening $\Delta\nu_{\text{transit}} = 11$ kHz.

Detuning of optical frequency

From a numerical simulation, it is found that the dark-line resonance does not crucially depends on the one-photon detuning, Δ_{31} and Δ_{21}. Figure 2.4 shows several simulation results for different values of the one-photon detuning. The detuning affects the depth of the dark-line resonance, but not the width nor the resonance frequency.

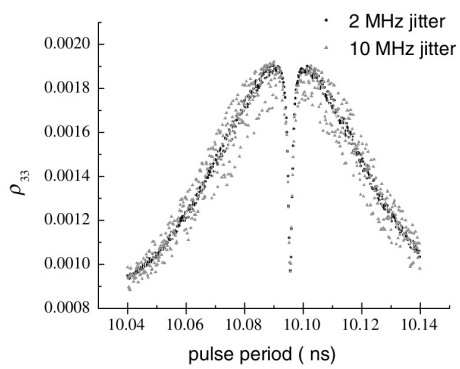

Figure 2.4: One-photon detuning Δ_{ij} does not affect the resonance characteristics such as line width or resonance frequency, although it affects the depth of the resonance.

Dependence on the area

An important parameter to characterize a pulse-matter interaction is the "area", which is defined as

$$\theta \equiv \int_{-\infty}^{\infty} \kappa \mathcal{E} dt \tag{2.17}$$

where the rotating-wave-approximation and zero detuning are assumed. The area is a time integral of the Rabi frequency, thus dimensionless, and is a measure of the strength of the interaction. Figure 2.5 shows the dependence of the dark resonance on the area. For areas below 0.01 the dark resonance is only a small perturbation to a weak fluorescence. For the area between 0.01 and 0.1 the narrow dark-line of the dark resonance appears. As the area increases above 0.5 the dark resonance starts broadening, leading to complete extinction of the dark resonance feature for an area equal to 2 and larger.

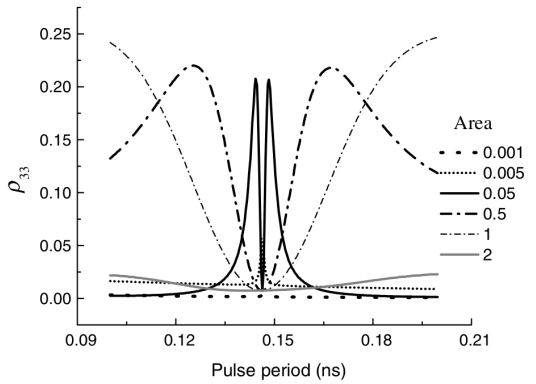

Figure 2.5: The dependence of the dark resonance on the area reveals that the resonance feature can be clearly observed for the areas between $0.01 \sim 0.5$. Below that range, it is only a small perturbation to a weak fluorescence. Above the range, a power broadening washes out the resonance feature.

2.4 Dark-line resonance in a magnetic field

2.4.1 Zeeman splitting of magnetic sublevels

The total atomic magnetic moment of the atom is the sum of the electronic μ_e and nuclear moments μ_I [43]:

$$\mu_{atom} = \mu_e + \mu_I = -\mu_B(g_s S + g_L L + g_I I) \tag{2.18}$$

where μ_B is the Bohr magneton, g_s, g_L and g_I are the Landé g-factors for the electron spin, electron orbital and nucleus. Under an external magnetic field, the atomic magnetic moments precess with energy given by the Hamiltonian [5]

$$\begin{aligned} H_B &= -\mu_{atom} \cdot B \qquad (2.19)\\ &= \mu_B \left(g_s S + g_L L + g_I I\right) \cdot B \\ &= \mu_B \left(g_s S_z + g_L L_z + g_I I_z\right) B_z \qquad (2.20) \end{aligned}$$

where in the last step the direction of the magnetic field is taken in z-direction; $B = B_z$. The energy of the precessing magnetic moment thus depends on the projection of the magnetic moment onto the direction of the applied magnetic field.

If the energy shift due to the magnetic field is small compared to the fine-structure splitting, then J is a good quantum number and the interaction Hamiltonian becomes

$$H_B = \mu_B \left(g_J J_z + g_I I_z\right) B_z \tag{2.21}$$

If the energy shift due to the magnetic field is even small compared to the hyperfine splitting, then F is also a good quantum number, so the interaction Hamiltonian is further simplified to

$$H_B = \mu_B g_F F_z B_z = \mu_B g_F m_F B_z \tag{2.22}$$

where the hyperfine Landé g-factor is

$$g_F \simeq g_J \frac{F(F+1) - I(I+1) + J(J+1)}{2F(F+1)} = \mp 0.5 \tag{2.23}$$

for ground state ^{87}Rb which has nuclear spin of $I = 3/2$ and electron angular momentum $J = L + S = 1/2$. The "-" and "+" signs correspond to $F = 1$ and $F = 2$ states.

m_F in Eq. (2.22) denotes the magnetic quantum number which is the projection of F onto the direction of the magnetic field. Due to the quantum nature of the wave function and to a simple fact that a projection of a vector cannot exceed the length of the vector itself, m_F has an upper and a lower bound and are separated by an integer:

$$-F \geq m_F \geq F \tag{2.24}$$

Therefore, there are $2F = 1$ number of magnetic sublevels in each hyperfine state with F. The energy shift of magnetic sublevels labelled as $|F\ m_F\rangle$ is

$$\Delta E_{|F\ m_F\rangle} = \mu_B g_F m_F B_z \tag{2.25}$$

$5S_{1/2}$ state of ^{87}Rb has $F = 1$ and $F = 2$ hyperfine states, each of which has 3 and 5 magnetic sublevels, respectively. Under a weak magnetic field, they shift in energy according to Eq. (2.25). With $g_F = -0.5$ for $F = 1$ and $g_F = +0.5$ for $F = 2$ hyperfine state, the corresponding frequency difference between adjacent magnetic sublevels is given by ∓ 0.7 kHz/mG where "-" and "+" signs correspond to $F = 1$ and $F = 2$ states, respectively. For $5P_{1/2}$ state, the frequency difference is ∓ 0.23 kHz/mG, where "-" for $F = 1$ and "+" for $F = 2$ hyperfine state.

2.4.2 Selection rule for the Λ-system

The spectral location of the dark-line resonance is determined by the energy shift of the sublevels forming the coherent dark-state. A specific pair allowed to form

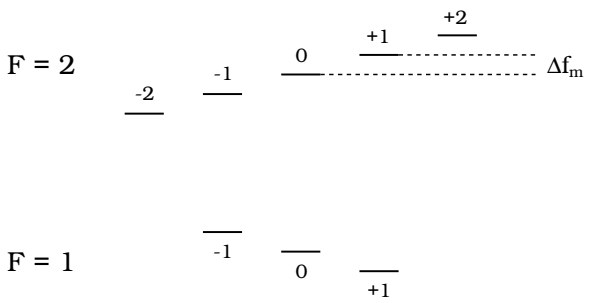

Figure 2.6: Zeeman splitting of the ground state $5S_{1/2}$ of ^{87}Rb . The magnetic sublevels in upper ($F = 2$) and lower ($F = 1$) hyperfine states shifts in opposite direction in a magnetic field. The frequency difference between adjacent magnetic sublevels is $\Delta f_m = \mp 0.7$ kHz/mG in the ground state.

the dark-state is dictated by the selection rule for two-photon transition in the Λ-system, imposed by the conservation of angular momentum [47]. The two-photon transition in the Λ-system takes place with simultaneous excitation and scattering of photons [48]. The conservation of angular momentum restricts the change in the angular momentum of the atoms to be equal to the total photon angular momenta involved in the two photon interaction, namely

$$\Delta m_F = m_e - m_s \tag{2.26}$$

where m_e and m_s are the angular momenta of exciting and scattered photons, respectively.

When the magnetic field is directed along the beam propagation, a circularly polarized light has a projection of the angular momentum of $m = \pm 1$ along the magnetic field with the sign determined by the "handness" of the polarization. The photons in such light field are dubbed σ_+ and σ_- photons. A linearly polarized light can be expressed as a linear combination of σ_+ and σ_- photons.

In an experiment where a magnetic field is applied along the beam direction, the selection rule for two-photon transition is therefore satisfied when $\Delta m_F = -2, 0, 2$. The pairs of the sublevels $|F, m_F\rangle$ for ^{87}Rb that satisfy the selection rule are the

following:

$$\Delta m_F = 0: \quad |1,-1\rangle \leftrightarrow |2,-1\rangle$$
$$|1,0\rangle \leftrightarrow |2,0\rangle$$
$$|1,1\rangle \leftrightarrow |2,1\rangle$$

$$\Delta m_F = \pm 2: \quad |1,-1\rangle \leftrightarrow |2,1\rangle$$
$$|1,0\rangle \leftrightarrow |2,2\rangle$$
$$|1,0\rangle \leftrightarrow |2,-2\rangle$$
$$|1,1\rangle \leftrightarrow |2,-1\rangle$$

which are depicted in Figure 2.7.

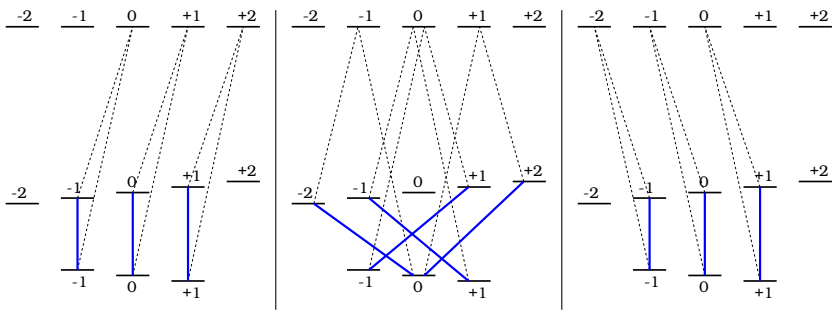

Figure 2.7: The selection rule determines which pair of sublevels to form a coherent dark-state. In the presence of a magnetic field along the beam propagation direction, σ_+ photons form the dark-state between the sublevels with the same m_F such that $\Delta m_F = 0$ (left). The same rule applies for σ_- photons (right). When both $\sigma_\pm$ photons are present, as in a linearly polarized light, the two-photon transition is accomplished when $\Delta m_F = \pm 2$ (center).

2.4.3 Measurement of Zeeman splitting of the dark-line resonance

A circularly polarized light is generated by sending a linearly polarized light through a quarter-wave-plate (QWP). By defining the angle θ between the fast axis of QWP and the polarization axis of the input beam, as shown in Figure 2.8, the output beam from QWP can be expressed as

$$\begin{aligned} E(\theta) &= E_0 \left(\cos\theta\hat{x} + i\sin\theta\hat{y}\right) \\ &= E_0 \left[\cos\theta(\hat{L}+\hat{R}) + \sin\theta(\hat{L}-\hat{R})\right] \\ &= E_0 \left[(\cos\theta+\sin\theta)\hat{L} + (\cos\theta-\sin\theta)\hat{R}\right] \end{aligned} \tag{2.27}$$

where $\hat{x}$ and $\hat{y}$ are decomposed in terms of circular unit vectors $\hat{L}$ and $\hat{R}$ as

$$\hat{R} = \frac{\hat{x}+i\hat{y}}{2} \quad \hat{L} = \frac{\hat{x}-i\hat{y}}{2}$$
$$\hat{x} = \hat{L}+\hat{R} \quad \hat{y} = -i(\hat{L}-\hat{R})$$

A left circular polarization (LCP), denoted as $\hat{L}$, carries the photon spin angular momentum of -1 in unit of $\hbar$ (i.e. σ_- photons). A right circular polarization (RCP), denoted by $\hat{R}$, carriers $+1$ spin angular momentum (i.e. σ_+ photons).

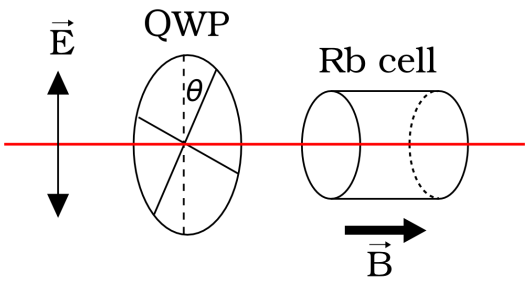

Figure 2.8: A geometry of the experiment. An external magnetic field is applied along the beam direction. θ is the relative angle between the plane of linear polarization of the input beam and the fast axis of QWP.

Figure 2.9 shows an experimental measurement of the Zeeman splitting of the dark-line resonance when a 350 mG magnetic field is applied along the direction of the beam propagation. The ^{87}Rb cell is heated to approximately 45 °C. With $B_y = 350$ mG, each sublevel shifts by $|\Delta f_m| = m_F \times 245$ kHz. In terms of the repetition rate, which is 1/45th of the hyperfine splitting in this particular experiment[1], each sublevel appears to be shifted by $m_F \times 5.5$ kHz. The selection rule for the two-photon transition in this case allows only those pairs shown in Figure 2.7 to form the dark-state. There is one non-shifted dark-state and two shifted dark-states by ±11 kHz.

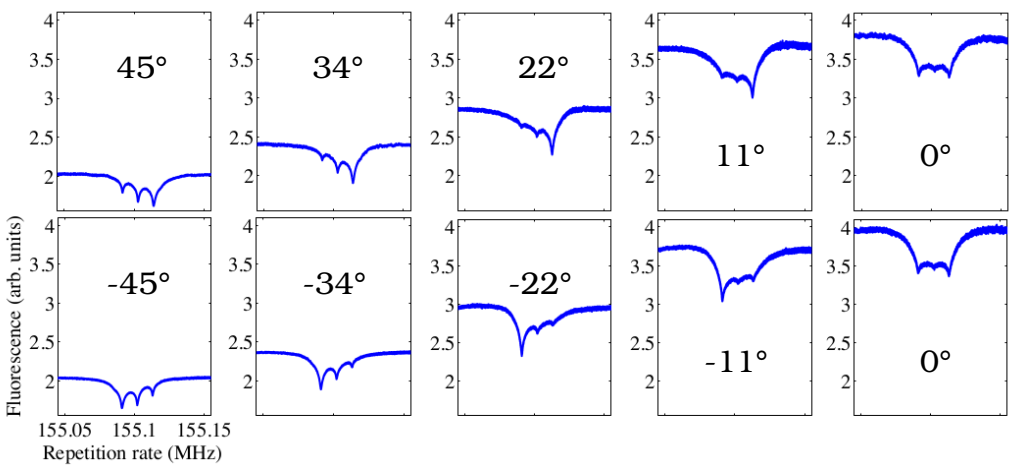

Figure 2.9: Zeeman splitting and optical pumping of the dark-line resonace. A magnetic field is applied along the beam direction. The angles indicate the angle between the fast-axis of QWP and the input light polarization.

[1]The resonance repetition in this experiment is noticeably shifted from exactly 1/45th of the hyperfine splitting. This effect is due to a modification to the laser spectrum which will be discussed in more details in Chapter 3 and 6.

2.5 Optical pumping of the dark-resonance

2.5.1 Optical pumping

A photon carries unit spin angular momentum along the propagation direction. When an atom absorbs a photon, the spin angular momentum is transferred into the atomic system. Suppose circularly polarized light is passed through an ensemble of atoms whose quantization axis is defined along the beam propagation. Over a number of absorptions of σ_+ (or σ_-) photons and emissions of randomly polarized photons, the entire atomic population is slowly transferred into the magnetic sublevel with maximum (minimum) quantum number. As a result, a net spin polarization of the ensemble is established. This process of optical pumping [49] is an effective way to create a macroscopic polarization, which has been exploited for high-sensitivity magnetometers [20].

2.5.2 Optical pumping of the dark-line resonance

A long-lived macroscopic polarization can be achieved by preparing a spin polarized CPT. The effect of optical pumping in CPT can be observed as an increase of the dark-line resonance signal formed between $m_F = 1$ or $m_F = -1$ sublevels. The top panels in Figure 2.9 show the dark-line resonance signals while the light polarization is varied from RCP (left-most panel) to linear polarization (right-most panel). When the light is RCP, more atoms are pumped into m=1 sublevels, and a larger dark-line resonance is obtained from the $|1,1\rangle \leftrightarrow |2,1\rangle$ superposition state. The effect of optical pumping is also seen as a reduction of the overall fluorescence. This is because a fair amount of atoms are trapped in the maximum angular momentum state $m_F = +2$ where there is no excited state to be promoted by absorbing σ_+ photons. As QWP is rotated away from 45°, the beam becomes a mixture of RCP and LCP. At $\theta = 0°$ the

equal amount of RCP and LCP makes the dark-line resonances nearly symmetric. In this case, there is no macroscopic spin polarization. By further rotating QWP into negative θ, as shown in the bottom panels, the amount of LCP increases and the population is pushed into the sublevels with negative magnetic quantum numbers. At $\theta = -45°$, the largest dark-resonance signal is obtained from $|1,-1\rangle \leftrightarrow |2,-1\rangle$ superposition. It is interesting to notice that optical pumping seems to be most efficient when QWP is rotated at $\theta = \pm 22°$.

2.6 Conclusion

In this chapter, a method of CPT spectroscopy of ^{87}Rb using a frequency comb is reviewed. The CPT resonance occurs when the repetition is tuned to a sub-harmonic of the hyperfine splitting of the ground state. A narrow dark-line with width on the order of 10 kHz with respect to the repetition rate is measured in a vapor withtout a buffer gas or in a cell with no anti-relaxation coating. Numerically solving the density matrix equations for a simplified three-level Λ-system, the dark-line features including the resonance frequency and the width are not affected by optical frequency detuning. However, it is greatly dependent of the area. For areas larger than 2, the dark-line severally disturbed by power broadening.

The dependence of the dark-line resonance on a magnetic field and the relative orientation of the light polarization is studied. Due to the Zeeman splitting of the magnetic sublevels, the observed dark-line resonance splits into multiple dips whose frequency depend on the energy shift of the individual sublevels forming the coherent dark-state. Under an external magnetic field applied along the beam propagation direction, the selection rule for two-photon transition imposes a condition $\Delta m_F = 0, \pm 2$. In excitation with σ_+ or σ_- photons, the optical pumping into the sublevels with larger magnetic number is observed. The strongest dark-line is obtained from

a coherent dark-state formed between $m_F = 1$ sublevels when excitating with σ_+ photons, and for excitation with σ_- photons the strongest signal is obtained for the superposition between $m_F = -1$ sublevels. The optical pumping in CPT establishes a long-lived atomic polarization, which opens a possibility for application in the IPI atomic magnetometery.

Chapter 3

Enhancement of CPT signal via spectral shaping

3.1 A lack of spectral overlap between comb and atoms

In Chapter 2, a method to create coherent population trapping (CPT) of ground state ^{87}Rb atoms using a frequency comb is presented. Pumping with circularly polarized light, the atomic population is pumped into a superposition of sublevels with large angular momentum. An ensemble of such atoms establishes a long-lived spin polarization. By increasing the pumping power, a further enhancement of the atomic spin polarization is expected.

Pumping with a frequency comb, however, poses an issue of small spectral overlap between the frequency comb and atomic lines. A frequency comb generated form a typical titanium-sapphire mode-locked laser spans between $10^2 \sim 10^5$ GHz. On the other hand, an inhomogeneously broadened atomic linewidth is in a range of

$10^{-1} \sim 10^{0}$ GHz. The spectral components that overlap with the atomic lines are thus only a fraction of the total spectral power contained in the entire frequency comb.

3.2 Spectral shaping

The problem of a lack of spectral overlap can be circumvented by shaping the frequency comb to match the shape of the atomic lines. An increased spectral overlap is expected to improve the pumping efficiency of the atomic population into the magnetic field sensitive dark state. Here, a simple yet effective spectral shaping method using an intracavity Fabry-Perot etalon (FPE) will be presented.

3.2.1 Spectral shaping using an intracavity Fabry-Perot

FPE transmission function

FPEs are commonly used inside a continuous-wave (CW) laser to force a laser to oscillate in a selected single mode. The principle of this technique is a combination of multiple beam interferences in FPE [50] with the existence of a saturable gain in the laser cavity [9]. The effect of the multiple beam interferences provide a frequency filter in the laser cavity, and the saturable gain selectively amplifies the spectral components that experience maximum transmission through FPE.

The multiple beam interferences give rise to a transmission spectrum determined by

$$\tilde{\mathcal{T}}(\Omega) = \frac{(1-R)e^{-i\delta/2}}{1-Re^{-i\delta}} \tag{3.1}$$

where R is the reflectivity of the interface and δ is a round-trip phase shift of an

optical field in FPE. The intensity transmission function is then

$$T = |\tilde{\mathcal{T}}|^2 = \frac{(1-R)^2}{1+R^2-2R\cos\delta} \tag{3.2}$$

which is a series of transmission peaks in the frequency domain. The maximum transmission ($T = 1$) occurs when an optical field experiences a round trip phase equal to an integer multiple of 2π for constructive interference:

$$\delta = -\frac{4\pi f_\ell n_p d\cos\theta_{in}}{c} = 2\pi N \tag{3.3}$$

where f_ℓ is the optical frequency, n_p is the phase index of refraction, d is the thickness of FPE, θ_{in} is the internal angle of the beam with respect to the surface plane of FPE and N is an integer. The spectral distance between the transmission peaks is then given by

$$f_{fsr} = \frac{c}{2n_p d} \tag{3.4}$$

This is the *free-spectral-range* (fsr) of FPE. It is also the inverse of the time a phase front takes to make a round-trip in FPE. When the reflectivity is not too high, Eq. (3.2) fits well to a sinusoidal function. With higher reflectivity, each transmission peak can be approximated by a Lorentzian with its width given by [51]

$$\Delta_{1/2} = \frac{1-R}{\sqrt{R}} \tag{3.5}$$

The higher the reflectivity, the narrower the transmission peaks become, as shown in Figure 3.1.

Effect of a saturable gain

In an inverted homogeneous gain medium, the stimulated emission rate is proportional to the photon numbers (intensity) [9]. Thus, the spectral components that experience maximum transmission through FPE, that is the resonance frequencies,

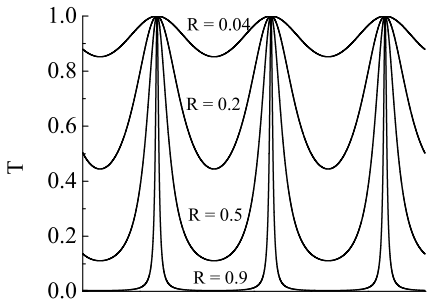

Figure 3.1: Intensity transmission through FPE for various values of R.

have a larger chance to create photons of the same kind. Since the gain can only store a finite amount of energy, it saturates and leaves less chance to be amplified for other spectral components that are off-resonance to FPE. This positive feedback process continues until the laser reaches the steady-state and sets the oscillating modes of the laser. By solving Eq. (3.3) for the laser frequency f_ℓ,

$$f_\ell = \frac{cN}{n_p d \cos\theta_{in}} \tag{3.6}$$

Or, in terms of wavelength:

$$\lambda_\ell = \frac{n_p d \cos\theta_{in}}{N} \tag{3.7}$$

As mentioned earlier, an intracavity FPE thus serves as a frequency tuner.

Shaping of a pulse spectrum

When the pulse spectrum is wider than f_{fsr}, there are multiple transmission peaks overlapping with the pulse spectrum, which gives rise to a periodic spectral amplitude modulation in the transmission spectrum. If a pulse spectrum is sufficiently wide, the spectral width is not significantly modified by FPE transmission function. In the time domain, the transmitted intensity profile comprises a train of pulses with

unchanged width and decaying intensity. The period of the pulse train is determined by f_{fsr}, and the rate of intensity decay is determined by $\Delta_{1/2}$. In order to maximize the spectral overlap between the pulse spectrum and the atomic lines, f_{fsr} needs to match the spectral spacing of the atomic transitions desired to be excited. The concept of the spectral shaping of a pulse train using an intracavity FPE is depicted in Figure 3.2.

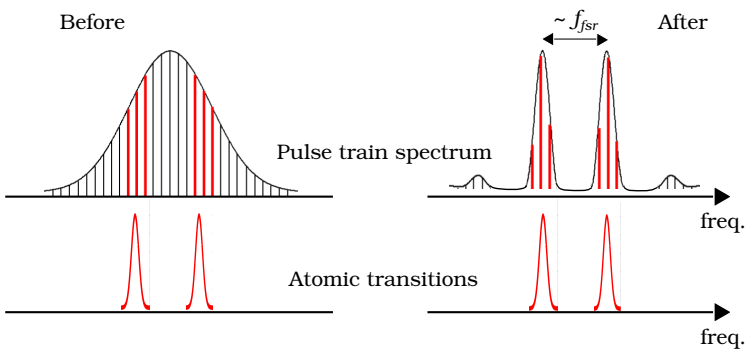

Figure 3.2: The concept of spectral shaping of a pulse train using an intracavity FPE. The FPE tranmission function results in a spectral amplitude modulation which increases the spectral overlap with the atomic transitions.

3.3 Experimental setup

3.3.1 Home-built titanium-sapphire laser

Experiments are performed using a home-build linear Titanium-Sapphire mode-locked laser shown in Figure 3.3. Mode-locking is assisted by a multiple quantum well saturable absorber (MQW-SAM) mounted on a Bragg reflecting mirror which serves as the cavity end mirror. The output coupler is mounted on a translation stage which allows for scanning the cavity length. A pair of prisms and a birefringent filter are used for tuning the laser frequency near 795 nm. They also limit the

spectral bandwidth to attain picosecond pulses. A reflected beam from one of the prisms is sampled by a 25 GHz high-speed InGaAs photodetector (New Focus 1437) to characterize the pulse train. The temporal profile is monitored on an 8 GHz digital oscilloscope (Tektronix DPO 70804). The spectrum is monitored on a 25 GHz digital radio frequency (RF) spectrum analyzer (Agilent MXA N9020).

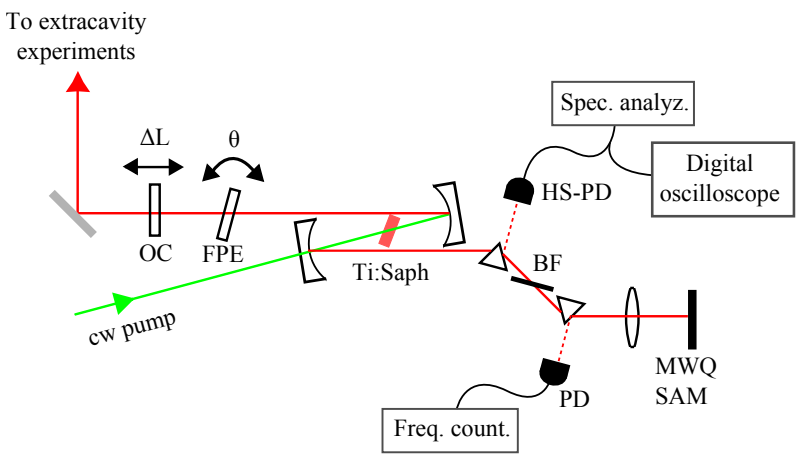

Figure 3.3: Home-build Ti:Sapphire mode-locked laser with an intracavity Fabry-Perot etalon (FPE). OC: output coupler, BF: birefringent filter, HS-PD: high-speed photodetector, PD: photodetector, MQW-SAM: multiple quantum well saturable absorber mirror.

3.3.2 Intracavity FPE

The FPE is a 15.12 mm fused-silica slab with parallel and uncoated surfaces. The free spectral range of this FPE is

$$\Delta f = \frac{c}{2nd} \simeq 6.82 \text{ GHz} \tag{3.8}$$

where $c = 2.998 \times 10^{11}$ mm/s and $n_p = 1.4534$ at 795 nm. The FPE is mounted on a standard mirror mount (Newport Ultima 100A) with one of the adjustment screws replaced with a motorized micrometer and inserted near the output coupler. The exact location of the FPE with respect to the output coupler does not affect

the characteristics of the laser. Tilt angles of FPE with respect to the beam axis is controlled and monitored remotely by a data acquisition system.

3.3.3 CPT spectroscopy apparatus

The main output of the laser is sent to a spectroscopy apparatus including a vapor cell, a Helmholtz coil and data acquisition instruments as shown in Figure 3.4. The vapor cell is an evacuated Pyrex cylinder filled with enriched rubidium-87 isotope, wrapped with bifilar heating wires. It is heated to approximately 45 °C and placed in the center of a three-axis Helmholtz coil. The cell assembly has a 3 mm × 4 mm rectangular access window that allows monitoring of a fluorescence signal, which is collected by a photomultiplier tube (PMT) (Hamamatsu R928) with an interference filter for 795 nm. The signal from the PMT is sent to a lock-in amplifier and mixed with a reference chopper frequency. The lock-in signal is then sent to a data acquisition system.

For transmission measuremetns, the incident and transmitted beams are compared. Two different avalanche photodiodes (APDs) are employed to monitor each of the beam components. Each APD signal is demodulated at the repetition rate of the laser using RF lock-amplifier. The difference between the signals generated from the two lock-in amplifiers is calculated and recorded using LabVIEW.

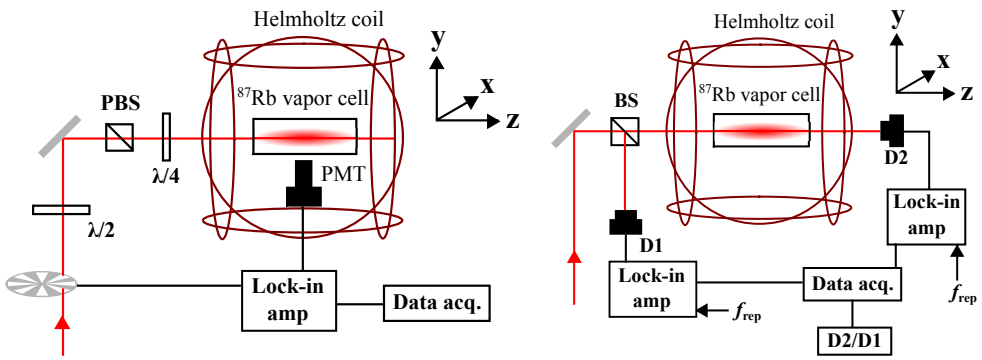

Figure 3.4: CPT spectroscopy apparatus for fluorescence measurement (left) and for transmission measurement (right).

3.4 Spectrally shaped pulse train

3.4.1 Generation of a modified pulse train

A typical output of the mode-locked laser with 15 mm fused silica FPE is shown in Figure 3.5. In the absence of the intracavity FPE, the laser operates as a standard mode-locked laser. It generates a continuous mode-locked pulse train with a pulse period of approximately 6.4 ns. On the other hand, in the presence of the intracavity FPE, a Bell-shape "bunch" of pulses is formed and repeated in every round trip of the laser cavity. The temporal extension of the bunch is approximately 1.3 ns (FWHM) and there are at least 13 pulses in each bunch. The appearance of the bunches seen on the oscilloscope trace in Figure 3.5 resembles an interferometric auto-correlation of a train of femtosecond pulses. However, what may appear as an optical oscillation is partially resolved intensity envelopes of the individual pulses. From an actual auto-correlation of the bunch, the pulse width and inter-pulse period are respectively found to be 2 ps and 148 ps, agreeing with the group round trip time of the 15.12 mm fused-silica, $\tau_{FP} = 2n_g d/c$ with $n_g \approx 1.46$, where n_g is the group index of refraction.

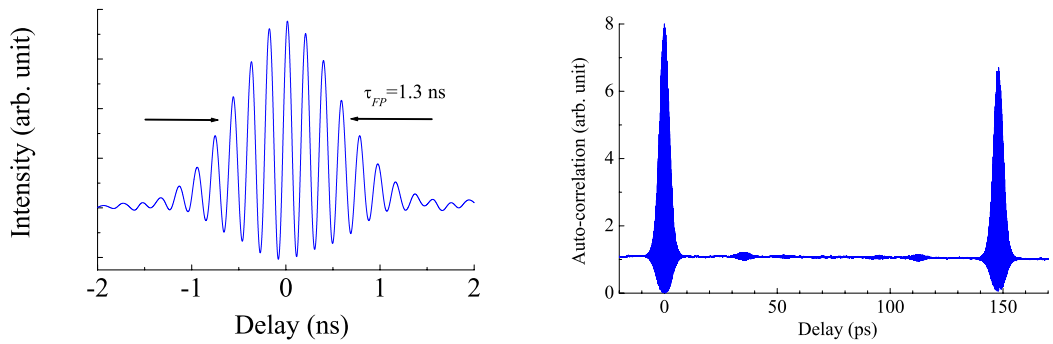

Figure 3.5: Temporal profile of an output of the mode-locked laser with a 15 mm intra-cavity FPE. Left: An oscilloscope trace acquired with a 25 GHz photodetector and an 8 GHz oscilloscope shows a generation of multiple pulses forming 1.3 ns wide bunch. Right: An interferometric auto-correlation trace reveals the individual 2 ps pulses in the bunch, with pulse period of 148 ps.

3.4.2 Modified RF spectrum

The RF spectrum of the spectrally shaped pulse train shows a set of modes in the neighborhood of 6.8 GHz, as shown in the left panel in Figure 3.6. The central 6.8 GHz mode corresponds to the inverse of 148 ps inter-pulse period. The modes around the 6.8 GHz mode are spaced evenly by the inverse of the cavity round trip time of the center of gravity of the bunch. It is found that the process of multiple reflections in FPE causes a back-ward flow of energy among the pulses within a bunch, which reduces the average velocity of the bunch during a cavity round trip.[1] Since the pulse bunch envelope travels at much slower velocity than individual pulses, the cavity repetition rate is significantly reduced from that of a standard single pulse mode-locked laser. Consequently, the difference between the bunch and the group (pulse) velocity results in a phase slippage between the bunch envelope and pulses in every round trip, giving rise to an offset frequency in the RF spectrum. The right panel in Figure 3.6 shows a comparison with the RF spectrum of a standard single

[1]More details on the slow bunch velocity are presented in Chapter 6.

pulse mode-locked pulse train. Their repetition rates are adjusted to be equal in order to indicate the presence of the offset frequency. The RF modes of the pulse bunch train is shifted by approximately 10 MHz. This offset frequency is analogous to the carrier-envelope offset (CEO) f_0 in optical frequency arising from the difference between the carrier and group velocity (see Section 1.2.1 for the definition of f_0). The spectral location of the RF modes shown in the figure is empirically found to be

$$f_N = f_{PBO} + N f_{rep} \tag{3.9}$$

where N is an integer and f_{PBO} is the offset frequency. The subscript PBO stands for "pulse-to-bunch offset".

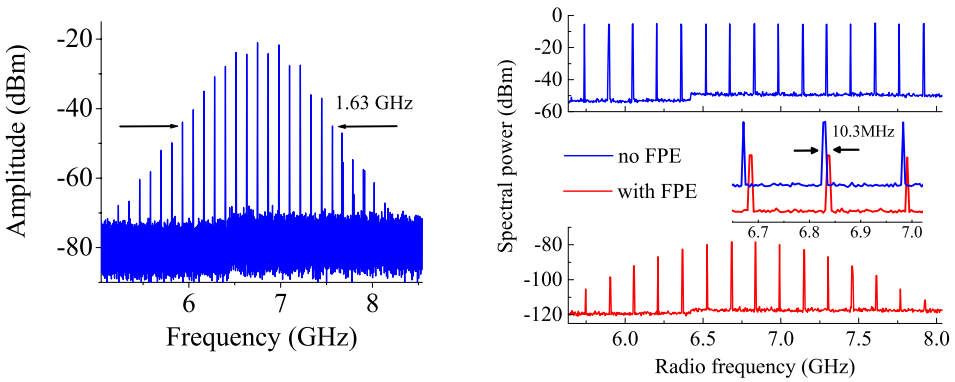

Figure 3.6: Left: The RF spectrum of the spectrally shaped pulse train due to the intracavity FPE. Right: A comparison of RF spectra of a pulse train of a standard mode-locked laser (top) and of the spectral shaped pulse train (bottom). Repetition rate of both lasers are set equal. Inset: A zoom of the 6.8 GHz region to indicate a shift of the spectrum, which is a consequence of the propagation velocity of the bunch envelop being slower than the constituent pulses.

3.4.3 Wavelength tuning

The interferences amongst multiple pulses in FPE give rise to wavelength tunability of the laser, as described by Eq. (3.7). Figure 3.7 shows a measured fluorescence

from the D1 line of ^{87}Rb vapor as a function of the internal angle of the intracavity FPE, overlaid with a calculated laser wavelength using Eq. (3.7). The peaks of the fluorescence are observed when the laser spectrum coincides with the D1 lines in the neighboorhood of $\lambda_\ell = 795$ nm. Since FPE is designed to match its free-spectral-range to the 6.8 GHz ground state hyperfine splitting of ^{87}Rb, a single peak of the fluorescence appears every time the round trip phase in the FPE, δ, changes by 2π. The behaviour of the fluorescence excellently agrees with the dependence of the wavelength on the FPE angle.

In addition, each fluorescence peak appears to be composed of two sub-peaks, as can be seen as a shoulder-like structure on each peak. By calibrating with the spacing between the fluorescence peaks, which is 6.83 GHz, the frequency difference of the sub-peaks is found to be approximately 815 MHz. This value is close to the excited state hyperfine splitting of 814.52 MHz. The relative transition strength between the ground state and excited state hyperfine levels are shown in Table 6.1 [5]. It is clear that the lower frequency transition ($|g\rangle \rightarrow |e, F' = 1\rangle$) is half as strong as the higher frequency transition ($|g\rangle \rightarrow |e, F' = 2\rangle$), provided that the equal amount of optical power is applied to those transitions. In the observed fluorescence signal, the smaller sub-peaks in the shoulder-like structure appear at smaller angles. Since the frequency increases with the FPE angle, the sub-peaks are indeed from the transitions to the excited hyperfine manifolds.

D_1 ($5^2S_{1/2} \rightarrow 5^2P_{1/2}$)	S_{22}	1/2	S_{12}	5/6
	S_{21}	1/2	S_{11}	1/6

Table 3.1: Relative strength $S_{FF'}$ of the hyperfine transitions for ^{87}Rb D_1 line [5]. F and F' represent the ground state and excited state hyperfine manifold, respectively.

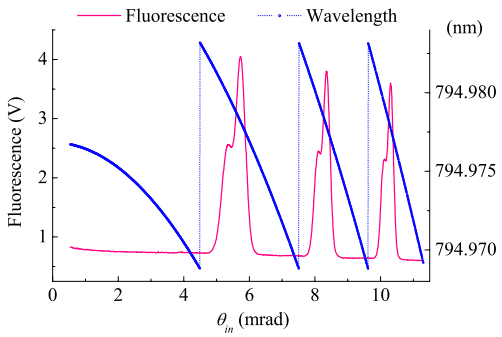

Figure 3.7: A fluorescence signal from D1 line of ^{87}Rb as a function of the FPE angle. A blue dot-dashed line is the wavelength calculated using Eq. (3.7).

3.5 CPT spectroscopy using the spectral shaped pulse train

3.5.1 Shift of the repetition rate resonance

When applying the spectrally shaped pulse train, the CPT resonance, measured with respect to the repetition rate, appears to be shifted from that observed when using a standard mode-locked pulse train. Figure 3.8 shows the D1 fluorescence of ^{87}Rb as a function of the repetition rate for both cases of a standard and the spectral shaped pulse train. Without an intracavity FPE, in case of a standard mode-locked pulse train, the CPT resonance occurs at a repetition rate which is a sub-harmonic of the hyperfine splitting, given by $f_{rep}^{CPT} = f_{HFS}/N$. In the particular measurement presented in the figure, the resonance repetition rate corresponds to 1/44th of the hyperfine splitting, for which $f_{rep}^{CPT} = 155.333$ MHz.

With the spectral shaped pulse train, the CPT resonance appears to be reduced by approximately 200 kHz. Three CPT resonance profiles measured in the presence of an intracavity FPE are shown on the left in the figure, measured at angles where

the fluorescence is maximum, corresponding to the fluorescence peaks similar to those in Figure 3.7. The resonance repetition rates are 155.097, 155.111 and 155.123 MHz, respectively.

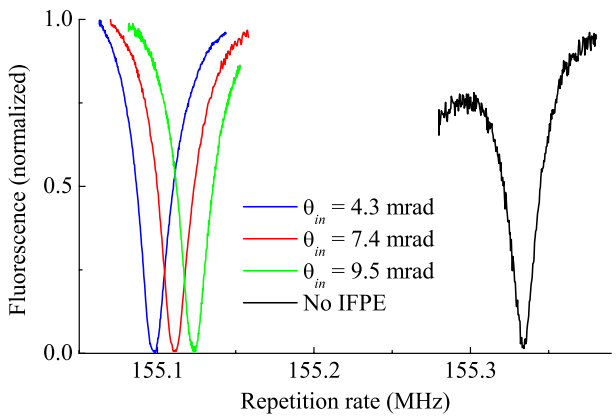

Figure 3.8: A comparison of CPT resonance induced with a standard pulse train (black) and with the spectral shaped pulse train with the intracavity FPE set at three different angles (color).

The reason for the observed shift of resonance is explained by the modification to the spectral location of the RF modes described by Eq. (3.9). For the CPT resonance to be induced, it is required that the separation between the optical modes to match the hyperfine splitting. That is to say, it is only required to have one of the RF modes to be equal to the hyperfine splitting:

$$f_N = f_{PBO} + N f_{rep} = f_{HFS} \tag{3.10}$$

Solving for f_{rep}, we have

$$f_{rep}^{CPT} = \frac{f_{HFS} - f_{PBO}}{N}. \tag{3.11}$$

Compare to the case for a single pulse mode-locked laser, the resonance repetition rate is reduced by a factor of f_{PBO}/N. As will be discussed later in Chapter 6, f_{PBO}

varies with the FPE angle. Figure 3.9 shows f_{PBO} as a function of the FPE angle. The values of f_{PBO} at angles where the fluorescence peaks occur are indicated in the figure. These angles also correspond to where the three fluorescence signals shown in Figure 3.8 are measured. With those values of f_{PBO}, $N = 44$ and $f_{HFS} = 6.83468261$ GHz, the resonance repetition rates using Eq. (3.11) are calculated. The results are summarized in Table 3.2. A good agreement between the measured and calculated CPT resonance repetition rate is obtained.

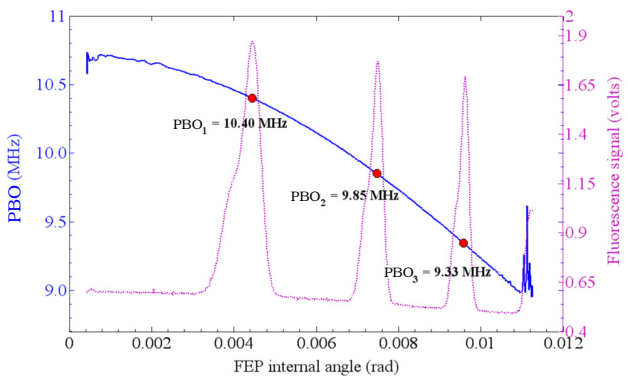

Figure 3.9: The angular dependence of the offset frequency, f_{PBO}. The values corresponding to the location of the fluorescence peaks are used to calculate the resonant repetition rate for CPT resonance using Eq. (3.11).

	Peak 1	Peak 2	Peak 3
f_{PBO}	10.04	9.85	9.33
f_{rep} (meas.)	155.097	155.111	155.123
f_{rep} (calc.)	155.0973	155.1098	155.1216

Table 3.2: CPT resonance is measured for each of the fluorescence peaks. The values of f_{PBO} at the angles corresponding to the fluorescence peaks are shown in the first row. The CPT resonance repetition rates measured for each fluorescence peak are shown in the second row. The calculated repetition rates to have $f_N = f_{HFS}$ for given f_{PBO} are shown in the third row.

3.5.2 Enhancement of the CPT signal

The motivation of inserting FPE in the mode-locked laser cavity is to increase the CPT signal by shaping the pulse spectrum to maximize the spectral overlap between the pulse spectrum and the D1 lines of ^{87}Rb. The enhancement of the CPT signal is found to be quite significant. In the left panel of Figure 3.10, the CPT signals obtained with and without the spectral shaping are compared. First, an overall fluorescence is increased nearly as much as a factor of 2, due to an increased spectral overlap. Second, the CPT signal contrast is increased from 15% up to 45%, measured in terms of a ratio of the depth of the CPT signal to the maximum fluorescence above the signal floor. Due to the increased optical power interacting with the hyperfine transitions, the CPT resonance is significantly broadened. By reducing the input power or expanding the beam cross-section, the linewidth comparable to the value obtained without a spectral shaping is obtained. The difference in the resonance repetition rate in the two cases is due to the presence of the offset frequency f_{PBO} as mentioned above.

The feature of the CPT resonance is also clearly observed in a transmission measurement, as shown in the right panel in Figure 3.10. The increased CPT signal contrast implies that more optical power contributes to pumping of the atomic population into the coherent dark-state through the two-photon process. An increased transmission at the CPT resonance clearly indicates that the input pulse train renders the ^{87}Rb atoms with reduced absorption or transparent. The narrow transparency window implies that there is a large dispersion, which can result in a reduction of group velocity, or a *slow-light* [30].

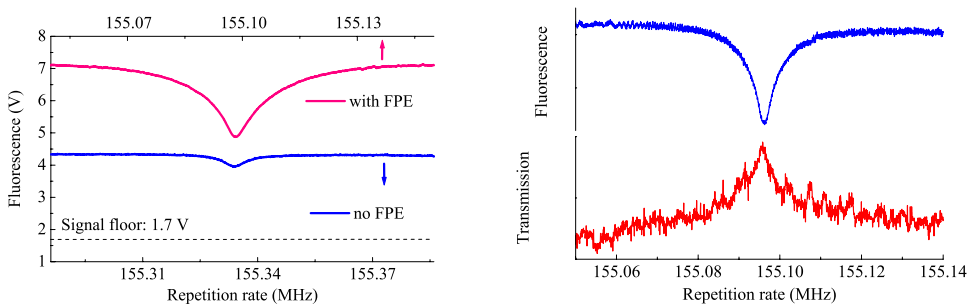

Figure 3.10: Enhancement of the CPT signal. Left: In a fluorescence measurement, the contrast of the resonance is increased from 15% to 45%. The resonance width is broadened due to the power-broadening, which can be suppressed by reducing the input power or expanding the beam area. Right: In a transmission measurement, a transparency peak is clearly measured. A ^{87}Rb vapor displaying the narrow transparency window should possess a large nonlinear dispersion to generate a slow-light.

3.5.3 Increased efficiency of optical pumping

Creating a long-lived ensemble polarization is an essential requirement for the development of ultra-sensitive magnetometers, as indicated in Eq. (1.14) which is characterized with the phase coherence time. In section 2.5 in the previous chapter, the optical pumping of CPT resonance is presented, as a method to create the long-lived ensemble polarization using a mode-locked pulse train. In order to pump more atomic population into larger magnetic moment states (i.e. $|m_F| \geq 1$), thus to create a larger ensemble magnetization, a further improvement of the optical pumping efficiency is desired. Since the efficiency of optical pumping generally improves with optical power at the atomic resonances [52], an enhancement of the optical pumping effect is expected with the spectrally shaped pulse train having an increased spectral overlap with the atomic resonance of ^{87}Rb atoms.

Figure 3.11 compares two cases of optically pumped CPT resonance obtained with a standard continuous pulse train (left) and the spectrally shaped pulse train (right). In both cases, a magnetic field of 350 mG is applied along the beam propagation

direction at the ^{87}Rb cell. The pulse trains are polarized in RCP (σ_+), thus the two-photon transition for the Λ-system does not allow the magnetic quantum number to change; the coherent dark-states are formed between the sublevels with the same magnetic number, $m_F = m'_F$. The energy of the dark-state formed between $m_F = -1$ sublevels is down-shifted (left dip in the figures), while that of $m_F = +1$ sublevels is up-shifted (right dip) from the unshifted energy of the magnetic field independent dark-state formed between $m_F = 0$ sublevels (middle dip).

The optical pumping of the atomic population into the the coherent dark-state formed between the field sensitive sublevels can be seen in both plots. Although there are still substantial population in m=-1 and m=0 sublevels, the CPT signal from the dark-state formed between $m_F = +1$ sublevels is the strongest. The overall fluorescence level in the excitation with the spectrally shaped pulse train is increased due to the increased spectral overlap for the one-photon dipole transition to $5P_{1/2}$. Comparing the relative strength of the middle dip and right dip, it is clear that the optical pumping is more efficient with the spectrally shaped pulse train.

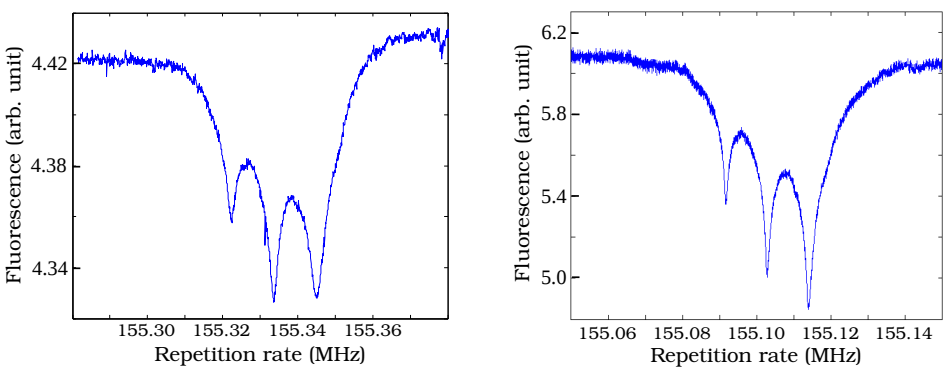

Figure 3.11: A comparison of optically pumped CPT resonances induced by a standard mode-locked pulse train (left) and the spectral shaped mode-locked pulse train (right). The optical pumping is enhanced with the spectral shaped pulse train.

3.6 Conclusion

A simple and effective method to enhance the interaction of a mode-locked pulse train and the ^{87}Rb atoms via intracavity spectral shaping using a glass FPE is presented. A spectral overlap between the pulse spectrum and the atomic lines is increased due to the spectral shaping. An increased overall fluorescence and the CPT signal contrast are achieved. The optical pumping of the atomic population into the magnetic field sensitive CPT resonance is improved.

By-products of the spectral shaping are also presented. Due to the modifications to the pulse spectrum, the shift of spectral location of the CPT resonances is observed. The wavelength tunability and a high-resolution spectroscopy of the excited state hyperfine states are presented.

Chapter 4

Push-pull optical pumping with a mode-locked laser

4.1 How does a train of alternating circular polarizations affect CPT?

As presented in the previous chapters, a train of circularly polarized pulses can produce a long-lived macroscopic magnetization through the process of optical pumping in CPT of the atomic population between the magnetic field sensitive sublevels. Such spin polarized coherent medium can be a host for the high-sensitivity magnetometers, such as in the case of the IPI magnetometer.

In a ring laser cavity constructed for an IPI magnetometer, there are two pulse trains with left and right circular polarizations circulating in the cavity. Each circularly polarized pulse train hits the atomic sample at the repetition rate of the cavity, with one polarization followed by another with a delay τ, as depicted in Figure 4.1. If there were only one circularly polarized pulse train, the atoms could be prepared

in the spin polarized dark-state by tuning the repetition rate into the CPT resonance. The presence of a RCP pulse which intercepts a train of LCP pulses disrupts the coherence being established by the LCP pulse train, and vice versa. How do different experimental parameters, including the delay between RCP and LCP (τ in the figure) pulses and the relative intensity between them, play a role in establishing CPT in the presence of two pulse trains with RCP and LCP? In the development of an IPI magnetometer based on CPT, these questions must be addressed.

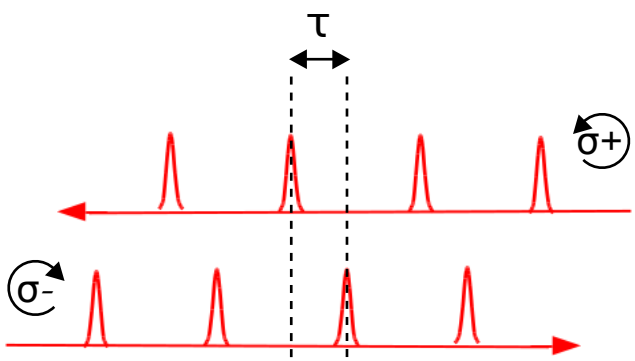

Figure 4.1: Two pulse trains, one polarized to be $\sigma+$ light and the other to be $\sigma-$ light, interacting with a ^{87}Rb vapor. A delay τ between the two pulse trains plays an important role in establishment of CPT.

4.2 CPT with a buffer gas

4.2.1 Improved efficiency of optical pumping

The degree of magnetization of the ensemble one can achieve depends on the overall efficiency of optical pumping. The cells used in the experiments presented in this chapter contain a buffer gas which is known to enhance the process of optical pumping through modifications to the relaxation rate of the excited state and ground state [49]. In the presence of a buffer gas, collisions with the buffer gas perturb the electron

wave function of the excited state of ^{87}Rb atoms, which result in faster decay rate of the excited state (pressure broadening). A thorough experimental investigation of the pressure broadening of the D1 line of ^{87}Rb in the presence of different kinds of buffer gases is performed by Romalis et. al. [53]. At typical buffer gas pressures in the experiments presented in this chapter ($\sim$ 20 Torr), the excited state relaxation rate Γ_3 (Figure 2.1) is of the order of 3×10^9 s^{-1} as compared to a free space decay rate (spontaneous emission) of the order of 3×10^7 s^{-1} [54]. This is particularly advantageous for excitation with a broadband radiation as in our case, since spectral overlap between the pulse spectrum and the atomic line is significantly increased. In the ground state, the spin relaxation is caused by diffusion of the atoms to the cell wall, collision with the buffer gas and spin-exchange collisions among ^{87}Rb atoms, which amount to the spin relaxation rate of the order of 1000 s^{-1} at $\sim$ 20 Torr. Therefore, when the laser intensity corresponding to excitation rates exceeds the ground state relaxation rate, strong optical pumping can be achieved. When a quenching gas, such as N_2, is used as a buffer gas, depolarization due to absorbing a randomly polarized photon can be suppressed, which further enhances the optical pumping.

4.2.2 Narrow CPT linewidth

In a vapor cell, ^{87}Rb atoms fly across the beam section at their mean thermal velocity. A finite interaction time contributes to the linewidth of the CPT resonance when all the other relaxation times are longer than the interaction time (transit-time broadening). In a typical experimental condition at room temperature (22 °C), the mean thermal velocity is 138 m/s, which implies that with a 2 mm beam diameter, the transit-time is $\tau_{\text{transit}} = 14.5$ μs, and the linewidth is $\Delta\nu_{\text{transit}} = 11$ kHz.

Addition of a buffer gas slows down the atomic motion through collisions with

this buffer gas and increases the duration of interaction between the atoms and the beam. Of course, a buffer gas also induces relaxation due to collision. Therefore, there is an optimum value for the buffer gas pressure. Under an approximation for small laser beam diameter ($d \ll D$, where d and D area the diameter of the laser beam and of the vapor cell), the ground state relaxation rate is given by [25];

$$\gamma_0 = 2.405^2 \frac{D}{a^2} \frac{1}{1 + 6.8\lambda/a} + 2\sigma_{dp} v_T n_b \tag{4.1}$$

where $a = d/2$ is the laser beam radius, D is the diffusion coefficient, $\lambda = 3D/v_T$ is the mean free path, σ_{dp} is the ground-state relaxation cross-section, $v_T = \sqrt{2k_B T/M}$ is the average thermal velocity of the ^{87}Rb atoms (k_B is the Boltzmann constant, T is the temperature of the cell and M is the molar mass of a ^{87}Rb atom), n_b is the density of the buffer gas atoms. For a room temperature ^{87}Rb vapor cell filled with 20 Torr N_2, as in our experiments, the minimum linewidth of the order of 1 kHz should be achieved. In more rigorous experiments, a very narrow linewidth below 50 Hz has been achieved in a cesium cell filled with 30 Torr neon buffer gas [55].

4.2.3 Modification to the selection rule

In the presence of a buffer gas at sufficiently high pressure, collisions between the buffer gas and atoms in an excited state cause a mixing of the excited state sublevels and modifies the selection rule for the Λ-system [3]. Figure 4.2 shows the dependence of the CPT signal on the light polarization at different buffer gas pressure in the absence of an external magnetic field. With linearly polarized light (at $\varphi = 0$ of the waveplate axis angle), the CPT signal is significantly reduced. At 13 mbar ($\approx$ 10 Torr) or higher pressure, the signal nearly vanishes. On the other hand, the maximum CPT signal occurs when the light is circularly polarized ($\varphi = 45°$). For this reason, circularly polarized light is used to prepare CPT in a cell with a buffer gas.

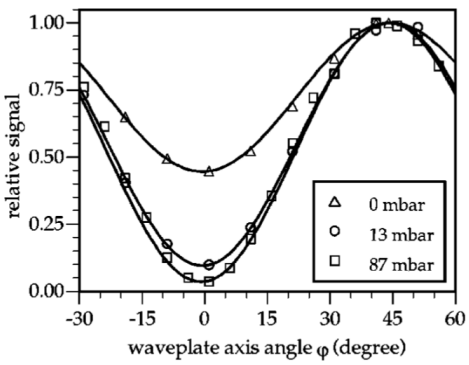

Figure 4.2: CPT signal as a function of light polarization at different buffer gas pressure. A magnetic field is set to zero. CPT signal is minimum (nearly vanished at higher buffer gas pressure) when the light is linearly polarized ($\varphi = 0°$). This maximum signal is obtained with circularly polarized light ($\varphi = 45°$). The figure is borrowed from Wynands et. al. [3].

4.2.4 "Trapping" the atomic population in the end state

When pumping with circular polarized light, a large portion of the atomic population is pumped towards sublevels with the maximum (or minimum) magnetic quantum number m_F. In the presence of a buffer gas, with a broadband excitation field, the optical pumping is more efficient because of the increased spectral overlap between the atomic resonance and the pulse spectrum as discussed above. This is beneficial for atomic magnetometers, as has been demonstrated in optically pumped magnetometers [20]. On the other hand, it may be detrimental for CPT-based atomic clocks which exploit the field-independent superposition, dubbed 0-0 superposition, formed between the sublevels with $m_F = 0$ magnetic quantum number. The strong optical pumping leaves little atomic population in the $m_F = 0$ sublevels. Consequently, the 0-0 CPT signal is significantly reduced, hindering the performance of the atomic clock operating on the 0-0 CPT signal.

4.3 Push-pull optical pumping

4.3.1 CPT preparation with polarization modulated light

Developed by Jau and Happer to improve the performance of the CPT-based atomic clocks, the push-pull optical pumping (PPOP) is an effective technique to optically pump a large portion of the atomic population into the 0-0 superposition states [4]. PPOP also addresses the issue encountered in the CPT-based IPI magnetometery: the effect of a sequence of alternating LCP and RCP pulses on a preparation of CPT. The principle of PPOP is analogous to the synchronous optical pumping scheme, first demonstrated by Bell and Bloom [17]. In the Bell-Bloom optical pumping experiments, a precession of macroscopic spin polarization is synchronously driven by a circularly polarized near-resonant light which is amplitude modulated at the Larmor frequency. In PPOP, the 0-0 superposition is coherently driven by a train of light pulses resonant with the D1 line in ^{87}Rb which alternates between LCP and RCP at the Bohr frequency, $\omega_{00} = (E_{a,0} - E_{b,0})/\hbar$, where a and b are the upper ($F = 2$) and lower ($F = 1$) hyperfine states, respectively (see Figure 2.1 for the energy diagram of the D1 line of ^{87}Rb). If the temporal separation between RCP and LCP light matches to one half of the oscillation period of the 0-0 superposition, $\tau = T_{00}/2$, where $T_{00} = 2\pi/\omega_{00}$, a very large portion of atoms is pumped into the superposition state.

4.3.2 0-0 superposition dark-state

The superposition between the sublevels with $m_F = 0$ can be expressed as

$$|\psi_{00}\rangle = \frac{|a\ 0\rangle\, e^{-iE_{a0}t/\hbar} + |b\ 0\rangle\, e^{-iE_{b0}t/\hbar}}{\sqrt{2}} \tag{4.2}$$

where $E_{a,0}$ and $E_{b,0}$ are the eigenenergy of the upper and lower hyperfine states, a and b, respectively. By choosing a relative phase between $|a\ 0\rangle$ and $|b\ 0\rangle$ such that $\langle a\ 0|\, S_z\, |b\ 0\rangle = 1/2$, the expectation value of the spin polarization along the beam direction (z-axis) is given by

$$\langle S_z \rangle = \frac{1}{2} \cos \omega_{00} t \tag{4.3}$$

The probability $\mathbb{P}$ of exciting a spin-polarized atom with a photon with spin s is:

$$\mathbb{P} \propto 1 - 2s \cdot \langle S \rangle \tag{4.4}$$

RCP and LCP light pulses in the propagation direction are σ_+ and σ_- photons and carry angular momentum with magnitude of $s = +1$ and $s = -1$ (in units of $\hbar$), respectively. Therefore, a relative probability of exciting the atoms prepared in the 0-0 superposition is given by

$$p_+ = \sin^2 \frac{\omega_{00} t}{2} \tag{4.5a}$$

$$p_- = \cos^2 \frac{\omega_{00} t}{2} \tag{4.5b}$$

If a RCP pulse arrives at the atoms which has been prepared in the 0-0 superposition state at $t = 0$, T_{00}, $2T_{00}$, $\cdots$, there is no probability for the atoms to absorb RCP light and to be excited. Likewise, if a LCP pulse arrives a half period later than RCP light at $t = \frac{1}{2}T_{00}$, $\frac{3}{2}T_{00}$, $\frac{5}{2}T_{00}$, $\cdots$, there is no probability for the atoms to absorb LCP light and to be excited. Therefore, a sequence of RCP and LCP light separated by a half period of the atomic oscillation therefore does not interact with the atoms in the 0-0 superposition state: the atoms are in a coherent dark-state for the sequence of RCP and LCP pulses. Atoms in other states absorb either RCP and LCP light, and are "pushed" and "pulled" between the sublevels with opposite polarity. Over time, the atoms accumulated in the $m_F = 0$ sublevels will be eventually pumped into the 0-0 superposition dark-state and trapped there for the decoherence time. A pictorial description of the PPOP scheme is shown in Figure 4.3. When

the pumping rate exceeds the spin decoherence rate, a large portion of the atomic population is pumped into the 0-0 superposition. A large CPT signal, which is 1 to 2 orders of magnitudes larger than those observed under the same conditions with conventional pumping, can be obtained from the 0-0 superposition dark-state in PPOP scheme [4].

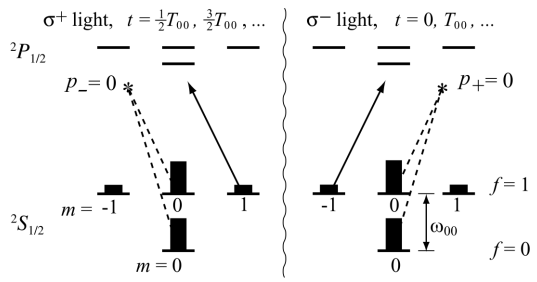

Figure 4.3: Push-pull optical pumping (PPOP) of the 0-0 superposition dark-state. The transition probability with LCP light (p_+) vanishes at every full oscillation period. For RCP, the probability (p_-) vanishes at every half oscillation period. By constructing a pulse train with RCP and LCP pulses with appropriate delay between each polarization, the atoms are pumped into the 0-0 superposition dark-state. This figure is borrowed from [4].

4.4 Experiment with a mode-locked pulse train

4.4.1 Experimental setup

Mode-locked laser

A pulse train is generated from a standard titanium-sapphire mode-locked laser. The pulse width is approximately 20 ps. The repetition rate is set closed to 126.6 MHz, which is 54th submultiple of the 6.8 GHz hyperfine splitting of ^{87}Rb and satisfies the condition for CPT, as described in chapter 2. In this case, the pulses arrive at the atoms in every 54 oscillation periods, which is $54 \times T_{00} \approx 7.9$ ns.

Polarization modulator

In order to generate a sequence of pulses with alternating circular polarizations and with an appropriate delay between them, the output of the laser is sent to a polarization modulator which is constructed from a Michelson interferometer and a set of wave plates, as shown in Figure 4.4. The p-polarized output beam from the laser is first rotated to 45° by a half-wave plate (HWP) at the entrance of the modulator. A polarizing beam splitter (PBS) splits the p-polarized and s-polarized components with equal intensity and sends them into the arms of the Michelson interferometer. Each arm contains one QWP, thus the output of the Michelson interferometer consists of a pulse train with orthogonal linear polarizations with a delay determined by the relative path length between the arms. Passed through another QWP at the exit of the modulator, each linear polarization becomes circularly polarized with opposite handness.

The delay can be varied over $\Delta L = 5$ cm or $\tau = c/2\Delta L = 300$ ps, which covers approximately 2 periods of the ground state coherent oscillation ($T_{00} = 146$ ps for ^{87}Rb). The zero delay is calibrated with respect to the peak of an intensity autocorrelation of the pulse train.

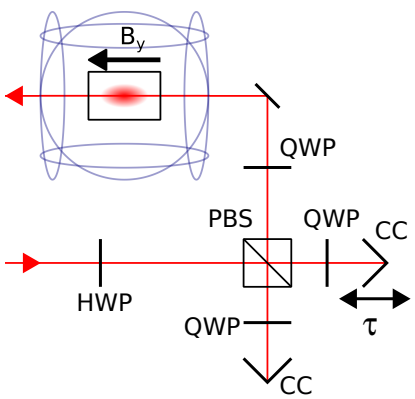

Figure 4.4: A sketch of the polarization modulator. HWP: half-wave plate, PBS: polarizing beam splitter, QWP: quarter-wave plate, CC: corner cube

Buffer gas cell

The ^{87}Rb vapor cells at different buffer gas pressure are prepared by a group lead by Prof. Gaetano Mileti at Université de Neuchâtel. The cells are made of 2 cm long Pyrex cylinder with 1.2 cm diameter windows made of a 1 mm thick parallel Pyrex plate with no anti-reflection coating. The cells (#3290 and #3291) are filled with 25 Torr and 40 Torr N_2 buffer gas. Their spectroscopic characteristics of CPT resonance are summarized in Table 4.1.

In order to achieve a good signal-noise ratio, the cells are heated to $\approx 40°$C to increase the number density of ^{87}Rb atoms. To prevent ^{87}Rb atoms from depositing on the windows, a pair of heaters is mounted on an extension tube which protrudes from each side of the cell body. A special care is given to remove ambient magnetic field generated from the heaters. The heaters initially used are a bifilar resistive heating wire which is very difficult to handle. For this experiment, the heating wire is replaced by a pair of commercial Kapton flexible heating tape (Omega KHLV-0504/10). It has an imprinted zigzag heating wire which eases the cell construction and generates sufficiently small magnetic field for this experiment. By reversing the currents in the two heaters, the magnetic field in the cell is minimized. The cell assembly is placed in a magnetic field of approximately 100 mG applied along the beam propagation, as shown in Figure 4.4.

Cell	Nominal N_2 pressure	Experimental N_2 pressure	Intrinsic linewidth
3290	33.3 mbar (25 Torr)	23.9 mbar (18 Torr)	1.059(5) kHz
3291	53.3 mbar (40 Torr)	51.7 mbar (39 Torr)	0.91(5)

Table 4.1: Specifications of the vapor cells provided by the Neuchâtel group.

4.4.2 Experimental results

Dependence of the CPT signal on delay between RCP and LCP

The first experiment is to investigate the dependence of the CPT signal strength on a delay τ between the RCP and LCP pulses. According to Eq. (4.5), the 0-0 superposition dark-state is formed when the delay is tuned to an integer multiple of a half period of the ground state oscillation. In this experiment, the D1 fluorescence is measured as a function of the delay, while the laser repetition rate is set at 54th submultiple of the ground state hyperfine splitting. The zero-delay is calibrated with an auto-correlation of the pulse train. Figure 4.5 shows the depth of CPT signal, which is defined as the height of the fluorescence signal at CPT resonance subtracted from the background signal, as a function of the delay between RCP and LCP. As expected from Eq. (4.5), the CPT strength periodically varies with the delay at a frequency corresponding to the ground state hyperfine splitting. The maximum CPT signal occurs when the delay is at every half integer of the ground state oscillation period, $\tau = M \times T_{00}/2 \approx M \times 73/2$ ps, where M is an integer. When the delay is an integer multiple of the oscillation period, the CPT signal vanishes completely. The zero-delay is equivalent to a train of linearly polarized pulses. As mentioned in Section 4.2.3, the modification to the selection rule in the presence of a buffer gas at sufficiently high pressure removes the dark-state for linearly polarized light. The extinction of the CPT signal also occurs at every integer multiple of $\tau = M \times T_{00}$. The oscillation of the CPT signal with the delay is expected to continue over many periods, because the ground state coherence time is several orders of magnitude longer than the temporal periods of the pulse train.

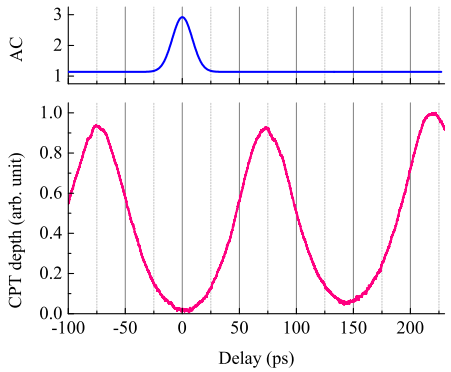

Figure 4.5: Depth of CPT signal as a function of delay between RCP and LCP pulses while the laser repetition rate is set to a submultiple of the 0-0 resonance. An auto-correlation of the pulse train is shown in the top panel for a calibration of the delay.

Line-shape of of CPT resonance

Figure 4.6 shows the CPT signal profile from the 0-0 superposition state measured for delays corresponding to the maximum (left) and minimum (right) CPT strength. In these measurements, the repetition rate is scanned across 1/54th of the ground state hyperfine splitting, while the delay between RCP and LCP is fixed at $\tau = 73$ ps for the maximum CPT signal and $\tau = 146$ ps for the minimum CPT signal. The average power of the excitation pulse train is reduced to a few mW using neutral density filters. The fluorescence signals are plotted with respect to the 54th harmonic of the repetition rate ($54 \times f_{rep}$).

With $\tau = 73$ ps for the maximum CPT strength, narrow CPT resonance occurs at the resonance for the 0-0 superposition dark-state. Because of the push-pull optical pumping scheme, the dark-state is primarily formed between the 0-0 superposition state. A zoom of the 0-0 superposition dark-state is shown in Figure 4.7, which reveals a narrow linewidth of 4.5 kHz. By further decreasing the average power of the excitation pulse train, 1 kHz linewidth is achieved, which is comparable to the measurement using a CW laser by the Neuchâtel group as listed in Table 4.1.

There are also small CPT resonances appeared on both sides of the 0-0 resonance at frequencies corresponding to the superposition between $m_F = -1$ and $m_F = +1$ sublevels. Apart from a broadened linewidth compared to the 0-0 resonance, which is due to an inhomogeneous magnetic field, the line-shape is different from Lorentzian and asymmetric. Similar asymmetric CPT line-shape has been reported in both numerical and experimental studies where two excitation fields applied to each optical transition of the Λ-system are detuned from the optical resonance and have unequal intensities (different Rabi frequencies) [56]. In the experiment presented here, the atoms in $m_F = \pm 1$ sublevels are driven by RCP and LCP pulses, with RCP pulses driving transitions to $m'_F = m_F + 1$ sublevels and LCP driving transitions to $m'_F = m_F + 1$ sublevels. Since the magnitude of the Clebsh-Gordan coefficients are different between those transitions driven by RCP and LCP [5], the Rabi frequencies associated with each polarization are different. That is the origin of the asymmetric line-shape. As a matter of fact, the 0-0 resonance in which the Crebsh-Gordan coefficients are equal in magnitude for transitions driven by RCP and LCP, the symmetric line-shape is obtained. As the average power is increased, both the depth and linewidth increase, and the asymmetric resonance structure becomes indistinguishable.

With $\tau = 146$ ps for the minimum CPT strength (right panel in Figure 4.6), there is absolutely no dark-resonance. The slight increase of the fluorescence level with delay is merely due to misalignment of the Michelson interferometer over the long delay scan.

Power dependence

The dependence of the contrast and the linewidth on the average power of the excitation pulse train is characterized. The input power, measured at the entrance of the vapor cell, is controlled with neutral density filters. The contrast is measured as

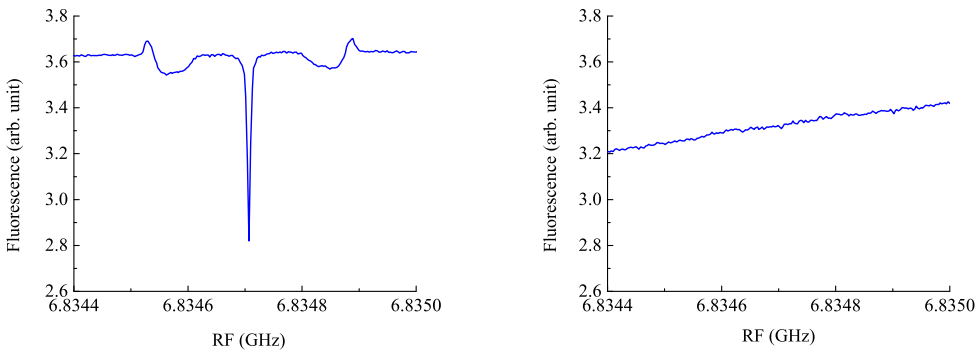

Figure 4.6: CPT signal from the 0-0 superposition state as a function of radio frequency (RF) which is $54 \times f_{rep}$, where f_{rep} is the repetition rate of the laser, for the delay between RCP and LCP fixed at 73 ps for maximum CPT strength (left) and at 146 ps for minimum CPT strength (right).

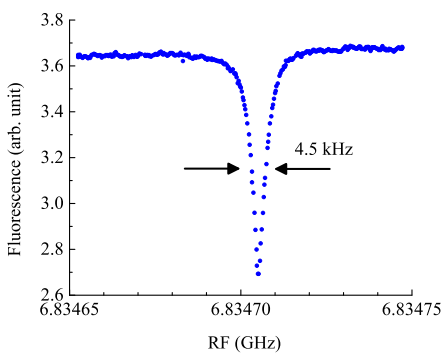

Figure 4.7: A zoom into the region of the dark resonance in the left panel in Figure 4.6, corresponding to $\tau = 73$ ps delay between RCP and LCP.

the ratio of the depth of the CPT resonance to the off-resonance fluorescence level above noise floor. The linewidth is measured as FWHM of the resonance.

Left panel in Figure 4.8 shows the CPT contrast as a function of the average laser power. The contrast increases linearly at low power, begins to saturate approximately at 20 mW and starts to decrease with the power at 40 mW. This trend is consistent with the result reported in ref. [54], although a CW laser was used in the study.

The decreasing contrast at higher power is due to a loss of population out of the 0-0 superposition state by the optical pumping, which is evident from the increased CPT depth from the superposition state between $m = +1$ and $m = -1$ sublevels at higher power (not shown in the figure).

The right panel in Figure 4.8 shows the power dependence of the CPT linewidth. The linewidth increases linearly with the average power of the excitation pulse train, which agrees with the linear dependence on the Rabi frequency given by the solution of the density matrix equations [54]. The minimum linewidth is 1.3 kHz at less than 1 mW input power, is comparable with the nominal linewidth measured by Neuchâtel group.

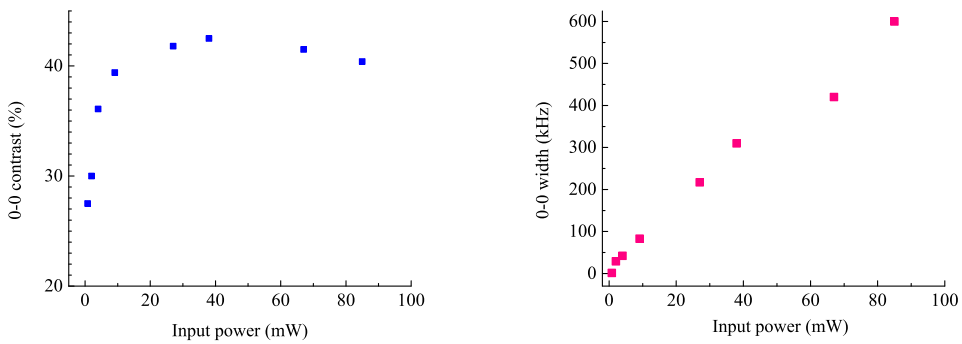

Figure 4.8: Power dependence of 0-0 resonance contrast (left) and linewidth (right) excited by a mode-locked pulse train using the push-pull optical pumping.

4.5 Conclusion

The question of the effect of alternating RCP and LCP pulses in a preparation of a spin polarized CPT medium is addressed experimentally. By scanning the repetition rate around 54th submultiple of the ground state hyperfine splitting while tuning a delay between equal intensity RCP and LCP pulses to a half period of the inverse of

the Bohr frequency, a large CPT signal is obtained from the 0-0 superposition state. Since the atomic population is pumped out of sublevels with $m_F \neq 0$, a very small CPT signal is obtained from the superposition state of the magnetic filed sensitive sublevels. For characterization of the 0-0 resonance, the power dependence of CPT contrast and the linewidth are analysed, which is consistent with previously reported results.

In conclusion, this optical pumping scheme, known as the push-pull optical pumping (PPOP), is an effective approach to enhance the performance of the CPT-based atomic clock, however is not suitable for implementation of a magnetometer as it leaves the magnetic sublevels nearly empty.

Chapter 5

Intracavity interaction between mode-locked pulses and ^{87}Rb vapor

5.1 Introduction

Towards the ultimate goal of realizing a high-sensitive atomic magnetometer based on the IPI technique, it is important to understand the interaction between a mode-locked pulse train and the atomic sample *inside* a mode-locked laser cavity, and its effect to the dynamics of the mode-locking operation.

According to the density matrix equations, a resonant electric field induces an instantaneous polarization of an ensemble of atoms. In a time scale of the ultrashort pulses ($10^{-14} \sim 10^{-11}$ second), which is comparable or shorter than the phase coherence time, the induced ensemble polarization evolves coherently with the applied electric field (i.e. the phase between the ensemble polarization and the field is preserved). According to the Maxwell's equations, such polarization radiates into the field and induces absorption (or amplification) and dispersion which depend on the local field strength. Consequently, resonant propagation of ultrashort pulses of-

ten hosts the exotic nonlinear optical effects, including transparency of an absorbing medium [57] and generation of a slow-light [30] whose velocity is significantly less than in linear optics. Taking place inside a mode-locked laser cavity, those nonlinear propagation effects can impact the operation of the laser sensor based on IPI.

This chapter presents new studies of coherent propagation of a mode-locked pulse train in a ^{87}Rb vapor which is placed in a mode-locked laser cavity. The chapter begins with providing a theoretical background based on the Maxwell-Bloch equations for descriptions of coherent pulse propagation in a resonant medium, followed by numerical simulations of picosecond pulse propagation in a three-level system. Experimental observations of the intracavity coherent propagation phenomena, including a pulse shaping effect and slow-light propagation, are presented. Those effects are characterized by "area" of the pulses. Lastly, a demonstration of intracavity coherent populatiotrapping (CPT) of ^{87}Rb atoms is presented.

5.2 Coherent propagation of ultrashort pulses

5.2.1 Maxwell-Bloch equations

Propagation of an electromagnetic field in an atomic ensemble is described by the Maxwell's wave equation [58]. When a propagation in z-direction is considered,

$$\left(\frac{\partial^2}{\partial t^2} - \frac{1}{c^2}\frac{\partial^2}{\partial t^2}\right) E(t,z) = \mu_0 \frac{\partial^2}{\partial t^2} P(t,z) \tag{5.1}$$

where the real electric field $E(t,z)$ and the ensemble polarization $P(t,z)$ are defined as

$$E(t,z) = \frac{1}{2}\tilde{\mathcal{E}} e^{i\omega_\ell t} + c.c. \tag{5.2}$$

$$P(t,z) = \frac{1}{2}\tilde{\mathcal{P}} e^{i\omega_\ell t} + c.c. \tag{5.3}$$

$\tilde{\mathcal{E}}$ and $\tilde{\mathcal{P}}$ are complex slow varying envelopes of the electric field and polarization, respectively.

For propagation of ultrashort pulses whose duration is longer than a few optical cycles, Eq. (5.1) is simplified to the *reduced* wave equation [58],

$$\frac{\partial}{\partial z}\tilde{\mathcal{E}}(t,z) = -i\frac{\mu_0\omega_\ell c}{2n}\tilde{\mathcal{P}}(t,z) \tag{5.4}$$

where the slowly varying envelope approximation (SVEA) and the transformation of the time coordinate into a retarded frame of reference which is moving with the pulse envelope have been made.

In a general case, the complex electric field and polarization envelope may be expressed as

$$\tilde{\mathcal{E}} = \mathcal{E}e^{i\varphi} \tag{5.5}$$

$$i\tilde{\mathcal{P}} = \tilde{\mathcal{Q}} = (iu + v)e^{i\varphi} \tag{5.6}$$

where u and v are the real quantities of the complex polarization that oscillate out-of-phase and in-phase with the electric field, respectively. φ accounts for a variation of optical phase. The reduced wave equation in Eq. (5.4) can be written as

$$\frac{\partial}{\partial z}\tilde{\mathcal{E}}(t,z) = -\frac{\mu_0\omega_\ell c}{2n}\tilde{\mathcal{Q}}(t,z) \tag{5.7}$$

which is a statement that the action of the polarization is to oppose the electric field. In terms of the real quantities, the equations for the envelope and phase are give by

$$\frac{\partial\mathcal{E}}{\partial z} = -\frac{\mu_0\omega_\ell c}{2c}v \tag{5.8a}$$

$$\frac{\partial\varphi}{\partial z} = -\frac{\mu_0\omega_\ell c}{2n}\frac{u}{\mathcal{E}} \tag{5.8b}$$

Eq. (5.8a)-(5.8b) indicate that v is responsible for absorption (or gain), and u is responsible for phase retardation (or advancement).

The ensemble polarization $P(t, z)$ in Eq. (5.1) is given by

$$P = \bar{N} \langle \hat{p} \rangle = \bar{N} \mathrm{Tr}(\hat{\rho}\hat{p}) \tag{5.9}$$

where $\bar{N}$ is the number density of the atomic ensemble, $\langle \hat{p} \rangle$ is the expectation value of the quantum mechanical dipole operator $\hat{p}$, which is given by a trace of the matrix product of $\hat{p}$ with the density matrix operator $\hat{\rho}$. Time evolution of the density matrix is given by the density matrix equation, Eq. 2.9 in Section 2.3. The set of equations in Eq. (5.4) and Eq. (2.9) is known as the Maxwell-Bloch equations, which provides theoretical basis for the experiments presented in this chapter.

5.2.2 Two-level atoms

Optical Bloch equations

Despite its simplicity, the two-level system model captures most of the important physics of light-atom interaction [46]. An ensemble of two-level atoms is represented by a 2×2 density matrix

$$\hat{\rho} = \begin{pmatrix} \rho_{11} & \tilde{\rho}_{12} \\ \tilde{\rho}_{21} & \rho_{22} \end{pmatrix} \tag{5.10}$$

Time evolution of each matrix element is given by

$$\begin{aligned}
\frac{d\rho_{11}}{dt} &= -\frac{i}{\hbar}(\tilde{V}_{21}^{*}\tilde{\rho}_{21} - \tilde{\rho}_{21}^{*}\tilde{V}_{21}) + \Gamma_2\rho_{22} \\
&= -\frac{2p_{21}}{\hbar}\mathrm{Im}(\tilde{E}^{*}\tilde{\rho}_{21}) + \Gamma_2\rho_{22} && (5.11a) \\
\frac{d\rho_{22}}{dt} &= -\frac{i}{\hbar}(\tilde{V}_{21}\tilde{\rho}_{21}^{*} - \tilde{\rho}_{21}\tilde{V}_{21}^{*}) - \Gamma_2\rho_{22} \\
&= \frac{2p_{21}}{\hbar}\mathrm{Im}(\tilde{E}^{*}\tilde{\rho}_{21}) - \Gamma_2\rho_{22} && (5.11b) \\
\frac{d\tilde{\rho}_{21}}{dt} &= i(\omega_2 - \omega_1)\tilde{\rho}_{21} - i\frac{\tilde{V}_{21}^{*}}{\hbar}(\rho_{22} - \rho_{11}) - \Gamma_{21}\rho_{21} \\
&= i\omega_{21}\tilde{\rho}_{21} - i\frac{p_{21}\tilde{E}^{*}}{\hbar}(\rho_{22} - \rho_{11}) - \Gamma_{21}\rho_{21} && (5.11c) \\
\frac{d\tilde{\rho}_{12}}{dt} &= -i\omega_{21}\tilde{\rho}_{12} + i\frac{p_{12}\tilde{E}}{\hbar}(\rho_{22} - \rho_{11}) - \Gamma_{12}\rho_{12} = \frac{d\tilde{\rho}_{21}^{*}}{dt} && (5.11d)
\end{aligned}$$

where Γ_2 is the relaxation rate of the population in $|2\rangle$ and and $\Gamma_{21} = \Gamma_{12}$ is the relaxation rate of the coherence between $|1\rangle$ and $|2\rangle$. To simplify their form, $\mathrm{Im}(z) = -i(z - z^{*})/2$ and $\omega_{21} = \omega_2 - \omega_1$ are used.

Since the time evolution in a scale much longer than optical oscillation is only relevant here, $\tilde{\rho}_{21}$ and $\tilde{E}$ are expressed in terms of a slowly varying envelope and rapidly varying oscillating term:

$$\tilde{\rho}_{21} = \frac{1}{2}\tilde{\sigma}_{21}e^{i\omega_\ell} \tag{5.12}$$

$$\tilde{E} = \frac{1}{2}\tilde{\mathcal{E}}e^{i\omega_\ell} \tag{5.13}$$

By doing this transformation, the fast oscillating terms can be eliminated from Eq. (5.11), a procedure known as the rotating wave approximation (RWA). The equations of population and the slowly varying envelopes of coherence become

$$\begin{aligned}
\frac{d\rho_{11}}{dt} &= -\frac{1}{2}\mathrm{Im}(\kappa\tilde{\mathcal{E}}^{*}\tilde{\sigma}_{21}) + \Gamma_2\rho_{22} && (5.14a) \\
\frac{d\rho_{22}}{dt} &= \frac{1}{2}\mathrm{Im}(\kappa\tilde{\mathcal{E}}^{*}\tilde{\sigma}_{21}) - \Gamma_2\rho_{22} && (5.14b) \\
\frac{d\tilde{\sigma}_{21}}{dt} &= -(\Gamma_{21} - i\Delta)\tilde{\sigma}_{21} + i\kappa\tilde{\mathcal{E}}^{*}(\rho_{22} - \rho_{11}) && (5.14c)
\end{aligned}$$

where $\kappa = p_{ij}/\hbar$ and $\Delta = \omega_{21} - \omega_\ell$ is the detuning between the optical frequency and the atomic resonance. $\kappa\tilde{\mathcal{E}}$ is identified as the Rabi frequency.

Pseudo-polarization vector

There is a geometrical representation of the two-level system undergoing a coherent evolution, the concept first applied to describe a precession of nuclear spins in nuclear magnetic resonance experiments [59]. From Eq. (5.6) and Eq. (5.9), it can be shown that in RWA,

$$(iu + v)e^{i\varphi} = ip\bar{N}\tilde{\sigma}_{21} \tag{5.15}$$

Now, a new variable w is introduced for the normalized population inversion:

$$w = p\bar{N}(\rho_{22} - \rho_{11}) \tag{5.16}$$

Substituting into Eq. (5.14), and ignoring the relaxation terms, a set of differential equations for three orthogonal variables, u, v and w is derived:

$$\dot{u} = \Delta\omega v \tag{5.17a}$$

$$\dot{v} = -\Delta\omega u - \kappa\mathcal{E}w \tag{5.17b}$$

$$\dot{w} = \kappa\mathcal{E}v \tag{5.17c}$$

where $\Delta\omega = \Delta - \dot{\varphi}$. Eq. (5.17a)-(5.17c) are known as the optical Bloch equations. They can be compactly written as a cross-product of two vectors:

$$\frac{\partial\vec{\mathcal{W}}}{\partial t} = \vec{\mathcal{E}}_{\text{fic}} \times \vec{\mathcal{W}} \tag{5.18}$$

where a pseudo-polarization vector, also known as the optical Bloch vector, is defined as

$$\vec{\mathcal{W}} = (u, v, w) \tag{5.19}$$

and a fictitious torque electric field vector is defined as

$$\vec{\mathcal{E}}_{\text{fic}} = (\kappa\mathcal{E}, 0, -\Delta\omega) \tag{5.20}$$

Eq. (5.18) is mathematically equivalent to the equation for a precession of an angular momentum vector around a torque vector, e.g. a precession of a spin polarization. Indeed, a coherent interaction between a two-level system and an electric field can be interpreted in terms of a precession of the pseudo-polarization vector $\vec{\mathcal{W}}$ about a fictitious electric field vector $\vec{\mathcal{E}}$. From Eq. (5.18), the precession frequency (the Rabi frequency) can be identified as

$$\Omega_{Rabi} = \sqrt{(\kappa\mathcal{E})^2 + \Delta\omega^2} \tag{5.21}$$

For a resonant interaction, in which $\Delta = 0$, the optical Bloch equations in Eq. (5.17a)-(5.17c) reduce to a simple coupled equations of v and w

$$\dot{v} = -\kappa\mathcal{E}w \tag{5.22a}$$

$$\dot{w} = \kappa\tilde{\mathcal{E}}v \tag{5.22b}$$

If the system is initially in the ground state, the solution of Eq. (5.22) is

$$v = -\sin\theta(t) \tag{5.23a}$$

$$w = -\cos\theta(t) \tag{5.23b}$$

where

$$\theta(t) = \int_{-\infty}^{\infty} \kappa\mathcal{E}(t')dt' \tag{5.24}$$

which defines the "area" of a resonant pulse. It can be shown that in the frequency domain θ is defined as

$$\theta = \kappa\mathcal{E}(\omega_\ell) \tag{5.25}$$

where ω_ℓ is the center frequency of the pulse. θ can be also identified as the tipping angle of the pseudo-polarization vector $\vec{\mathcal{W}}$, since

$$\theta = \tan^{-1}\left(\frac{v}{w}\right) = \tan^{-1}\left(\frac{-\sin\theta}{-\cos\theta}\right) \tag{5.26}$$

Therefore, the action of a resonant pulse on a two-level system is to rotate the pseudo-polarization vector $\vec{\mathcal{W}}$ in the vw plane by the angle determined by Eq. (5.24).

Since the cross-product of two vectors is orthogonal to both vectors, $\dot{\vec{\mathcal{W}}} \cdot \vec{\mathcal{W}} = 0$, which indicates that $|\vec{\mathcal{W}}|^2$ is constant. The conservation of population also implies that $|\vec{\mathcal{W}}|^2 = 1$. Therefore, in the absence of relaxation processes, the length of the pseudo-polarization vector is a constant of motion and unity:

$$|\vec{\mathcal{W}}|^2 = |u|^2 + |v|^2 + |w|^2 = 1 \tag{5.27}$$

The tip of $\vec{\mathcal{W}}$ traverses on the surface of a sphere with unit radius, known as the Bloch sphere.

In general, the energy can be dissipated into the bath and the atomic population can be lost outside of the system. Those relaxation processes are customarily described in terms of phenomenological relaxation time constant, T_1 for the energy relaxation, and T_2 for the phase relaxation. In the absence of relaxation processes, except for collisions among the atomic themselves, the phase relaxation time is twice the energy relaxation time: $T_2 = 2T_1$. With the phenomenological relaxation constants, the optical Bloch equations become

$$\dot{u} = \Delta\omega v - \frac{u}{T_2} \tag{5.28a}$$

$$\dot{v} = -\Delta\omega u - \kappa\mathcal{E} w - \frac{v}{T_2} \tag{5.28b}$$

$$\dot{w} = \kappa\mathcal{E} v - \frac{w - w_0}{T_1} \tag{5.28c}$$

where w_0 is the population inversion at equilibrium.

To include inhomogeneous line broadening due, for example, to a distribution of thermal velocities of atoms (Doppler broadening), other sets of optical Bloch equations with different detuning $\Delta' = \Delta + \delta_{ih}$ are considered and integrated over the inhomogeneous linewidth.

Steady-state solutions

If the temporal variation of the envelope of a pulse is much slower than $T_2 \approx 1/(2\pi \times 500\ \text{MHz})$ for ^{87}Rb , Eq. (5.17a) and Eq. (5.17b) reach a steady state in the time scale of the pulse[1]. Solving for u and v for the steady state;

$$u^{s.s} = -\frac{\kappa\mathcal{E}T_2^2\Delta\omega w}{1+T_2^2\Delta\omega^2} \tag{5.29}$$

$$v^{s.s} = -\frac{\kappa\mathcal{E}T_2 w}{1+T_2^2\Delta\omega^2} \tag{5.30}$$

Substituting into Eq. (5.28c), the equation for the population inversion is obtained:

$$\dot{w} = -\frac{\mathcal{E}^2(\kappa^2 T_1 T_2)}{1+\Delta\omega^2 T_2^2}\frac{w}{T_1} - \frac{w-w_0}{T_1} \tag{5.31}$$

Eq. (5.31) is identical to the rate equation that is often encountered in laser textbooks where w is replaced with ΔN [60]. The saturation field is defined as

$$\mathcal{E}_{s0} = \frac{1}{\kappa\sqrt{T_1 T_2}} \tag{5.32}$$

for on-resonance case. For off-resonance case it is increased by

$$\mathcal{E}_s = \mathcal{E}_{s0}\sqrt{1+\Delta\omega^2 T_2^2} \tag{5.33}$$

The steady-state solution for w is give by

$$w^{s.s} = \frac{1+\Delta\omega^2 T_2^2}{1+\Delta\omega^2 T_2^2 + (\kappa\mathcal{E})^2 T_1 T_2} w_0 \tag{5.34}$$

[1]In the experiments presented in this chapter, the atomic system does not reach a steady-state for interaction with a picosecond pulse. However, the steady-state solution provides α_0 which is an important parameter in the area theorem in Section 5.2.3.

From Eq. (5.29), Eq. (5.30) and Eq. (5.34), it is clear that linear optics is described by the steady-state solutions.

Absorption coefficient

Now, if both sides of Eq. (5.8a) are multiplied by $\mathcal{E}^*$ and substituted with the steady-state solutions in Eq. (5.29)-(5.30) and Eq. (5.34), the Beer's law of linear absorption is found:

$$\begin{aligned}\frac{\partial|\mathcal{E}|^2}{\partial z} &= -\frac{\mu_0\omega_\ell c}{2n}v^{s.s}\mathcal{E}^* \\ &= \frac{\mu_0\omega_\ell c T_2\kappa w_0}{2n}\frac{|\mathcal{E}|^2}{1+\Delta\omega^2T_2^2+(\mathcal{E}\kappa)^2T_1T_2} \\ &= \alpha_0\frac{|\mathcal{E}|^2}{1+\Delta\omega^2T_2^2+(\mathcal{E}\kappa)^2T_1T_2}\end{aligned} \tag{5.35}$$

where

$$\alpha_0 = \frac{\mu_0\omega_\ell c T_2\kappa w_0}{2n} \tag{5.36}$$

is the unsaturated absorption coefficient.

5.2.3 Pulse propagation in two-level atoms

Self-induced transparency

Self-induced transparency (SIT) is a remarkable example of nonlinear transparency effect observed in the propagation of an ultrashort pulse in an absorbing medium. SIT was discovered by McCall and Hahn [57] in late 1960's. They demonstrated anomalously low loss propagation of an intense resonant optical short pulse in a cryogenically cooled ruby crystal. It was found that the transparency occurs if a resonant pulse was sufficiently short and intense such that a full cycle of energy

exchange between the pulse and crystal's ions took place before the system dissipated energy into the bath. They also formulated a propagation law of the area θ in an inhomogeneously broadened medium. They discovered a self-consistent solution to the Maxwell-Bloch equations, from which a stable pulse envelope shape was derived. Since its discovery, a number of both experimental and theoretical studies have been carried out with different medium including atomic gases [61] and semiconductors [62]. Intracavity SIT has been also studied theoretically in the context of development of new laser sources [63].

Area theorem

A propagation of a short pulse in an inhomogeneous resonant two-level system is described by the reduced wave equation with an inhomogeneous broadening lineshape function $g_{inh}(\omega_0' - \omega_{ih})$;

$$\frac{\partial \tilde{\mathcal{E}}}{\partial z} = -\frac{\mu_0 \omega_\ell c}{2n} \int_{\omega_{ih}} \tilde{\mathcal{Q}}(\omega_0') g_{inh}(\omega_0' - \omega_{ih}) d\omega_0' \tag{5.37}$$

where

$$\int_{-\infty}^{\infty} g(\omega_0' - \omega_{ih}) d\omega_0' = 1 \tag{5.38}$$

The equations for the amplitude and phase are

$$\frac{\partial \mathcal{E}}{\partial z} = -\frac{\mu_0 \omega_\ell c}{2c} \int_{\omega_{ih}} v(\omega_0') g_{inh}(\omega_0' - \omega_{ih}) d\omega_0' \tag{5.39a}$$

$$\frac{\partial \varphi}{\partial z} = -\frac{\mu_0 \omega_\ell c}{2n} \int_{\omega_{ih}} \frac{u(\omega_0')}{\mathcal{E}} g_{inh}(\omega_0' - \omega_{ih}) d\omega_0' \tag{5.39b}$$

When the pulse duration is shorter than both relaxations times, T_1 and T_2, no energy is dissipated into a bath in the time scale of the pulse. In addition, if the pulse duration is longer than the inhomogeneous relaxation time $T_2^* = 1/\Delta_{ih}$, the inhomogeneous line shape does not vary significantly over the pulse spectrum. In

this limit, there is a conservation law for the area, known as the *area theorem*[57], as following.

The propagation equation for the field envelope in Eq. (5.39a), after multiplying both sides by κ and integrating in time, leads to the propagation equation for the area,

$$\frac{d\theta}{dz} = \frac{\alpha_0}{2}\sin\theta \tag{5.40}$$

which has the general solution

$$\theta(z) = 2\tan^{-1}\left[\tan(\theta_0/2)e^{-\alpha_0 z/2}\right] \tag{5.41}$$

where θ_0 is the initial area at the entrance to the medium (z=0) and α_0 is the absorption coefficient given in Eq. (5.36). With a small initial area ($\theta \ll 1$), Eq. (5.41) turns into the propagation law for a low intensity or incoherent pulse, i.e. the Beer's law:

$$I(z) = I_0 e^{-\alpha_0 z} \tag{5.42}$$

The graphical representation of the solution in Eq. (5.41) is shown in Figure 5.1. A remarkable prediction of the area theorem is that the area evolves towards an even integer multiple of π (0, 2π, 4π, $\cdots$) in an absorber and an odd integer multiple of π (π, 3π, 5π, $\cdots$) in an amplifier. An input pulse with the area of an even integer of π preserves its area in an absorber, that is the steady-state solution to Eq. (5.40), while a pulse with the area of an odd integer of π is the steady-solution in an amplifier with opposite sign of α in Eq. (5.40).

2π-pulse

In particular, there is a self-consistent stable solution of the Maxwell-Bloch equations in Eq. (5.7) and Eq. (5.17a)-(5.17c) for a pulse with $\theta = 2\pi$, dubbed a "2π-pulse".

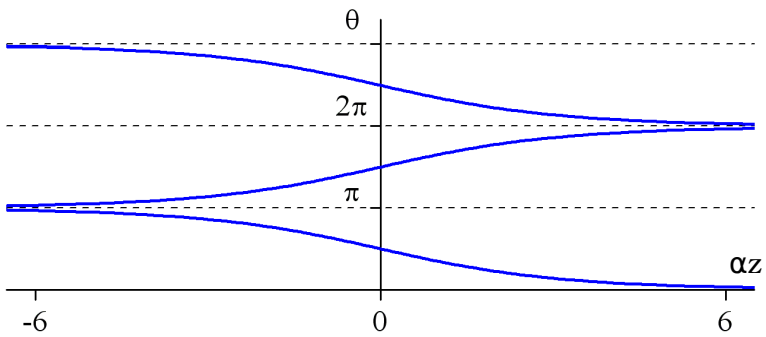

Figure 5.1: Graphical representation of Eq. (5.41) showing the evolution of area over many absorption length.

The self-consistent solution for propagation of a 2π-pulse in an absorber is given by

$$\mathcal{E}(t,z) = \frac{2}{\kappa\tau_s}\text{sech}\left(\frac{t}{\tau_s} - \frac{z}{\tau_s\mathcal{V}}\right) \tag{5.43}$$

where τ_s is the width of a hyperbolic secant pulse envelope and $\mathcal{V} = 2/(\alpha_0\tau_s) \ll c$ is the envelope velocity. It is clear that the envelope experiences a delay, in the retarded frame, given by

$$\tau = \alpha_0\tau_s L/2 \tag{5.44}$$

Thus, propagating over one absorption length ($L = \alpha_0^{-1}$), a 2π-pulse will delay by as much as a half of its width. The cause of the slow-light propagation is explained by an exchange of energy between the 2π-pulse and the atomic system. The first half of the 2π-pulse is absorbed by the atoms, which rotates the pseudo-polarization vector by π. It is followed by a coherent radiation of the pseudo-polarization, which adds to the rear end of the pulse, while rotating the pseudo-polarization vector by another π. Therefore, a 2π-pulse experiences significant reduction of its propagation velocity, while rotating the atomic polarization by a full 2π and leaving the entire population in the ground state.

0π-pulse

Another interesting propagation is one for a 0π-pulse. It is more common for narrow lines ($t_p \ll T_2^*$), for which it is somewhat trivial, because it is a linear effect. For broad lines, there is still and anomalous absorption. A 0π-pulse has zero spectral component at the atomic resonance frequency:

$$\theta = \kappa\mathcal{E}(\omega_\ell) = 0 \tag{5.45}$$

Numerical integration of the Maxwell-Bloch equations

Figure 5.2 shows numerical solutions of the Maxwell-Bloch equations for a long pulse ($T_2^* < t_p$) for three different values of input area. The input envelope is a hyperbolic secant with width of $\tau_p = 2.5$ ns, with no detuning $\Delta\omega = 0$. For an input area smaller than 2π, the pulse experiences a significant absorption after propagating over one absorption length, as shown in the left panel. Its area evolve towards $\theta = 0$, as predicted by the area theorem Eq. (5.40), which is evident by a small pulse created sometime later with a π shifted phase.

When an input area is greater than 2π, the pulse is shaped such that the area evolves towards 2π, as shown in the right panel. A pulse with initial area 2.5π experiences a pulse compression, while the peak intensity increases. The time integral of the field envelope times κ shows that the area evolve towards 2π in agreement with the area theorem.

For a 2π-pulse as shown in the middle panel, no pulse shaping occurs since it is the stable solution, except for a delay on the order of the pulse width, as predicted by Eq. (5.44). The area is a constant of motion in this case.

For propagation of an ultrashort pulse ($t_p \ll T_2^*$), the Maxwell-Bloch equations in Eq. (5.7) and Eq. (5.17a)-(5.17c) must be numerically integrated simultaneously.

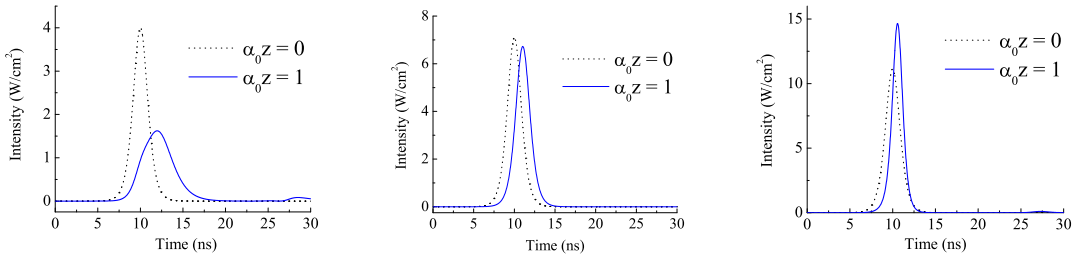

Figure 5.2: Coherent propagation of a 2.5 ns pulse with the area (left) $\theta = 1.5\pi$, (middle) $\theta = 2\pi$ and (right) $\theta = 2.5\pi$ over one absorption length ($\alpha z = 1$).

Figure 5.3 shows numerical solutions of the Maxwell-Bloch equations for an ultrashort pulse for three different values of input area. An ultrashort pulse whose width is much shorter than the inhomogeneous relaxation time, $t_p \ll T_2^*$, takes much longer propagation distance to reshape, because its spectral overlap with an inhomogeneously broadened atomic line is much less than the long-pulse case. For a 30 ps 2π-pulse, it take approximately 40 absorption length to experience pulse shaping effect to a similar extent to the narrow-line limit case.

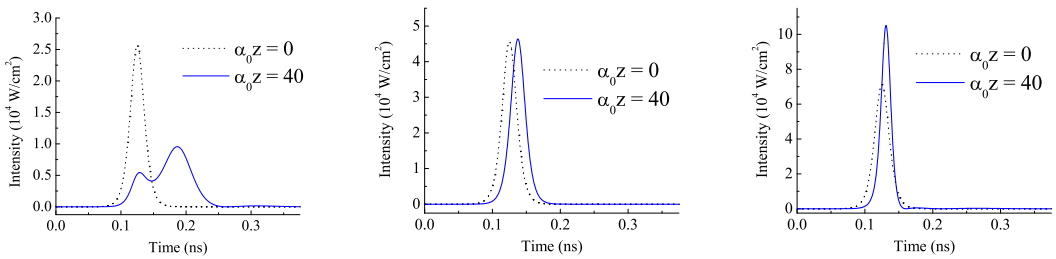

Figure 5.3: Coherent propagation of an ultrashort (ps) pulse with the area (left) $\theta = 1.5\pi$, (middle) $\theta = 2\pi$ and (right) $\theta = 2.5\pi$ over many absorption lengths ($\alpha z = 40$).

5.2.4 Pulse propagation in a ^{87}Rb vapor

Maxwell-Bloch equation for three-level atoms

In reality, ^{87}Rb has more than two energy levels. For interaction with a picosecond pulse at room temperature or at higher temperatures, ^{87}Rb is well represented by a three-level Λ-system. The density matrix equation is then

$$\frac{d\rho_{11}}{dt} = -\frac{\kappa}{2}\mathrm{Im}(\tilde{\mathcal{E}}^*\tilde{\sigma}_{31}) + \frac{\Gamma_3}{2}\rho_{33} \tag{5.46a}$$

$$\frac{d\rho_{22}}{dt} = -\frac{\kappa}{2}\mathrm{Im}(\tilde{\mathcal{E}}^*\tilde{\sigma}_{32}) + \frac{\Gamma_3}{2}\rho_{33} \tag{5.46b}$$

$$\frac{d\rho_{33}}{dt} = \frac{\kappa}{2}\mathrm{Im}(\tilde{\mathcal{E}}^*\tilde{\sigma}_{31}) + \frac{\kappa}{2}\mathrm{Im}(\tilde{\mathcal{E}}^*\tilde{\sigma}_{32}) - \Gamma_3\rho_{33} \tag{5.46c}$$

$$\frac{d\tilde{\sigma}_{31}}{dt} = (-\Gamma_{31} - i\Delta_{13})\tilde{\sigma}_{31} - i\kappa\tilde{\mathcal{E}}(\rho_{33} - \rho_{11}) + i\kappa\tilde{\mathcal{E}}\tilde{\rho}_{21} \tag{5.46d}$$

$$\frac{d\tilde{\sigma}_{32}}{dt} = (-\Gamma_{32} - i\Delta_{23})\tilde{\sigma}_{32} - i\kappa\tilde{\mathcal{E}}(\rho_{33} - \rho_{22}) + i\kappa\tilde{\mathcal{E}}\tilde{\rho}^*_{21} \tag{5.46e}$$

$$\frac{d\tilde{\rho}_{21}}{dt} = (-\Gamma_{21} - i\Delta_{12})\tilde{\rho}_{21} - i\frac{\kappa}{4}\tilde{\mathcal{E}}^*\sigma_{31} - i\frac{\kappa}{4}\tilde{\mathcal{E}}\tilde{\sigma}^*_{32} \tag{5.46f}$$

The propagation of a pico-second pulse in a ^{87}Rb vapor is described by the the reduced wave equation,

$$\begin{aligned}\frac{\partial\tilde{\mathcal{E}}}{\partial z} &= -\frac{\mu_0\omega_\ell c}{2n}\int_0^\infty \tilde{\mathcal{Q}}(\omega_0')g_{inh}(\omega_0' - \omega_{ih})d\omega_0' \\ &= -i\frac{\mu_0\omega_\ell c}{2n}\bar{N}\int_0^\infty g_{inh}(\omega_0' - \omega_{ih})[\sigma_{13}(\omega_0')p_{13} + \sigma_{23}(\omega_0')p_{23}]d\omega_0'\end{aligned} \tag{5.47}$$

where

$$\tilde{\mathcal{Q}} = i\bar{N}[\tilde{\sigma}_{13}p_{13} + \tilde{\sigma}_{23}p_{23}] \tag{5.48}$$

is the atomic polarization of ^{87}Rb in the rotating frame.

5.3 Intracavity experiments with ^{87}Rb vapor

5.3.1 Experimental setup

Experiments are performed using a home-built linear Ti:Sapphire mode-locked laser, shown in Figure 5.4. The laser cavity is designed to produce a train of $1 \sim 5$ ps pulses at a repetition rate between 121 MHz and 127 MHz. The average output power of the laser is on the order of 100 mW. With a $R = 96\%$ output coupler, the intracavity power should be on the order of several watts.

A ^{87}Rb vapor cell is constructed from a cylindrical Pyrex tube (6.5 cm long, 1.2 cm diameter) with a 1 cm long cold-stem and Brewster windows (Opthos, Inc)[2]. The cell contains pure ^{87}Rb metal and no buffer gas. In order to control the number density of ^{87}Rb atoms, a double-path heating wire (California Fine Wire Stablohm 800) wrapped around the cell is used to heat the cell. Temperature of the cell is monitored at the center and near one of the windows by thermocouple sensors. The cell is housed inside a two-layer cylindrical μ-metal shield without end caps in order to shield ambient magnetic fields. A small access hole is punctured on the side of the shield to monitor a fluorescence. The entire cell assembly is placed near the output coupler.

The center frequency of the laser is tuned using a 3-plate birefringent filter near 795 nm of the D1 line. The fluorescence from the vapor is collected by a photo-multiplier tube (Hamamatsu R928) with a bandpass filter for 795 nm. By monitoring the fluorescence, the center frequency is tuned across the resonance.

[2]Other types of cell windows are also tested for a use in this intracavity experiment. Details on the design considerations for the window piece are presented in Appendix B.

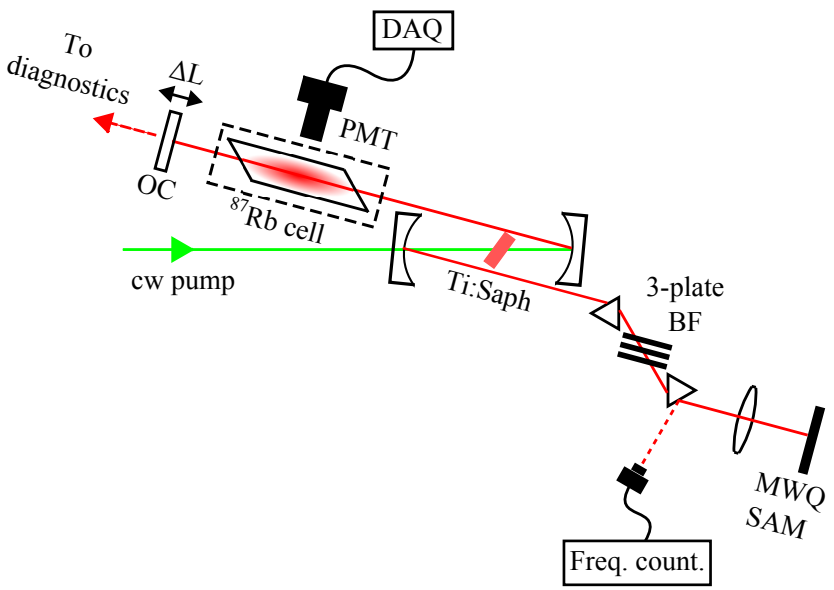

Figure 5.4: Home-built linear Ti:Sapphire laser hosting an intracavity ^{87}Rb cell. Cavity elements include a multiple quantum well saturable absorber mirror (MQW-SAM), 3-plate birefringent filter (BF), a pair of Brewster prisms, an output coupler (OC) on a translation stage and a ^{87}Rb vapor cell enclosed in a μ-metal shield (dashed box). The repetition rate is sampled from a prism reflection, using a 500 MHz photodetector and a frequency counter (FC). Fluorescence is collected by a photomultiplier tube (PMT). Both signals from FC and PMT are send to a data acquisition system.

5.3.2 Intracavity propagation

Pulse shaping

When the center frequency is detuned off atomic resonance, the laser generates a mode-locked train of $1 \sim 5$ ps pulses. When it is tuned on-resonance, significant pulse shaping is observed. The degree of pulse shaping seem to strongly depend on the pulse characteristics off resonance, including pulse energy and the bandwidth of the cavity. In the following, the pulse shaping effects are examined with different input pulse parameters.

Figure 5.5 shows auto-correlation traces of a pulse train off resonance (left) and

on-resonance (right). In off-resonant case, 4.3 ps pulses at 126.6492 MHz are generated. No significant deviation from a transform-limited pulse is present. The laser is pumped at 4.8 W pump power and generates 197 mW output power, measured immediately after the $R = 96\%$ output coupler. When the laser is tuned on resonance, a significant pulse broadening is observed as shown in the right figure. The pulse width of 54 ps is obtained, which is more than 10 fold broadening from the off-resonant case. In addition, the repetition rate is reduced by more than 4 kHz, which implies a delay of approximately 300 fs over the length of the 6.5 cm cell.

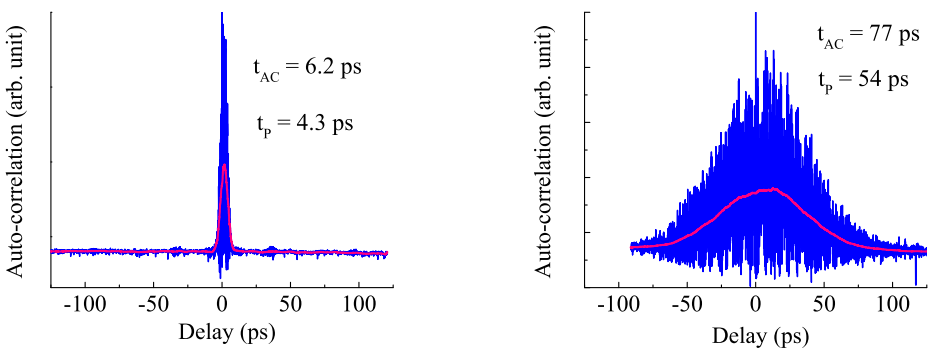

Figure 5.5: Auto-correlation of a pulse train off-resonance (left) and on-resonance (right).

To show how sensitive the coherent propagation effects are to experimental parameters, auto-correlation traces of a pulse train of the laser with different power are compared in Figure 5.6. The off-resonant pulse (left) is $\tau_p = 1.2$ ps with a near transform-limited envelope (inset), which is slightly shorter than the off-resonance pulse train shown in the previous figure. The pulse shaping effects on resonance are shown in the middle and right panels. The auto-correlation in the middle panel is obtained when the laser is pumped at 4.0 W, while the one in the right panel is obtained when pumped at 4.8 W. The on-resonance pulse shaping effect exhibits a strong modulation of the pulse envelope.

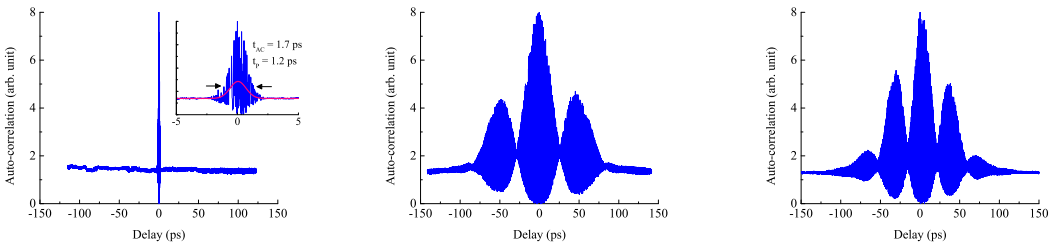

Figure 5.6: Pulse shaping effect due to coherent interaction between a picosecond pulse and ^{87}Rb vapor. Auto-correlation of a pulse train off-resonance (left) shows a near transform-limited pulse shape with 1.2 ps width (inset). Power-dependent pulse shaping occurs on-resonance when pumping at 4.0 W (middle) and 4.8 W (left).

Slow-light propagation

Coherent interaction is accompanied with slow propagation of the pulse envelope, which is caused by absorption in the front portion of the pulse, followed by coherent emission to the rear end. For example, in the long pulse limit, a 2π-pulse experiences a delay on the order of the pulse width as given by Eq. (5.44). This delay is proportional to the absorption length which is proportional to the atomic number density.

In this experiment, a change in the repetition rate is measured while the atomic number density is controlled by the cell temperature. The pulse delay is deduced from a change in the repetition rate. A relation between the change in repetition rate and a delay in the vapor is given by

$$\tau = -\frac{\Delta f_{rep}}{f_{rep}^2} \tag{5.49}$$

where f_{rep} and Δf_{rep} are repetition rate and its change, respectively. Experimental result is plotted in Figure 5.7. A linear dependence of the pulse delay on the number density is observed.

To compare with a prediction of the Maxwell-Bloch equation, a result of a nu-

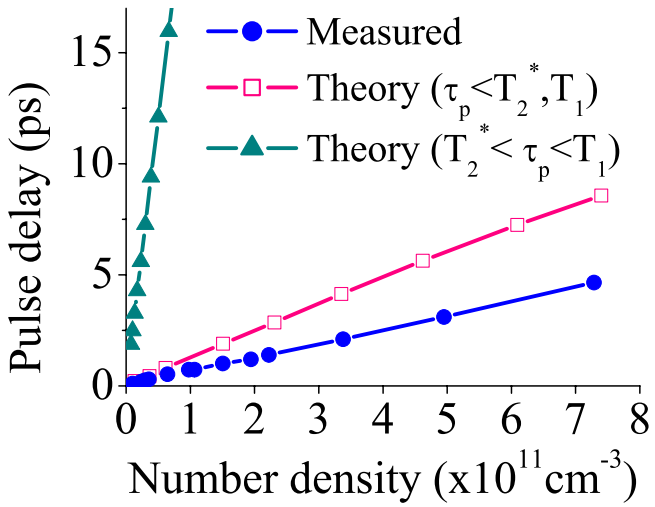

Figure 5.7: Pulse delay as a function of the number density of the ^{87}Rb vapor. Experimental results (blue-circles) are presented along with a numerical result (red-squares) obtained from the solution of Eq. (5.46) and the analytical solution (green-triangles) obtained from Eq. (5.44) for a two-level system in the limit of inhomogeneous broadening larger than the pulse spectrum, and pulse shorter than the homogeneous dephasing time.

merical integration of the Maxwell-Bloch equation is also plotted in the figure. The numerical data is obtained by simultaneously integrating Eq. (5.46) and Eq. (5.47) using the Butcher predictor-corrector method, which is known to be the most stable integrator for Schrödinger type ODEs. The integration is carried over $z = 13.0$ cm, twice the length of the vapor cell, since a pulse traverses the cell twice per round trip in the linear cavity. The area in this series of calculations is set to $\theta = 2\pi$. The pulse width is set to $\tau_s = 25$ ps. A pulse delay is measured as a delay of the peak of the output pulse with respect to the input pulse. A linear dependence of group delay on the number density observed in the experiment is reproduced.

However, there is nearly a factor of two difference in the slope of the experiment and the numerical results. One possible source of the discrepancy is the presence of the laser gain in the experiment, which is not included in the numerical analysis. As

will be discussed in the next section, the presence of a gain can cause the value of the stable area to be different from 2π. Therefore, it is possible that the observed phenomenon of slow pulse propagation cannot simply be modelled by propagation of a 2π-pulse. Another possibility is an exclusion of 4-th level of ^{87}Rb atoms in the numerical modelling. This simplification can also affect the proper definition of the area which is applicable to the present experimental conditions.

To qualitatively gauge a degree of the discrepancy, the analytical solution for a delay in Eq. (5.44) obtained for a stable 2π-pulse is plotted in the same figure. The analytical solution is obtained in the long pulse limit ($T_2^* < \tau_p < T_1$), which is applicable to a nanosecond pulse propagating in a two-level system. Arguably, there are significant differences in terms of physics between interaction of two-level atoms with nanosecond pulses and that of three-level-atoms with picosecond pulses, which give rise to a large gap between the analytical solution and both experimental and numerical results obtained for a system of picosecond pulses and a three-level system. Therefore, the simple model based on a three-level system interacting with a picosecond 2π-pulse provides at least a coarse description of the experimental observations and an insight into the coherent nature of the intracavity interaction between ^{87}Rb atoms and a resonant picosecond pulse.

Area evolution in the presence of a gain

Resonant interaction between atoms and a resonant pulse critically depends on the area θ. An ideal two-level system with very long relaxation times (T_1, $T_2 \to \infty$), and large inhomogeneous broadening ($T_2^* \ll \tau$), there exists a stable area which is found to be 2π. A 2π-pulse propagates in an absorber without attenuation or distortion. Input pulse areas other than 2π evolve towards the closest even integer of 2π. The degree of pulse shaping critically depends on the input area. For example, a 4π-pulse evolves into two 2π-pulses, a 3π pulse evolves towards a 2π pulse through

compression, and a pulse of initial area slightly over π will stretch towards a stable 2π pulse. These trends apply for media that are initially in the ground state (absorbers).

The area theorem applies as well to amplifying media, with a reversal of sign for α. Previous numerical calculations have shown that in the amplifier case, the 2π pulse is no longer a stable solution. A π pulse on resonance [64], a $\pi\sqrt{2}$ pulse off resonance and any other solutions [65] have been found numerically, but none of them has been demonstrated to be stable. What is most often observed is an evolution towards a 0π pulse [64], such that the time integral of the electric field vanishes, while the energy (and intensity) grows indefinitely.

A case of a two-level system inside an amplifying cavity has not been studied previously, and it may be considered intermediate between the absorbing and amplifying two-level system. While the same area-dependent pulse shaping takes place in the interaction with a ^{87}Rb vapor, there is the additional complexity that ^{87}Rb is a three-level system with finite relaxation times. To characterize those observed pulse shaping effects and slow propagation, it is important to identify the area of the pulses.

Determination of the area

The area can be determined from parameters measured in experiments as following. The average energy per pulse is given by

$$\langle U \rangle_{pulse} = P \times \tau_{rt} \tag{5.50}$$

where P is the average power and τ_{rt} is the repetition rate.

Energy density per pulse is then

$$W = \frac{P \times \tau_{rt}}{\sigma} \tag{5.51}$$

where σ is a beam cross-sectional area. For a Gaussian beam profile (TEM00),

$$\sigma = \frac{\pi w^2}{2} = \frac{\pi D^2}{8} \tag{5.52}$$

where w is the half-width at $1/e^2$ and D is the diameter of Gaussian beam profile measured with a beam profiler (Spiricon).

On the other hand, a time integral of intensity over the duration of the pulse also gives the energy density per pulse:

$$W = \frac{1}{2\sqrt{\mu_0/\epsilon_0}} \int |\mathcal{E}|^2 dt = \frac{|\mathcal{E}_0|^2}{2\sqrt{\mu_0/\epsilon_0}} \int \mathrm{sech}^2(t/\tau_s) dt = \frac{|\mathcal{E}_0|^2 \tau_s}{\sqrt{\mu_0/\epsilon_0}} \tag{5.53}$$

By setting Eq. (5.51) equal to Eq. (5.53),

$$\frac{P \times \tau_{rt}}{\pi(D^2/8)} = \frac{|\mathcal{E}_0|^2 \tau_s}{\sqrt{\mu_0/\epsilon_0}}$$

$$|\mathcal{E}_0| = \left[\frac{8\sqrt{\mu_0/\epsilon_0}}{\pi} \frac{P\tau_{rt}}{D^2 \tau_s} \right]^{1/2} \tag{5.54}$$

The area, as defined in Eq. (5.25) in the frequency domain, is

$$\theta = \kappa \mathcal{E}(\omega_\ell)$$

where $\mathcal{E}(\omega_\ell)$ is a spectral amplitude on resonance, which is given by

$$\mathcal{E}(\omega_\ell) = \pi \mathcal{E}_0 \tau_s \tag{5.55}$$

for a hyperbolic secant envelop with width τ_s.

Combining Eq. (5.25), Eq. (5.54) and Eq. (5.55), the area of a pulse measured in the laboratory is thus

$$\begin{aligned} \theta &= \pi \kappa \tau_s \left[\frac{8\sqrt{\mu_0/\epsilon_0}}{\pi} \frac{P\tau_{rt}}{D^2 \tau_s} \right]^{1/2} \\ &= \left(\frac{8\pi\sqrt{\mu_0/\epsilon_0}}{1.7627} \right)^{1/2} \frac{p}{\hbar} \frac{\sqrt{P\tau_{rt}\tau_p}}{D} \end{aligned} \tag{5.56}$$

where $\tau_p = 1.7627\tau_s$.

The dipole moment p of ^{87}Rb D1 line is 2.5373×10^{-29} Cm. For a three-level Λ system, the dipole moment of each transition, $|1\rangle \leftrightarrow |3\rangle$ and $|2\rangle \leftrightarrow |3\rangle$, is reduced by a half. In calculating the area Eq. (5.56), we will use $p = 1/2 \times 2.5373 \times 10^{-29}$ Cm.

Other parameters including the average power P, pulse width τ_p, pulse period τ_{rt} and beam diameter D are experimentally measured. Among these parameters, the pulse period can be measured with great accuracy using a RF counter. The rest of the parameters are always accompanied with uncertainties, among which the average power is least accurately measured due to an uncertainty in the reflectivity of the output coupler and an uncertainty in the amount of loss introduced in the cell. An uncertainty in measurement of the beam diameter also significantly affects the calculation of the area, because the area is inversely proportional to the beam diameter, as seen in Eq. 5.56. The measured experimental parameters and the calculated area using Eq. (5.56) with those parameters are summarized in Table 5.1.

	Measurement 1	Measurement 2	Measurement 3
τ_s (ps)	39	30	36
$1/\tau_{rt}$ (MHz)	127	127	121
P (W)	$1.7 \sim 2.0$	$3.7 \sim 3.9$	$1.7 \sim 1.9$
D (μm)	$390 \sim 420$	$450 \sim 560$	$670 \sim 740$
θ/π	$2.3 \sim 2.6$	$2.4 \sim 3.2$	$2.3 \sim 2.6$

Table 5.1: Measured laboratory parameters and the area calculated using Eq. (5.56). Three different data sets and corresponding area are shown.

0π-pulse component

The values of experimentally measured areas in Table 5.1 are larger than the stable area of $\theta = 2\pi$. In an auto-correlation trace of the output pulse train as shown in

Figure 5.6, the output pulses have a strong phase modulation which is dependent of the input power. Such phase modulation can be introduced by a pulse component evolving towards 0π. If that is the case, Eq. (5.56) would generate an area large than 2π. In order to examine the presence of the 0π-pulse component, it is required to measure a spectrum of the output pulse. As the area in frequency domain is defined as $\theta = \kappa\mathcal{E}(\omega_\ell)$ in Eq. (5.25), a spectrum of 0π-pulse has no component at the resonant frequency. A spectrum of the phase modulated pulse such as the one in Figure 5.6 would display a vanishing spectral component near the atomic resonance. The correct value for the area can be obtained for the spectral amplitude multiplied by κ at the resonance.

A measurement of the output spectrum can be done by employing a high resolution spectroscopy. The atomic line width is only on the order of $10^{-1} \sim 10^{0}$ GHz while a picosecond pulse spectrum spans approximately $10^{3} \sim 10^{4}$ GHz. By using a high-resolution optical spectrometer, such as a stabilized Michelson interferometer or a high-finesse Fabry-Perot interferometer, it is feasible to experimentally measure the spectral amplitude of the output pulse spectrum at the atomic resonance, which will be a future subject of the research.

5.3.3 Coherent population trapping of ^{87}Rb

Intracavity CPT

One of the motivations for the intracavity experiment is to examine whether the dark-line resonance (presented in chapter 2) can be observed in a mode-locked laser cavity under high power environment. To this end, the condition for observing the intracavity dark-line resonance is established by tuning the repetition rate to a subharmonic of the ground-state hyperfine splitting while a ^{87}Rb cell is in the cavity.

Figure 5.8 shows a fluorescence signal as a function of the repetition rate. A distinct reduction of the fluorescence is clearly visible, indicating an occurrence of dark-line resonance. By fitting a Lorentzian function to the data, the resonance repetition rate is found to be 126.569 MHz, which is very close to 54th sub-harmonic of 6.835 GHz hyperfine splitting. FWHM of the measured resonance is approximately 13 kHz, determined from the fit Lorentzian.

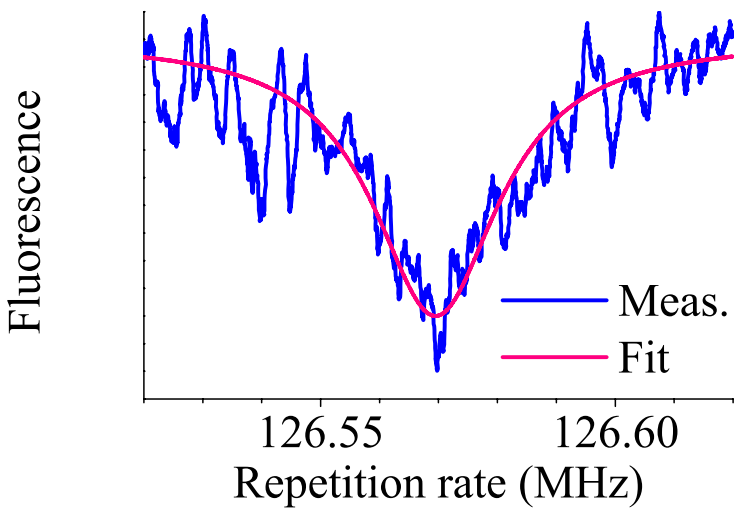

Figure 5.8: Intracavity dark-line resonance. A reduction of fluorescence occurs as the resonance repetition rate is tuned to 54th sub-harmonic of the ground-state hyperfine splitting.

It is surprising that the dark-line resonance shows that the shape, position and width of the resonance structure are very similar to those obtained in the extracavity experiment presented in Chapter 2. Only the signal contrast is somewhat smaller. In fact, the area in the extracavity experiments is very small ($\theta \ll 1$), whereas the area in this intracavity experiment is on the order of 2π. A previous numerical simulation for the dependence of the dark-line resonance on the area shows that the resonance feature diminishes with the area larger than 2.

Based on the results obtained throughout this chapter, it is possible to explain the intracavity observation of the dark-line resonance as a result of coherent interaction with a train of intense ultrashort pulses; when the area is close to 2π, the coherent rotation of the atomic polarization brings the entire population back to the ground-state while preserving the ground state coherence. Small area pulses as well as 2π pulses share in common the final state of population, which is near ground state.

5.4 Conclusion

The work presented in this chapter is to investigate the nature of resonant interaction between a picosecond mode-locked pulse train and a ^{87}Rb vapor inside a laser cavity.

When a ^{87}Rb vapor cell is placed in a mode-locked laser cavity, coherent propagation phenomena, including pulse shaping and slow group velocity, are observed. These observations are similar to the characteristics of the self-induced transparency. In an investigation of the dependence of the delay on the atomic number density, a fair agreement between the experimental data and a numerical calculation is obtained. The measurement of area, however, remains as an unsolved piece of the problem, as it is found to be 1.5 to 2 times larger than the area of the stable 2π pulse. Auto-correlation traces show a strong phase modulation, which indicates that the pulse may have evolved to have both 2π and 0π component. In order to determine the area of the generated pulses more accurately, a high resolution spectrum is required.

Despite the unsettled value of the area, a dark-line resonance is observed when the repetition rate is tuned to a sub-harmonic of the ground state hyperfine splitting of ^{87}Rb . This observation can be understood as resulting from coherent interaction with a train of intense ultrashort pulses whose area is on the order of 2π.

The results obtained in this chapter will be useful information in the future development of the IPI magnetometer.

Chapter 6

Interwoven frequency comb from a nested-cavity mode-locked laser

6.1 Overview

6.1.1 Fabry-Perot etalon

Fabry-Perot etalon (FPE) is a type of optical cavity constructed from two parallel interfaces, separated with vacuum, air or a transparent dielectric medium such as glass [66]. An incident optical field into FPE bounces back and forth multiple times between the interfaces before exiting, resulting in multiple beam interference of the output field. When the relative phase between the interfering fields is an integer multiple of 2π, a constructive interference occur. This is the case when the optical path-length $n_p d$, where n_p is the phase index of refraction of the medium filling the cavity and d is the cavity length, is an half integer multiple of the wavelength λ_0 of the field. With all the fields interfere constructively, a resonance transmission occurs with the transmission equal to unity, that is all the energy is transmitted. The width

of the resonance peak is determined by the number of interfering beams, thus depends on the reflectivity of the interfaces. The higher the reflectivity of the interfaces is, the narrower the transmission resonance becomes. Because of its simple construction and high resolution achieved by the multiple beam interference configuration, FPE has been widely used as both a high-resolution spectrometer and a high performance optical filter. Quantitative descriptions of the characteristics of FPE are given in Section 6.2.

6.1.2 Intracavity spectral shaping

Operated as an optical filter, FPE has been used as an intracavity spectral filter for continuous-wave (cw) lasers to achieve single-mode operation [60]. The single-mode operation is achieved by matching the spectral location one of the narrow transmission peaks of FPE to one of the laser cavity modes while introducing sufficiently large loss for other cavity modes to keep them from oscillating. In general, an insertion of FPE inside a laser cavity introduces a spectral modulation of the laser output. The initial motivation for the study presented in this chapter is to demonstrate a "cheap man" method to shape the pulse spectrum in order to improve the contrast of the dark-line of the repetition rate spectroscopy of ^{87}Rb , as presented in Chapter 3. When the experiments are performed, however, intriguing behaviors of the laser and of the generated frequency comb are observed, in addition to the desired improvement of the spectroscopy. Those observations have led us to further scrutinize the properties of this new type of mode-locked laser, dubbed the *nested-cavity mode-locked laser*. The general descriptions of the experiments are given in Section 6.4. A demonstration of tuning of the laser frequency is presented in Section 6.5. Observation and characterization of a formation of a high frequency pulse train are presented in Section 6.6.

6.1.3 Coupling of two frequency combs

One of the intriguing properties of the nested-cavity mode-locked laser is its spectrum which constitutes a new class of frequency comb having two characteristic mode spacings - the high repetition rate of FPE and low repetition rate of the laser cavity - dubbed the *interwoven frequency comb*. Through various experiments, it is revealed that the high and low repetition rates interact with each other through the resonance conditions of the laser cavity and FPE. Experimental observations and a semi-quantitative analysis of the cavity coupling effect are presented in Section 6.7.

6.1.4 Application of the interwoven frequency comb for precision phase interferometry

Lastly, a potential application of the nested-cavity mode-locked laser for a precision phase interferometry is described in Section 6.8. By exploiting the coupling of the high and low repetition rate, it is possible to perform a precision measurement of a change in the index of refraction of FPE. An application for a radiation dosimeter is proposed.

6.2 Fabry-Perot etalon

6.2.1 Transmission function

Let us consider a transmission of a monochromatic optical field through FPE with symmetric interface characterized by transmission coefficients $\tilde{t}_{ij}$ and reflection coefficients $\tilde{r}_{ij}$ at an interface between medium i and medium j. The incident field $\tilde{E}_{in}$ from one of the two interfaces undergoes internal multiple reflections at each

interface inside FPE before exiting from the other interface. The transmitted field $\tilde{E}_t$ is composed of all the multiple reflected components at the exit interface, and given by their sum [51];

$$\begin{aligned}\tilde{E}_t &= [\tilde{t}_{12}\tilde{t}_{21}e^{-i\delta/2} + \tilde{t}_{12}\tilde{t}_{21}e^{-i\delta/2}(\tilde{r}_{21}\tilde{r}_{21}e^{-i\delta}) + \tilde{t}_{12}\tilde{t}_{21}e^{-i\delta/2}(\tilde{r}_{21}\tilde{r}_{21}e^{-i\delta})^2 + \cdots]\tilde{E}_{in} \\ &= \tilde{t}_{12}\tilde{t}_{21}e^{-i\delta/2}\frac{1}{1-\tilde{r}_{21}^2e^{-i\delta}}\tilde{E}_{in} \\ &= \frac{(1-R)e^{-i\delta/2}}{1-Re^{-i\delta}}\tilde{E}_{in} \end{aligned} \tag{6.1}$$

where δ is the round-trip phase shift between each transmitted field component:

$$\delta(\Omega) = 2k_0 n_p d\cos\theta_{in} = 2\Omega n_p d\cos\theta_{in}/c \tag{6.2}$$

with k_0 the wave number, Ω the frequency of the field, n_p the phase index of refraction of the medium inside FPE, d the length of FPE, and θ_{in} the internal incident angle of the field. In deriving Eq. (6.1), the following properties of a symmetric interface have also been applied:

$$\tilde{t}_{12}\tilde{t}_{21} - \tilde{r}_{12}\tilde{r}_{21} = 1 \tag{6.3}$$

$$\tilde{r}_{12} = -\tilde{r}_{21}^* \tag{6.4}$$

$$\tilde{t}_{12}\tilde{t}_{21} = 1 + \tilde{r}_{12}\tilde{r}_{21} = 1 - |r_{12}|^2 = 1 - R \tag{6.5}$$

The transmission function $\tilde{\mathcal{T}}$ is therefore

$$\tilde{\mathcal{T}}(\Omega) = \frac{(1-R)e^{-i\delta/2}}{1-Re^{-i\delta}} = |\tilde{\mathcal{T}}|e^{-i\psi} \tag{6.6}$$

where ψ is the overall phase shift of the transmitted field which is found as

$$\psi = \tan^{-1}\left[\frac{1+R}{1-R}\tan(\delta/2)\right] \tag{6.7}$$

The intensity transmission function is

$$T = |\tilde{\mathcal{T}}|^2 = \frac{(1-R)^2}{1+R^2-2R\cos\delta} = \frac{1}{1+F\sin^2\delta/2} \tag{6.8}$$

where

$$F = \frac{4R}{(1-R)^2} \tag{6.9}$$

The intensity transmission function T as a function of δ for various values of R is presented in Figure 3.1 in Section 3.2.1. When the round-trip phase shift δ is an integer multiple of 2π, all the transmitted field components interfere constructively and a resonance occurs. At the resonance, the peak value of T is unity independent of R. For low reflectivity ($F \ll 1$), Eq. (6.8) can be approximated as

$$T \approx 1 - F\sin^2\delta/2 = 1 - \frac{F}{2}(1-\cos\delta) \tag{6.10}$$

which is characteristic of a fringe pattern of two-beam interference, such as Michelson interferometer. For high reflectivity close to unity, T drops quickly like a Lorentzian as δ is detuned from a multiple of 2π. The sharpness of the transmission peaks is conveniently characterized by the *finesse* $\mathcal{F}$, which is the ratio of the spacing between the transmission peaks, the *free-spectral-range* (fsr), to the full-width-at-half-maximum (FWHM) of the transmission peak. From Eq. (6.8), the transmission intensity drops to one half at $\delta_{1/2} = 2/\sqrt{F}$. Since fsr is 2π, the finesse is given by

$$\text{Finesse}: \quad \mathcal{F} = \frac{fsr}{FWHM} = \frac{\pi\sqrt{F}}{2} \tag{6.11}$$

For the use as a spectrometer or frequency filter, it is more practical to express T as a function of frequency. The resonant frequencies are determined by setting,

$$\delta = \frac{4\pi f n_p d\cos\theta_{in}}{c} = 2\pi N \tag{6.12}$$

where N is an integer, which gives

$$f_N = N\frac{c}{2nd_p\cos\theta_{in}} \tag{6.13}$$

The free-spectral-range in frequency is then

$$f_{fsr} = \frac{c}{2n_p d\cos\theta} \tag{6.14}$$

6.2.2 Pulse propagation in a Fabry-Perot

Unlike a case of continuous-wave (cw), propagation of a short pulse through FPE depends on relative duration between the pulse width and the round-trip time of FPE. When the pulse width τ_p is comparable or longer than the round trip time of FPE τ_{fp} ($\tau_p \geq \tau_{fp}$), an interference between different portions of a single pulse occurs. On the other hand, when the pulse duration is much shorter than the round trip time of FPE ($\tau_p << \tau_{fp}$), no interference occurs because any portion of the pulse does not overlap in FPE after each round trip. Difference in the pulse propagation velocity (group velocity) between those two cases is discussed in the following paragraphs.

Long pulse limit: $\tau_p \gg \tau_{fp}$

From Eq. (6.6), the transmitted field through FPE is given by

$$\tilde{E}_t(\Omega) = \tilde{\mathcal{T}}(\Omega)\tilde{E}_{in}(\Omega) = |\tilde{\mathcal{T}}(\Omega)|\tilde{\mathcal{E}}_{in}(\Omega-\omega_\ell)e^{-i\psi(\Omega)} = \tilde{\mathcal{E}}_t(\Omega-\omega_\ell)e^{-i\psi(\Omega)} \tag{6.15}$$

When the pulse spectrum is narrow compared to the width of the resonance transmission peak, the phase factor $\psi(\Omega)$ can be expanded in a power series about the carrier frequency ω_ℓ:

$$\psi(\Omega) = \psi(\omega_\ell) + \left.\frac{d\psi}{d\Omega}\right|_{\omega_\ell}(\Omega-\omega_\ell) + \frac{1}{2}\left.\frac{d^2\psi}{d\Omega^2}\right|_{\omega_\ell}(\Omega-\omega_\ell)^2 + \cdots \tag{6.16}$$

The inverse Fourier transform of Eq. (6.15) with Eq. (6.16) leads to the transmitted field in the time domain:

$$\begin{aligned}
\tilde{E}_t(t) &\approx \int_{-\infty}^{\infty} \tilde{\mathcal{E}}_t(\Omega-\omega_\ell)e^{-i[\psi(\omega_\ell)+\left.\frac{d\psi}{d\Omega}\right|_{\omega_\ell}(\Omega-\omega_\ell)]}e^{i\Omega t}d\Omega \\
&= e^{i\left(\frac{d\psi}{d\Omega}-\frac{\psi}{\omega_\ell}\right)\omega_\ell}\int_{-\infty}^{\infty}\tilde{\mathcal{E}}_t(\Omega-\omega_\ell)e^{\Omega(t-\frac{d\psi}{d\Omega})}d\Omega \\
&= e^{i\left(t-\frac{\psi}{\omega_\ell}\right)\omega_\ell}\int_{-\infty}^{\infty}\tilde{\mathcal{E}}_t(\Omega')e^{\Omega'(t-\frac{d\psi}{d\Omega})}d\Omega' \\
&= e^{i\left(t-\frac{\psi}{\omega_\ell}\right)\omega_\ell}\tilde{\mathcal{E}}(t-d\psi/d\Omega)
\end{aligned} \tag{6.17}$$

where a new variable $\Omega' = \Omega - \omega_\ell$ has been made. From Eq. (6.17), the phase and group delay can be defined as

$$\text{Phase delay}: \quad \tau_{ph} = \frac{\psi}{\omega_\ell} \tag{6.18}$$

$$\text{Group delay}: \quad \tau_{gr} = \frac{d\psi}{d\Omega} \approx \frac{\partial\psi}{\partial\Omega} + \frac{\partial\psi}{\partial n}\frac{\partial n}{\partial\Omega} \tag{6.19}$$

In general, a frequency-dependent index of refraction (dispersion) results in the difference between the phase and group delay.

The near-resonance response of FPE can be found by expanding Eq. (6.6) about $\delta = 2\pi$. Keeping the lowest order in δ, it is left with

$$\tilde{\mathcal{T}}(\delta) = \frac{(1-R)e^{-i\delta/2}}{1-Re^{-i\delta}} \approx \frac{e^{-i\delta/2}}{1+i\frac{R}{1-R}\delta} \approx e^{-i\delta/2}\left[1 - i\frac{R}{1-R}\delta\right] \tag{6.20}$$

The phase shift in single passage is

$$\psi = -\frac{\delta}{2}\left[1 + \frac{2R}{1-R}\right] \tag{6.21}$$

Using Eq. (6.18) and Eq. (6.19), the single-passage phase and group delay occurred in near-resonance transmission are given by;

$$\text{Phase delay}: \quad \tau_{ph} = \frac{\psi}{\omega_\ell} = -\frac{n_p d\cos\theta_{in}}{c}\left[1 + \frac{2R}{1-R}\right] \tag{6.22}$$

$$\begin{aligned}\text{Group delay}: \quad \tau_{gr} = \frac{d\psi}{d\Omega} &= -\frac{1}{2}\left[1 + \frac{2R}{1-R}\right]\frac{d\psi}{d\Omega} \\ &\approx -\frac{1}{2}\left[1 + \frac{2R}{1-R}\right]\left(\frac{\partial\delta}{\partial\Omega} + \frac{\partial n}{\partial\Omega}\right) \\ &= \frac{n_p d\cos\theta_{in}}{c}\left[1 + \frac{2R}{1-R}\right]\left(1 + \omega_\ell \left.\frac{dn}{d\Omega}\right|_{\omega_\ell}\right)\end{aligned} \tag{6.23}$$

The last two expression are only valid *near a single resonance peak* of FPE, implying therefore that the spectrum of the light incident on that FPE is narrower than the transmission linewidth of FPE.

Ultrashort pulse limit: $\tau_p \ll \tau_{fp}$

Most mode-locked lasers generate femtosecond to picosecond pulses whose spatial extension is no more than a few hundred microns which is considerably short compared to commonly used FPEs of the order of a few millimeters or longer. In this case, since the input pulse spectrum of an ultrashort pulse is much broader than the free spectral range of FPE, the transmitted spectrum consists of a comb of transmission peaks with their width determined by the reflectivity of the interfaces. In the time domain, the transmitted field consists of a train of multiply reflected pulses with their amplitudes decaying with the number of round trips.

To find a delay between transmitted pulses, let us look at the path those pulses take in FPE. Referring to Figure 6.1, the delay, τ_{fp}, is a time difference between path BCD and path BE. The length of those paths are

$$\begin{aligned} BCD &= \frac{2d}{\cos\theta_{in}} \\ BD &= 2d\tan\theta_{in} \\ BE &= 2d\tan\theta_{in}\sin\theta_{out} = \frac{2n_p d\sin^2\theta_{in}}{\cos\theta_{in}} \end{aligned}$$

The delay between the transmitted pulses is then given by

$$\begin{aligned} \tau_{fp} &= \frac{n_g(BCD) - (BE)}{c} \\ &= \frac{2d}{c\cos\theta_{in}}\left(n_g - n_p\sin^2\theta_{in}\right) \\ &= \frac{2n_p d\cos\theta_{in}}{c} + \frac{2d(n_g - n_p)}{c\cos\theta_{in}} \end{aligned} \tag{6.24}$$

The second term of the last equation is a correction to the phase delay due to the difference between group and phase velocity.

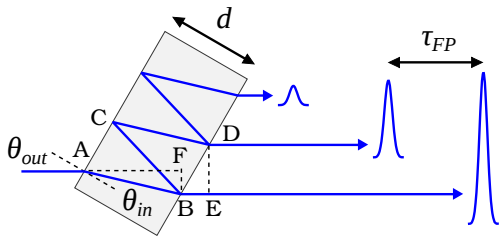

Figure 6.1: A schematic of pulse propagation in FPE when the pulse duration is much shorter than the FPE round trip time. In the ultrashort pulse limit, no interference occurs, and the delay between the transmitted pulses is given by Eq. (6.24)

Transmission of pulse train: the machine gun out of the Fabry-Perot

Consider a propagation of a single pulse entering FPE, with a field given by $E_0(t) = \tilde{\mathcal{E}}_0(t)\exp(i\omega t)$. The sequence of N pulses is a total field $E(t)$:

$$E(t) = e^{i\omega t}T\sum_{p=0}^{N} R^p \tilde{\mathcal{E}}_0(t - p\tau_{fp}) \tag{6.25}$$

The Fourier transform of that expression is:

$$\begin{aligned} E(\Omega) &= T\tilde{\mathcal{E}}_0(\Omega-\omega)T\left[1 + Re^{i\Omega\tau_{fp}} + \ldots R^N e^{Ni\Omega\tau_{fp}}\right] \\ &= T\tilde{\mathcal{E}}_0(\Omega-\omega)\frac{1 - R^{(N+1)}e^{(N+1)i\Omega\tau_{fp}}}{1 - Re^{i\Omega\tau_{fp}}} \end{aligned} \tag{6.26}$$

Notice that the dependence of the phase factor in the numerator on the number of pulses N. For $N \to \infty$:

$$E(\Omega) = \frac{T\tilde{\mathcal{E}}_0(\Omega-\omega)}{1 - Re^{i\Omega\tau_{fp}}} \tag{6.27}$$

Expression in Eq. (6.25) is in the time domain, while Eq. (6.26) is the corresponding expression in the frequency domain.

6.3 Intracavity Fabry-Perot etalon

6.3.1 General properties

Evolution of transmission function over many passages

When a transmitted field is recycled and injected back to FPE, for example by constructing a cavity around FPE, the field transmission function after p-th passage is given by p-th power of the single-pass transmission function in Eq. (6.6):

$$\tilde{\mathcal{T}}_p(\Omega) = \left[\frac{(1-R)e^{-i\delta/2}}{1-Re^{-i\delta}}\right]^p \tag{6.28}$$

Figure 6.2 shows an evolution of the transmission function over 50 passages for $R = 0.034$. After the first passage, the transmitted function is weakly modulated sinusoidally, as expected for small R in Eq. (6.10). As the number of passages p approaches 50, the modulation depth increases to 100 % and each transmission peak becomes more like a Gaussian. As $p \to \infty$, the transmission function becomes a comb of Delta functions (Dirac comb). The same phenomenon occurs for large R, in which the initial Lorentzian line-shape becomes a Gaussian-like line-shape as the number of passages increase. In time domain, it implies that the envelope function of a train of transmitted pulses evolves from single-sided exponential to Gaussian over many passages through FPE. This is confirmed in the experiment presented below.

Effective finesse

Due to the feedback and amplification of the pulse energy by means of a laser cavity enclosing FPE, the apparent finesse of the uncoated glass FPE is significantly increased. As seen in Figure 6.2, the finesse of the transmission peaks increases with the number of passages. The amplification by the laser gain in the feedback cavity

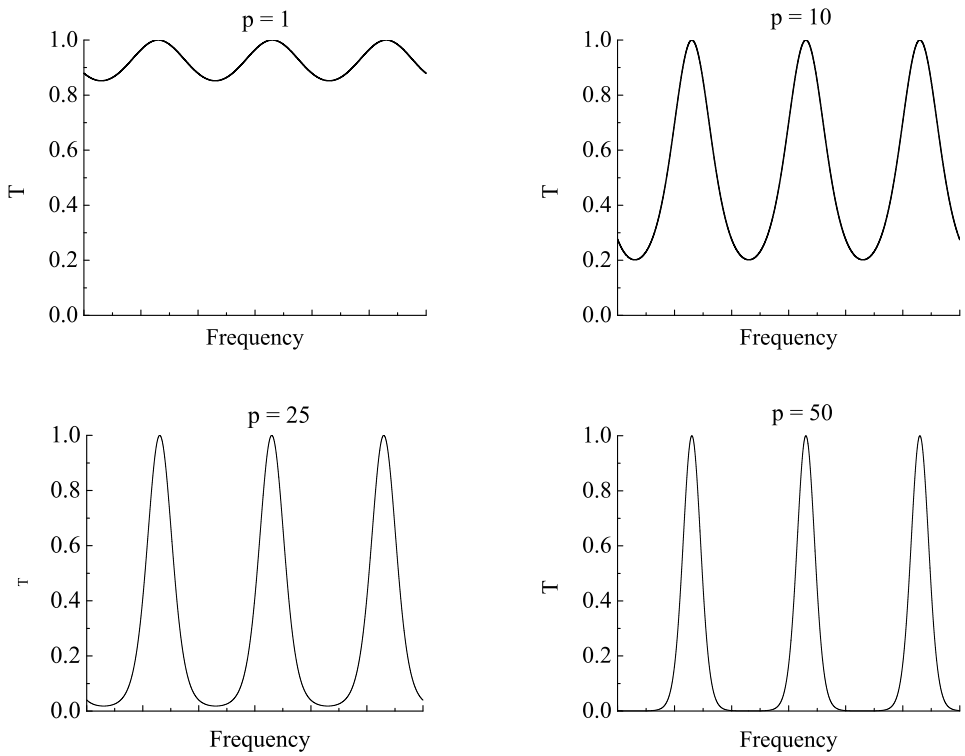

Figure 6.2: Evolution of the transmission function Eq. (6.28) over 50 passages. The surface reflection is $R = 0.034$ for an uncoated fused-silica FPE.

compensates for the loss caused in the transmission through FPE, and therefore contributes to further increasing the finesse. The upper limit is determined by a finite energy stored in the gain medium. In experiments, as many as 16 pulses has been observed in a steady-state cavity.

Interference of ultrashort pulses

Unlike the single-passage case ($p = 1$), interference of ultrashort pulses ($\tau_p \ll \tau_{fp}$) occurs in the multi-passage transmission through a thick FPE, because the pulse period of the input pulse train is guaranteed to match the round-trip time of FPE. This is an important aspect of the intracavity Fabry-Perot etalon, and gives rise to

a double-resonance condition for the nested cavity system, as described below.

Resonance modes

Laser oscillation of the nest-cavity laser occurs when the resonance condition of both cavities are satisfied simultaneously. This simultaneous resonance condition couples the modes of the two resonant cavities. However, since the number of pulses interfering through FPE transmission is finite, the resonance width of the FP transmission is rather broad, as shown above in Figure 6.2. This broad or "soft" resonance condition allows the resonance modes of one cavity to follow those of the other. In Section 6.7, a coupling between the high frequency (HF) modes of FPE and the low frequency (LF) modes of the laser repetition rate is described in more details.

Modified group velocities

Another intriguing property of the intracavity FPE is that the group velocities are no longer determined by the dielectric constant of the intracavity elements, but are dominated by distribution of the pulse energy in a pulse train. During transmission though FPE, the energy of a pulse is transferred to following pulses. Looking over a pulse train, there is an overall recession of the energy front, which results in a slow propagation the "center of gravity" of the pulse train in the laser cavity. On the other hand, the saturation of the laser gain has an opposite effect. Pulses in the front edge of the pulse train receive a gain proportional to their intensities while depleting the gain medium. Within a time scale of the pulse train ($\sim$ ns), the gain medium does not recover completely, thus leaves less gain for the pulses in the latter part of the pulse train. As a result, the center of gravity of the pulse train is accelerated. These effects are *quantitatively* verified by the numerical simulation of evolution of the high frequency pulse train, which is presented in Section 6.6.

6.3.2 FPE inside a *ring* laser cavity

An actual laser contains a gain medium, so the combined effect of the intracavity FPE and gain will be analyzed here. In particular, their effects on the transmission phase and resonance frequencies will be investigate. Consider transmission of a pulse train through FPE placed inside a ring laser cavity. There are N pulses in the train. The difference from a linear cavity is that FPE is traversed once in each round-trip in the laser cavity. Let $\tilde{\mathcal{E}}_n$ be the field amplitude just before FPE, at the round-trip n. The first value of $\tilde{\mathcal{E}}_n$ is the single pulse $\tilde{\mathcal{E}}_0$. The n-th value in frequency is given by Eq. (6.26):

$$\tilde{\mathcal{E}}_n(\Omega) = \tilde{\mathcal{E}}_{n-1}(\Omega)\frac{1 - R^{(N+1)}e^{(N+1)i\Omega\tau_{fp}}}{1 - Re^{i\Omega\tau_{fp}}}T \tag{6.29}$$

where $\tilde{\mathcal{E}}_{n-1}$ represents the pulse train at the $n-1$ cycle of the ring cavity, and $A_N(\Omega)$ is the transmission function of FPE:

$$A_N(\Omega) = \frac{1 - R^{(N+1)}e^{(N+1)i\Omega\tau_{fp}}}{1 - Re^{i\Omega\tau_{fp}}}T \tag{6.30}$$

Notice that the phase up on transmission depends the number of pulses N. The inverse Fourier transform of Eq. (6.30) is given by

$$A_N(t) = \int_{-\infty}^{\infty} \frac{1 - R^{(N+1)}e^{(N+1)i\Omega\tau_{fp}}}{1 - Re^{i\Omega\tau_{fp}}}e^{i\Omega t}d\Omega. \tag{6.31}$$

Remember that N is a fixed number, while n is the running index for the round-trips in the ring cavity. The inverse Fourier transform of Eq. (6.29) is the convolution:

$$\tilde{\mathcal{E}}_n(t) = \tilde{\mathcal{E}}_{n-1}(t) * A_N(t) \tag{6.32}$$

During a round-trip in a ring cavity, the pulse train goes once through the sequence [gain $\rightarrow$ cavity propagation $\exp(-ikL)$ $\rightarrow$ Fabry-Perot]. L is the length (perimeter) of the ring cavity excluding FPE. For simplicity of the analysis, the gain

is considered to be a constant in time. In the time domain, the infinite train $\tilde{\mathcal{E}}(t)$ is the sum:

$$\begin{aligned}\tilde{\mathcal{E}}(t) &= \Big\{\tilde{\mathcal{E}}_0(t) * A_N(t) \\ &+ \Big[\tilde{\mathcal{E}}_1(t-\tau_{rt}) * A_N(t-\tau_{rt})\Big] \times g \times e^{-ikL} \\ &+ \Big[\tilde{\mathcal{E}}_2(t-\tau_{rt}) * A_N(t-2\tau_{rt})\Big] \times g^2 \times e^{-2ikL} \end{aligned} \tag{6.33}$$

The Fourier transform of the expression in Eq. (6.33) is:

$$\begin{aligned}\tilde{\mathcal{E}}(\Omega) &= \Big\{\tilde{\mathcal{E}}_0(\Omega) A_N(\Omega) \\ &+ \Big[\tilde{\mathcal{E}}_1(\Omega) A_N(\Omega)\Big] \times g \times e^{i\Omega\tau_{rt}-ikL} \\ &+ \Big[\tilde{\mathcal{E}}_2(\Omega) A_N(\Omega)\Big] \times g^2 \times e^{2i\Omega\tau_{trt}-2ikL}\Big\} \\ &= \left\{\sum_{n=1}^{n=\infty} \left[A_N(\Omega) g e^{i\Omega\tau_{rt}-ikL}\right]^n\right\} \tilde{\mathcal{E}}_0 A_N(\Omega) \end{aligned} \tag{6.34}$$

where the Ω dependence of k is neglected, which is a reasonable assumption since the modes of the mode-locked laser are equally spaced. The geometric sum can be made:

$$\tilde{\mathcal{E}}(\Omega) = \frac{\tilde{\mathcal{E}}_0 A_N(\Omega)}{1 - [A_N(\Omega) g e^{i\Omega\tau_{rt}-ikL}]}. \tag{6.35}$$

where

$$A_N(\Omega) = \frac{1 - R^{(N+1)} e^{(N+1)i\Omega\tau_{fp}}}{1 - R e^{i\Omega\tau_{fp}}} T$$

This is a qualitative expression of the Fabry-Perot transmission of the laser cavity with gain and FPE for finite number of pules. It can be observed by inspecting the functional form of Eq. (6.35) and $A_N(\Omega)$ that the transmission phase depends on N, τ_{fp}, τ_{rt} and L. In order to determine a more accurate transmission function, a nonlinear time-dependent gain $g(t, I)$, where I is the pulse intensity, needs to

be determined. In that case, the finite life-time of the gain keeps the Fabry-Perot transmission peaks from collapsing to a narrow resonance, and there will also be an additional phase due to the time-dependence of the gain.

6.4 General experimental setup

6.4.1 Nested-cavity mode-locked laser

The nested-cavity mode-locked laser is constructed from a linear titanium-sapphire mode-locked laser and an intracavity glass FPE, as shown in Figure 3.3 in Section 3.3.1. Mode-locking is assisted by a multiple quantum well saturable absorber integrated on a Bragg reflecting mirror (MQW-SAM), placed at one end of the cavity. A pair of intracavity prisms is used for dispersion control and for frequency tuning. A birefringent filter placed between the prisms serves both as a frequency tuner and as a bandpass filter which limits the spectral width to have picosecond pulses for an application in ^{87}Rb spectroscopy. The output coupler is mounted on a translation stage with a motorized micrometer to allow cavity length scanning over a range of a few tens of MHz of the repetition rate. A typical output of the laser consists of a train of picosecond pulses with repetition rate of $120 \sim 150$ MHz. The Laser frequency is tuned near 795 nm, which corresponds to the D1 line of ^{87}Rb .

FPE is mounted on a standard mirror mount (Newport U100). The lever arm of the mirror mount (a distance between the tip of an alignment screw and the pivot) is 38.1 mm. The alignment screw for vertical angle adjustment is replaced with a motorized micrometer which allows for precision control of the tilt angle θ using LabVIEW. The mounted FPE is placed near the output coupler. Its exact position is not critical since it is tilted so slightly (< 1 mrad) with respect to the beam axis in order to prevent a formation of cavities with other intracavity elements. There

are several different types of FPE used throughout the experiments presented in this chapter, including UV graded fused-silica and calcium fluoride (CaF_2) with various thickness ranging from 6.5 mm to 15 mm.

6.4.2 Alignment of laser with an intracavity FPE

Alignment of the nested-cavity mode-locked laser requires special care. Since the tilt angle of FPE with respect to the beam axis is a critical parameter in almost all the experiments in this chapter, an accurate and repeatable method to set a reference angle must be established. For the best result, the normal incident ($\theta = 0$) is chosen as the reference. The normal incident ($\theta = 0$) can be found by searching for an angle where the threshold pump power is minimum. The value of the lowest threshold power is often less than that of a bare cavity (without an intracavity FPE). This is the case when the surfaces of the end mirrors and the FPE are aligned parallel and form multiple coupled resonant cavities (Fabry-Perot effect) where the total cavity loss is minimized. Mode-locking will not start, however, unless the couplings between various surfaces are removed. In order to break the cavity couplings, FPE is tilted slightly from the normal ($\theta_{in} \geq 1$ mrad). For this reason, data points at $\theta_{in} < 1$ mrad are missing in all the experimental data.

6.4.3 Monitoring the optical frequency

Two detection schemes are employed to monitor the optical frequency of the laser output. One of them is an optical spectrometer (Ocean Optics 2000). The spectrometer has a resolution of $\Delta\lambda = 0.5$ nm, or in terms of frequency $\Delta f \approx 240$ GHz. Thus, it is only used for coarse tuning of the laser frequency.

For better resolution, a fluorescence spectroscopy of ^{87}Rb is employed. ^{87}Rb has

an optical resonances at 795 nm (D1 line) and 780 nm (D2 line) with a Doppler broadened linewidth of approximately 500 MHz. A fluorescence signal from the D1 line is monitored using a photomultiplier tube (PMT, Hamamatsu R928) with an interference filter for 795 nm.

6.4.4 Monitoring the repetition rate and the frequency of FPE

The pulse train is sampled by two detectors with different bandwidth. The first is a 500 MHz silicon photodetector (Thorlab DET210) which is connected to a 500 MHz frequency counter (HP 5335A). It is employed to measure the laser repetition rate which is on the order of 100 MHz. The second is a 25 GHz high-speed InGaAs photodetector (New Focus 1437) which is connected to either a 13 GHz RF spectrum analyzer (HP 8562E) or a 8 GHz digital oscilloscope (Tektronix DPO 70804), depending on the domain of measurement, and is employed to monitor fast temporal structures on the order of $\sim$ 10 GHz of a pulse train generated from the nested-cavity mode-locked laser.

6.5 Tuning the laser frequency with intracavity FPE

6.5.1 Resonance transmission due to multiple pulse interference

As discussed in Section 6.2, there are two cases when an interference of ultrashort pulses occur in FPE. The first case is when the pulse width is comparable or longer

than the round-trip time of FPE such that temporal overlap between different portions of the pulse occurs after each round-trip. This is certainly not the case for picosecond pulses propagating in a centimeter thick FPE ($\tau_{rt} \sim 10^2$ ps). The second case is when the round-trip time matches an integer multiple of the inter-pulse period. In this case, the multiply reflected pulses interfere with each other after every round trip. Pulse propagation in the nested-cavity mode-locked laser fits to this case, since the intracavity FPE generates a train of pulses whose inter-pulse period is equal to the round-trip time of the pulses in FPE.

When interference is present, there is resonance transmission as given by the transmission function Eq. (6.6). The maximum transmission ($T = 1$) occurs for frequencies for which the round-trip phase satisfies the resonance condition;

$$\delta = -2k_0 n_p d \cos\theta_{in} = 2N\pi \tag{6.36}$$

A laser with an inhomogeneously broadened gain, such as ti:sapphire, preferentially oscillates at frequencies for which the net gain (minus loss) per round-trip is maximum, while suppressing other modes that are competing for the gain within the homogeneous linewidth. Therefore, the resonant modes of the nested-cavity mode-locked laser is expected to satisfy the condition given in Eq. (6.36). Then, it follows that the resonant frequencies (and wavelength) are give by

$$f_{res} = \frac{cN}{n_p d \cos\theta_{in}} \tag{6.37}$$

$$\lambda_{res} = \frac{n_p d \cos\theta_{in}}{N} \tag{6.38}$$

which imply that the frequency of the laser can be tuned with the angle of the intracavity FPE.

6.5.2 Fluorescence spectroscopy of ^{87}Rb

The prediction of the angular dependence of the laser frequency (wavelength) in Eq. (6.37) (and Eq. (6.38)) is examined by fluorescence spectroscopy of a ^{87}Rb vapor. The D1 line of ^{87}Rb consists of four transitions between two ground state hyperfine states, separated by 6.8 GHz, and two excited state hyperfine states, separated by 814 MHz (referred to Figure 2.1 in Section 2.2 for the energy diagram of ^{87}Rb). At room temperature, those transitions are inhomogeneously broadened due to Dopper effect, making only the ground state hyperfine manifold fully resolved. As a result, a spectrograph of the D1 line shows two resonant peaks separated at 6.8 GHz, each corresponding to transitions between the ground state and excited state hyperfine states: $F = 1 \rightarrow F' = 1, 2$ and $F = 2 \rightarrow F' = 1, 2$. Depending on the resolution of spectroscopic apparatus being used, the excited state hyperfine structure may or many not be visible. The relative hyperfine transition strength factors for the D1 line of ^{87}Rb are given in Table 6.1.

D_1 ($5^2S_{1/2} \rightarrow 5^2P_{1/2}$)	S_{22}	1/2	S_{12}	5/6
	S_{21}	1/2	S_{11}	1/6

Table 6.1: Relative hyperfine transition strength factors for ^{87}Rb D_1 line (from Steck).

The nested-cavity mode-locked laser with a 15.12 mm fused-silica intracavity FPE generates a frequency comb with 6.8 GHz modulation with nearly 100% depth. Since the modulation period of the comb matches to the ground state hyperfine splitting, both transitions from ground state are excited when the laser frequency is tuned on-resonance. On the other hand, if the laser is tuned off-resonance, neither transitions are excited. Consequently, when the frequency is scanned across the atomic resonance, only one resonance peak will appear. The next resonance peak appears when the frequency is tuned over one free-spectral-range ($f_{fsr} \approx 6.8$ GHz). As will be described below, the frequency tunability of the nested-cavity mode-locked

laser is demonstrated based on this property. Notice that a standard frequency comb does not have either resolution or frequency tunability to perform such spectroscopy.

Figure 6.3 shows a measured fluorescence signal from the D1 line as a function of the internal angle θ_{in} of the intracavity FPE. The fluorescence signal increases when the laser spectrum has maximum overlap with the D1 line, which occurs when $\lambda_\ell = 795$ nm, where λ_ℓ is laser wavelength. There are also two smaller peaks with different strength inside each fluorescence peak. Figure 6.4 is a zoom of a single fluorescence peak (R1 in Figure 6.3). The internal FPE angles at all the fluorescence peaks are summarized in Table 6.2.

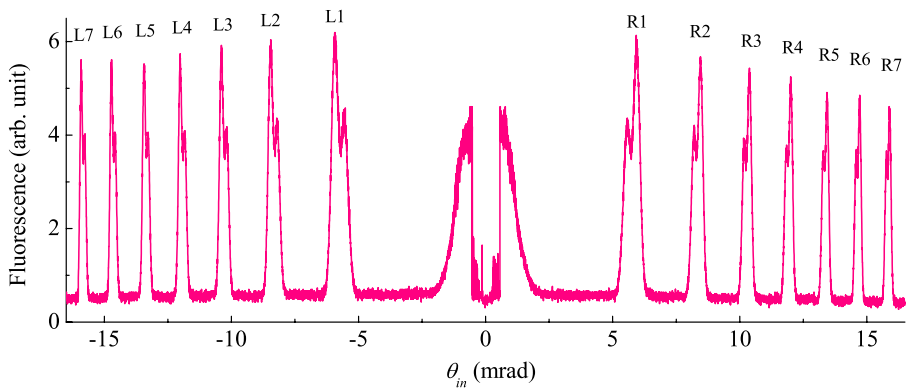

Figure 6.3: D1 fluorescence from a ^{87}Rb vapor as a function of FPE internal angle. The number and letter on the label on each fluorescence peak indicate respectively the order and the side of the plot from the origin ($\theta_{in} = 0$) they show up: "L" for left and "R" for right. Their values are summarized in Table 6.2.

To examine whether the laser wavelength follows the resonance condition of FPE, the round-trip phase shift is calculated using Eq. (6.36). The fluorescence peaks occur when δ is a multiple of 2π. Using a listed value of the resonant wavelength of the D1 line ($\lambda_{D1} = 794.978851$ nm [5]), the number of wavelength N fitted inside FPE

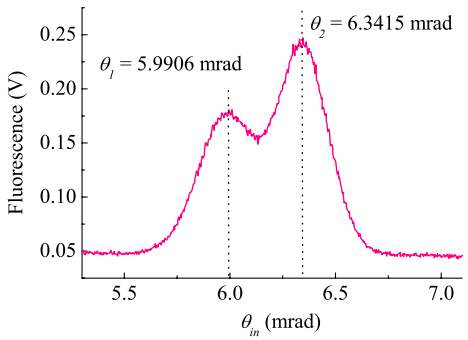

Figure 6.4: Fluorescence profile of a single peak. Laser power is attenuated to suppress power broadening of the transition. The average power is 7 mW.

Peak	L tall	L short	R tall	R short	N_i
1	-5.93006	-5.55357	5.94632	5.57236	55277
2	-8.45868	-8.2003	8.45542	8.20337	55276
3	-10.3954	-10.18471	10.38255	10.1728	55275
4	-12.01819	-11.83404	12.01145	11.83707	55274
5	-13.43735	-13.27599	13.43675	13.28332	55273
6	-14.72229	-14.57682	14.71896	14.5771	55272
7	-15.90748	-15.76924	15.898	15.7686	55271

Table 6.2: Measured values of θ_{in} at the location of spikes in each fluorescence peak in Figure 6.3. "Peak" corresponds to the numbers to label the peaks in the figure. "L" and "R" indicates the the negative angles and positive angles, respectively. "tall" and "short" indicate the relative height of the spikes within the peak. "N_i" is an integer corresponding to the number of wavelength fitted inside the $d = 15.119$ mm fused-silica FP, as calculated in Eq. (6.39). Unit of the angles is mrad.

is calculated for each fluorescence peak. For $d = 15.119$ mm and $n = 1.4534$ at λ_{D1},

$$N_i = \mathrm{mod}(\delta/2\pi) = 2n_p d\cos\theta_{in}/\lambda \tag{6.39}$$

Using the values of θ_{in} and N_i, the differences of the round-trip phase shift between adjacent fluorescence peaks are calculated as

$$\Delta\delta = \delta_{i+1} - \delta_i = 2k_0 n_p d(\cos\theta_{in}^{i+1} - \cos\theta_{in}^{i}) \tag{6.40}$$

Table 6.3 summarizes the difference in the round-trip phase shift $\Delta\delta$ between adjacent tall peaks and adjacent short peaks shown on the left side of Figure 6.3. Similarly, Table 6.4 summarizes $\Delta\delta$ for adjacent peaks on the right side. The values are given in the unit of 2π. The percent errors are calculated as

$$\% \text{ error} = \frac{(\text{measured } \Delta\delta) - 2\pi}{2\pi} \tag{6.41}$$

The result shows that the average percent error is below 1 %, indicating an excellent agreement of the behavior of the laser wavlength with Eq. (6.38).

$\Delta\delta$	L tall	% error	L short	% error
$\delta_2 - \delta_1$	-1.0056	-0.56	-1.006	-0.61
$\delta_3 - \delta_2$	-1.0092	-0.92	-1.0084	-0.84
$\delta_4 - \delta_3$	-1.0053	-0.53	-1.0037	-0.37
$\delta_5 - \delta_4$	-0.9985	0.16	-1.0007	-0.07
$\delta_6 - \delta_5$	-1.0000	0.00	-1.0014	-0.14
$\delta_7 - \delta_6$	-1.0033	-0.33	-1.0001	0.00

Table 6.3: Phase difference between adjacent fluorescence peaks on the left ($\theta < 0$) in Figure 6.3, calculated using Eq. (6.40) and the values in Table 6.2. The phase differences are calculated separately between the tall spikes and the short spikes. Other parameters used in the calculations include $k_0 = 2\pi/794.978851$ nm^{-1}, $n_p = 1.4534$ and $d = 15.119$ mm. Unit of $\Delta\delta$ is 2π.

$\Delta\delta$	R short	% error	R tall	% error
$\delta_2 - \delta_1$	-0.9987	0.13	-1.0017	-0.17
$\delta_3 - \delta_2$	-1.0034	-0.34	-1.0003	-0.03
$\delta_4 - \delta_3$	-1.0082	-0.82	-1.0124	-1.24
$\delta_5 - \delta_4$	-1.0025	-0.25	-1.0041	-0.41
$\delta_6 - \delta_5$	-0.9978	0.22	-0.9962	0.38
$\delta_7 - \delta_6$	-0.9977	0.23	-0.9993	0.07

Table 6.4: Phase difference between adjacent fluorescence peaks on the right ($\theta > 0$) in Figure 6.3.

Excited state hyperfine splitting

In order to examine the sub-peak structure in the fluorescence peaks, the frequency differences between the sub-peaks are calculated as

$$\Delta f_{spike} = \frac{cN}{2nd}\left(\frac{1}{\cos\theta_{\text{tall}}} - \frac{1}{\cos\theta_{\text{short}}}\right) \tag{6.42}$$

The results are summarised in Table 6.5. Comparing with the excited state hyperfine splitting of 814.52 MHz, the measured values match quite well. However, there is a relatively large discrepancy. The primary source of error is associated with the instrumental instability. For example, the measurement of fluorescence as a function of FPE angle as shown in Figure 6.3 takes over minutes. Over the course of the measurement, the center frequency drifts due to fluctuations of the cavity alignment, which in turn affects the relative connection between the FPE angle and the laser frequency.

Peak	L	% error	R	% error
1	815.16	0.1	812.15	-0.3
2	811.56	-0.4	791.67	-2.8
3	817.54	0.4	812.92	-0.2
4	828.18	1.7	784.12	-3.7
5	812.74	-0.2	773.00	-5.1
6	803.64	-1.3	783.62	-3.8
7	825.69	1.4	772.64	-5.1
Mean	816.36		790.02	
Stdv.	8.44		6.80	

Table 6.5: Frequency difference Δf_{spike} between the spikes in each fluorescence peak in Figure 6.3, calculated using Eq. (6.42). The % error is calculated based on the value of the excited state hyperfine splitting of 814.52 MHz. Unit is MHz.

6.6 High frequency pulse train formation

6.6.1 Temporal profile

A typical temporal profile of a standard mode-locked pulse train and of the nested-cavity mode-locked laser with a 15 mm fused-silica FPE are shown in Figure 6.5. In the standard mode-locked laser, a continuous mode-locked pulse train is generated. The pulse period is determined by the cavity round trip time of the pulses in the laser cavity. In the nested-cavity mode-locked laser, on the other hand, a Bell-shape "pulse bunch" is formed and repeated at the round trip time. The temporal extension of this high frequency pulse train is approximately 1.5 ns wide (FWHM). There are at least 14 pulses housed in a single bunch. The appearance of the pulse bunches resembles an interferometric auto-correlation of a train of femtosecond pulses. Although an analogy to the femtosecond pulse dynamics is found to be useful, what may appear as an optical oscillation in Figure 6.5 is actually the partially resolved intensity profile of individual pulses. From an auto-correlation shown in Figure 3.5 in Section 3.4, the pulse width and inter-pulse period are found to be 2 ps and 148 ps, respectively. The inter-pulse period matches approximately the group round-trip time of the 15.12 mm fused-silica, $\tau_{FP} = 2n_g d/c$ with $n_g \approx 1.48$.

6.6.2 Group velocities study

The classical textbook description of group velocity applies to transparent systems that can be fully described by their transfer function in the frequency domain [58]. As a pulse traverses an optical system characterized by a complex transfer function $\tilde{T}(\Omega) = T(\Omega)\exp(\psi(\Omega)$, it can be shown that the center of gravity of the pulse suffers a group delay τ_d given by:

$$\tau_d = \frac{d^2\psi}{d\Omega^2}. \tag{6.43}$$

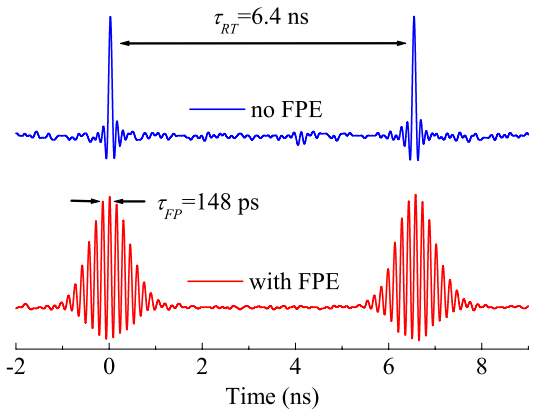

Figure 6.5: Temporal profile of an output of the nested-cavity mode-locked laser (bottom), in comparison to a pulse train from a standard mode-locked laser with the same cavity length (top). Both measurements are acquired using a 25 GHz photodetector and a 8 GHz oscilloscope.

Such a simple equation does not apply to systems with time dependent gain or absorption, however. A typical example is that of a pulse traveling in a medium with saturable gain. The decreasing gain from the leading edge of the pulse to the trailing edge results in a pulse velocity exceeding the speed of light [58]. In the case of the laser with the intracavity Fabry-Perot, the group velocities are dominated by the energy transfer from one pulse to the next as well as the time dependent gain (saturable gain), as discussed in Section 6.3.1.

The inclination angle of FPE has also an impact of the group velocity. Successive passages shift the pulse in space as well as in time, resulting increasing losses. There is therefore a large impact of the FPE angle on the group velocity that is dominated by non dispersive effects.

Group velocity reduction through Fabry-Perot

The quantitative understanding of the non-dispersive contributions to the group velocity is completed by a numerical simulation of pulse dynamics in the presence of the intracity FPE. The numerical model of the mode-locked laser includes a saturable gain, linear and saturable loss and FPE. Details of this numerical calculation are presented in Appendix C.

In each passage through FPE, an input pulse experiences multiple reflections and creates a group of trailing pulses with quickly decaying intensity, as expected for $R = 3.4$ %. Every member of the trailing pulses subsequently creates its own group of trailing pulses after one round trip though FPE and recombines with pulses of another group. Consequently, the pulse energy is transferred from the pulses ahead in time to the ones later in time through multiple reflections. Figure 6.6 shows the evolution of a bunch during first 50 round trips in the nested-cavity mode-locked laser. The initial pulse is given by a 2 ps Gaussian envelope. After the first passage (upper-left panel), a high frequency pulse train with inter-pulse period $\tau_{fp} = 148$ ps with quickly decaying intensity is generated. Since the energy flows from the front edge to the rear edge of a bunch, a symmetric bunch envelope starts forming after ~ 30 passages. In this simulation, the time axis is in a retarded frame of reference moving with the original pulse. A shift of the center of gravity of the bunch from the origin ($t = 0$) represents the group delay associated with the energy transfer. A near steady-state evolution of the pulse bunch shown in Figure 6.7 displays more clearly the slower velocity of the bunch envelope compared to the constituent pulses. The shift of the bunch envelope to the right (towards latter times) with increasing round-trips indicates the retardation of the center of gravity of the bunch in every round-trip with respect to the constituent pulses. Figure 6.8 shows the center of gravity of the bunch as a function of the number of round-trips for the first 300 round-trips. A positive slope indicates the retardation of the center of gravity of the

bunch with respect to the constituent pulses.

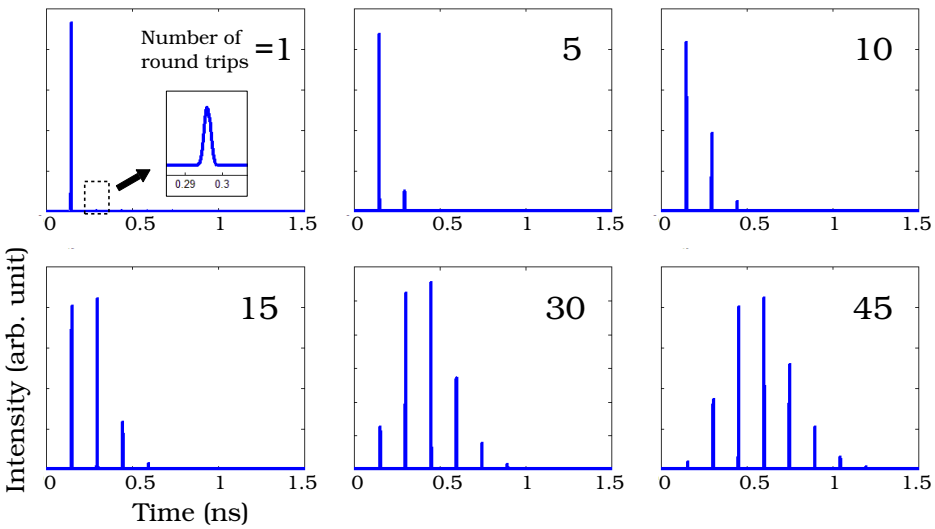

Figure 6.6: A numerical simulation showing the birth of the high frequency pulse train during the first 50 round trips. Time axis is in the retarded frame of reference moving with the pulses. The intensity profile of the pulse train initially decaying exponentially becomes more symmetric bell-shape after many passages through FPE placed inside a laser cavity.

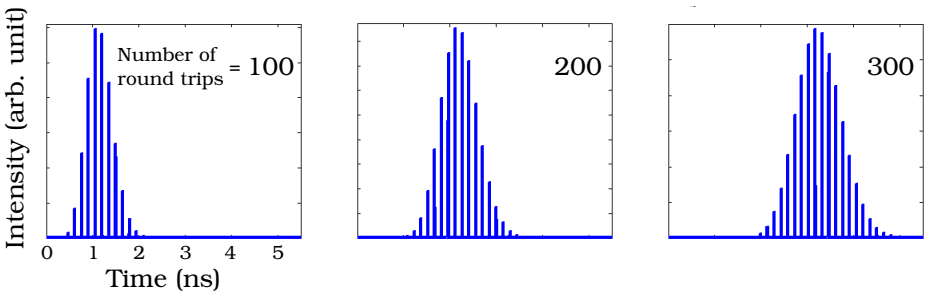

Figure 6.7: A near-steady state evolution of the high frequency pulse train. The envelope of a pulse bunch formed by at least 15 pulses moves slower than the constituent pulses, which can be seen as the motion of the envelope to the right.

The temporal retardation of the center of gravity of the bunch in every round-trip results in a reduced repetition rate. Compared to the repetition rate of a cavity without an intracavity FPE, the reduction is as much as 1.4 MHz, which is significant

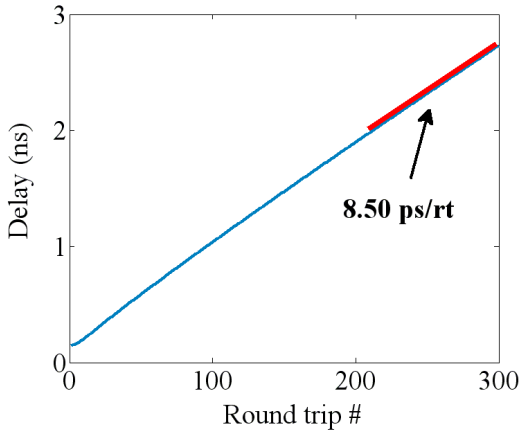

Figure 6.8: Evolution of the center of gravity (COG) of a bunch with the number of round-trips. The steady-state rate of change is 8.5 ps/rt is found in the numerical simulation. The effective life time T_p (Eq. (6.46)) is 22 ns.

compared to 250 kHz reduction expected for an addition of the path-length due to the 15.12 mm fused-silica FPE in the meter-long laser cavity.

Group velocity acceleration through Gain

As mentioned previously, a pulse group velocity is accelerated by a saturable gain. The same acceleration effect applies to the center of gravity of the bunch of pulses generated by FPE, as can be verified by the simple two-level rate equation approximation outlined below. The temporal evolution of a pulse in a gain medium is given by Eq. (6.44) and Eq. (6.45);

$$\frac{d\Delta N}{dt} = -\frac{I\Delta N}{W_s} - \frac{\Delta N - \Delta N_e}{T_p} \tag{6.44}$$

$$\frac{dI}{dz} = \sigma \Delta N I \tag{6.45}$$

where $\Delta N = N_2 - N_1$ is the population inversion, ΔN_e is the population inversion at equilibrium, W_s is the saturation energy density, σ is the absorption cross section and the effective decay rate of the laser transition determined by the natural lifetime

T_1 and the pump rate $\mathcal{R}$ is given by

$$\frac{1}{T_p} = \frac{1}{T_1} + \frac{\mathcal{R}}{2}. \tag{6.46}$$

The main parameter in this model appears to be the effective gain lifetime, T_p, if it is larger than the temporal extension of the high frequency pulse train, or the number of pulses in that bunch. This dependence is illustrated in the theoretical plot of Figure 6.9.

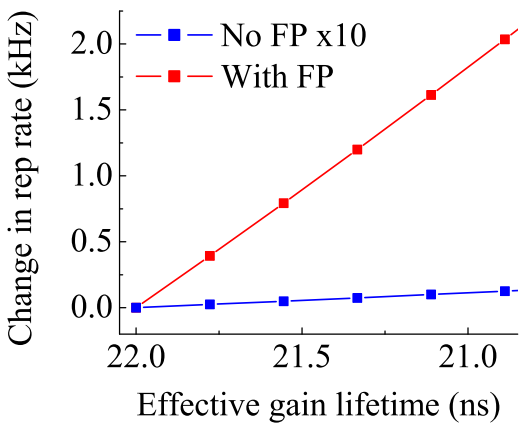

Figure 6.9: Numerical study of gain saturation effect. Changes in the laser repetition rate are calculated as a function of the effective life time of gain medium.

Group velocity dependence on pump intensity

The group velocity in a mode-locked laser cavity is influenced by the gain, a fact that has been exploited for laser stabilization. An electro-optic device [67] or an acousto-optic modulator [68] is placed to modulate the pump beam as a means to control the repetition rate of the laser without affecting the phase velocity.

Figure 6.10 shows an experimental measurement of the laser repetition rate as a function of the pump power, in presence or absence of an intracavity FPE. The

dependence on pump power is considerably enhanced when FPE is present in the cavity. The effective gain lifetime T_p decreases with increasing pumping rate, and therefore the plot of Figure 6.10 could serve as an explanation of the observed enhanced dependence of the group velocity brought in by the intracavity FPE. The effect of pump is however a little more complex. As will be shown in the next Section, as the gain increases, the number of pulses created by FPE also increases, modifying the delay of the center of gravity.

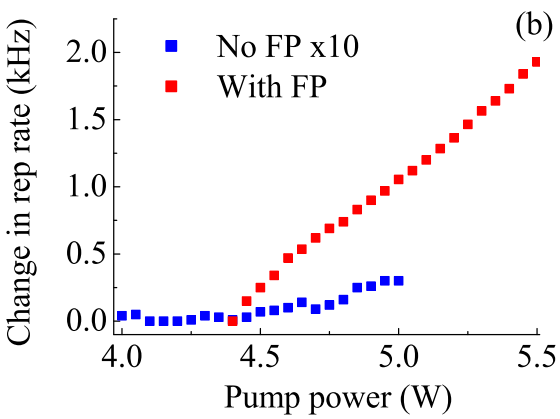

Figure 6.10: Experimental study of gain saturation effects. Changes in the laser repetition rate are measured as a function of pump power.

Group velocity dependence on Fabry-Perot angle

As mentioned above, group velocities associated with variations of optical path and index of refraction are dwarfed by gain and loss dynamics. Another example can be found in the repetition rate dependence of the nested-cavity mode-locked laser on the angle of a 15 mm intracavity etalon, as plotted in Fig. 6.11. An increase by as much as 30 kHz over 12 mrad angle range is measured. A model based solely on material dispersion and path length changes predicts approximately 300 Hz *reduction* of the

repetition rate over the range of angles in the figure.

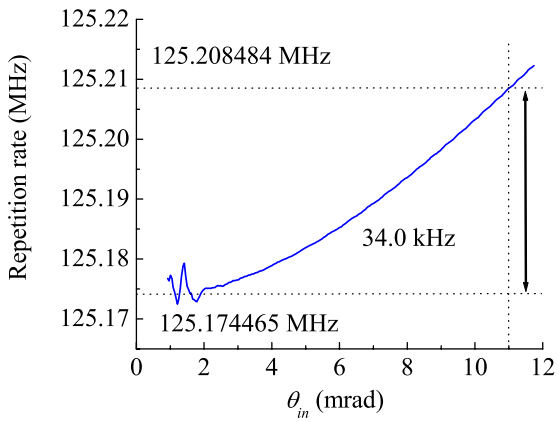

Figure 6.11: Experimental measurement of the repetition rate of the nested-cavity mode-locked laser as a function of the FPE internal angle θ_{in}.

To explain this unusual dependence of the repetition rate on the FPE angles, a loss of the laser cavity introduced by a tilted FPE is considered. Refraction in a tilted FP displaces a beam further from the optical axis as the angle increases. The left panel in Figure 6.12 shows the amount of displacement of the beam from the optical axis after one passage through FPE of different thickness as a function of the angle. Since the cavity mode has a finite width in the transverse direction, the cavity loss increases with the beam displacement. The right panel in Figure 6.12 shows measured laser threshold power as a function of the FPE angle, measured for a 15 mm and 10 mm fused-silica FPE. The threshold power increases with the angle as the cavity loss increases. It is noted that the threshold power for the thicker FPE increases more rapidly with the angle, since the beam displacement distance is proportional to the thickness.

Simulation of the repetition rate dependence of FPE angle: To simulate the group velocity influenced by the loss due the beam displacement, a simple numerical

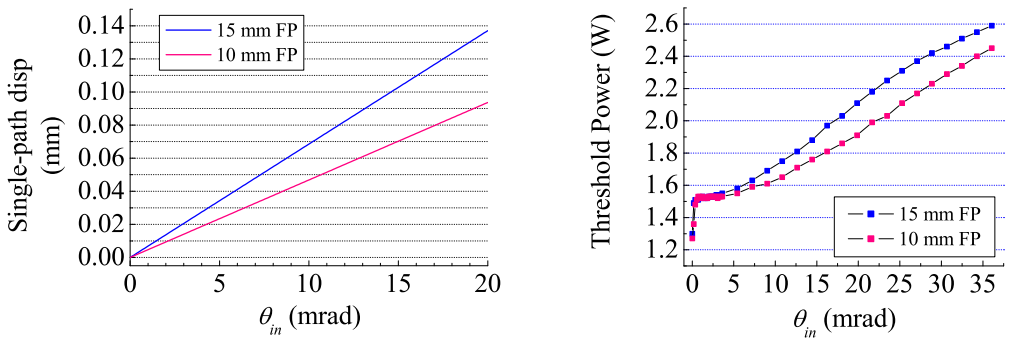

Figure 6.12: Left: Beam displacement as a function of FPE angle after a single passage through a 10 mm and 15 mm fused-silica FPE. Right: Angular dependence of laser threshold power for 15 mm and 10 mm fused-silica FPE.

model is developed. The key feature is an inclusion of an additional loss factor in the Fabry-Perot transmission function in Eq. (6.6).

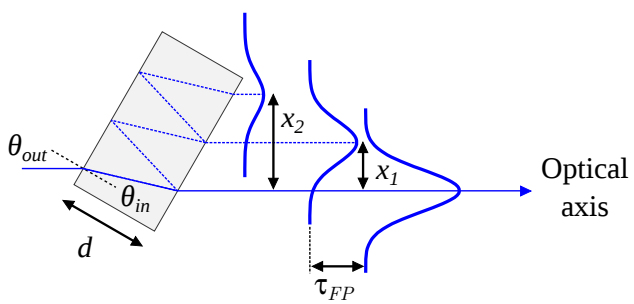

Figure 6.13: Multiple reflections in a tilted FPE cause beam displacements from the optical axis.

Referring to Figure 6.13, the center of the beam is displaced from the optical axis (i.e., the path of the beam transmitted without reflections) by

$$x_N = N \times 2d \tan\theta_{in} \cos\theta_{out} \tag{6.47}$$

where N is the number of round-trips. Assuming a fundamental Gaussian beam (TEM00), the field amplitude of a N_{th} reflected beam evaluated at the optical axis

is given by

$$A_N = e^{-x_N^2/w^2} = e^{-2\ln 2(x_N/\Delta)^2} \tag{6.48}$$

where w is the half-width of the field at $1/e$ and Δ is the intensity FWHM. A modified FP transmission function is then given by

$$\tilde{T}_{mod} = (1-R)e^{i\delta/2}(A_0 + A_1 R e^{i\delta} + A_2 R^2 e^{i2\delta} + A_3 R^3 e^{i3\delta} + \cdots) \tag{6.49}$$

As for the derivation of the standard Fabry-Perot transmission function, the sum could run to infinity. However, from a practical point of view, only finite terms are required to obtain sufficient accuracy. This simplification is particularly applicable to a low reflectivity FPE for which the intensity of the reflected beams is nearly vanished after a few round-trips, and contributions of the higher order terms to the sum are negligible. A truncated version of the transmission function is then

$$\tilde{\mathcal{T}}_{mod} = (1-R)e^{i\delta/2}\sum_{N=0}^{N'} A_N (Re^{i\delta})^N \tag{6.50}$$

Eq. (6.50) is readily incorporated into a numerical calculation.

Figure 6.14 shows a numerical simulation of the repetition rate as a function of the FPE tilt angle, where the repetition rate is defined as the center of gravity of the bunch. In this simulation, the following parameters are used: a laser cavity of $L = 1.2$ m, the FPE thickness $d = 15.12$ mm, $n_p = 1.4534$, $n_g = 1.4673$ and $\Delta = 400$ μm. The sum in (6.50) is determined up to $N = 10$. By comparing with the experimental measurement in Figure 6.11, this simple model based on the cavity loss due to beam displacement is in good agreement.

From these results, the anomalous increase of the repetition rate with the angle can be interpreted as increased cavity loss for the pulses in the tailing edge of the bunch with the FPE angle. As a result, the center of gravity of the bunch shifts forward in time, and the repetition rate increases.

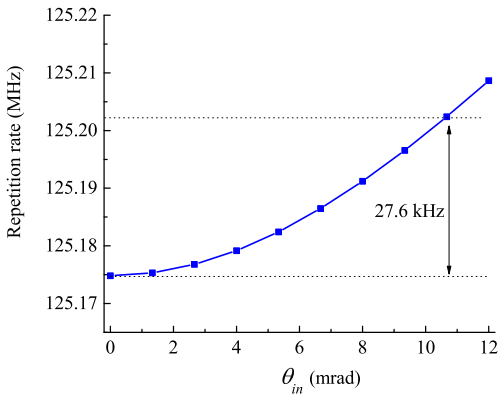

Figure 6.14: A numerical simulation of the angular dependence of the bunch velocity. An inclusion of the loss factor due to beam displacement into the modified FPE transmission function (6.50) reproduces an experimental observation in Figure 6.11.

6.6.3 Transition to single-pulse mode-locking

When the FPE angle is increased to a sufficiently large angle, the cavity loss exceeds the gain for all the multiply reflected pulses, and the laser starts operating in the single pulse mode-locking. It is interesting to observe how the repetition rate behaves when the laser make a transition from the nested-cavity mode-locking to the single-pulse mode-locking.

For the single pulse mode-locking, a transmission of an ultrashort pulse though a thick FPE is characterized by a group delay $\tau_{gr} = d\psi/d\Omega$. Using Figure 6.15, the repetition rate is expected to vary with the FPE angle according to

$$\begin{aligned} f'_{rep} &= \frac{c}{2}\left[\bar{n}_g l + n_g\overline{AB} + \bar{n}_g(L - l - \overline{AC})\right]^{-1} \\ &= \frac{c}{2}\left[\bar{n}_g L + \frac{d}{\cos\theta_{in}}\left\{n_g - \bar{n}_g\cos(\theta_{out} - \theta_{in})\right\}\right]^{-1} \\ &= \frac{c}{2}\left[\bar{n}_g L + \delta L\right]^{-1} \end{aligned} \tag{6.51}$$

where d and L are respectively physical length of FPE and the laser cavity, n_g is the group index of refraction of FPE, and $\bar{n}_g$ is the average group index of

the laser cavity. The change in the laser cavity length is given by δL, where $\delta L = d\{n_g - \bar{n}_g \cos(\theta_{out} - \theta_{in})\} / \cos\theta_{in}$. The internal and external angle are related though $\sin\theta_{out} = n_p \sin\theta_{in}$ where n_p is the phase index of refraction of FPE. Therefore, insertion of FPE into the laser cavity would reduce the repetition rate by

$$\delta f_{rep} = -\frac{\delta L}{L} f_{rep} \tag{6.52}$$

in the *absence* of the bunch formation. For example, with $L = 1000$ mm, $d = 15$ mm, $n_g = 1$, $n_p = 1.4534$, $n_g = 1.4673$ at normal incident $\theta_{out} = \theta_{in} = 0$ rad, a change in the repetition rate would be $\delta f_{rep} \approx -1.05$ MHz.

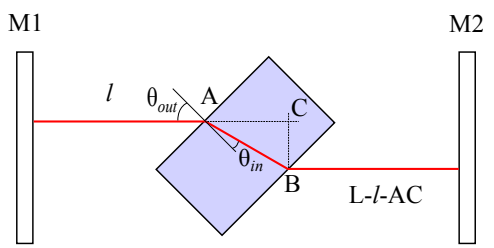

Figure 6.15: Geometry of a simplified laser cavity with an intracavity FPE.

Figure 6.16 shows the repetition rate around the angles where the transition from the multiple pulse to single pulse mode-locking takes place. For smaller angles, the repetition rate increases with the FPE angle, as presented above for the case of the nested-cavity mode-locked laser (left side of a dashed line). The transition occurs at approximately $\theta = 59°$. As soon as the laser switches to the single-pulse mode, the repetition rate starts following Eq. (6.51), as expected for the group velocity of a single pulse in the cavity.

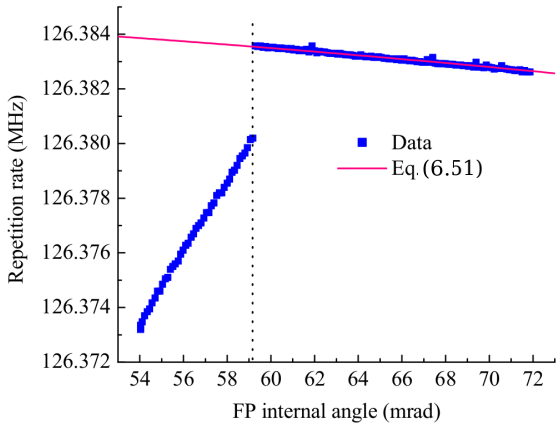

Figure 6.16: Repetition rate around the transition between the mode of operation. A red line is a fit given by Eq. (6.51), which agrees with the measurement.

6.6.4 Behavior of group velocity from a point of view of cavity resonance

So far in this section, the behavior of group velocity (repetition rate) of the nested-cavity mode-locked laser is explained in terms of the intrinsic energy transfer in FPE and the gain-loss balance. Here, a different view of the group velocity behavior based on the FPR transmission function is to be introduced. As discussed in Section 6.3, the phase of a transmitted pulse train with a finite number of pulses through FPE depends on the number of pulses and the gain, as shown in Eq. (6.48). The group velocity of the bunch should also depend on those parameters.

For simplicity of discussion, the gain is assumed to be linear and uniform in the frequency range around a Fabry-Perot resonance of interest. The gain factor a at each round-trip can be incorporated into the phase factor δ: $\tilde{\delta} = \delta - ia$, where $\tilde{\delta}$ is the previously defined complex phase factor, and δ is the real part of this phase factor.

The transmission function with gain is then given by

$$\tilde{\mathcal{T}}(\Omega) = \frac{(1-R)e^{a/2}e^{-ikd}}{1-Re^{a}e^{i\delta}} \tag{6.53}$$

Since a near-resonance transmission is considered[1], $\tilde{\mathcal{T}}(\Omega)$ can be expanded in series of $\delta = -2ikd = -2i\Omega n/c$, limiting to first order, to find:

$$\tilde{\mathcal{T}}(\Omega) = (1-R)e^{a/2}\left[\frac{e^{i\frac{\delta}{2}}}{(1-Re^{a})iRe^{a}\delta}\right]. \tag{6.54}$$

Consistent with these approximations, the phase angle is:

$$\psi = \delta/2 + \arctan\left[\frac{Re^{a}\delta}{1-Re^{a}}\right] \tag{6.55}$$

The group delay is the derivative of ψ with respect to Ω:

$$\frac{d\psi}{\Omega} = -\frac{nd}{c} - \frac{1}{1+S^2\delta^2}S\frac{nd}{c} \tag{6.56}$$

where

$$S = \frac{Re^{a}}{1-Re^{a}}. \tag{6.57}$$

The expression (6.56) is a function of frequency. The goal is to find the group delay near resonance, which means $\delta = 0$ or $\Omega = 0$. Therefore, a good approximation for the group velocity of the bunch is:

$$\frac{d\psi}{\Omega} = -\frac{nd}{c}\left[1 + \frac{Re^{a}}{1-Re^{a}}\right]. \tag{6.58}$$

It is interesting to note that, the smaller the difference $(1-Re^{a})$, the the narrower the Fabry-Perot resonance and the larger the number of pulses in the bunch, and also the larger the difference between group and phase velocity. This result is consistent with the experimental observations presented above, but derived in a different principle.

[1]Although the width of individual pulses is on the order of a few picosecond with a spectrum covering many transmission peaks, this approximation seems to work. The reason is that transmission of a train of picosecond pulses extending over a couple of nanosecond is equivalent to transmission of a single nanosecond pulse whose spectrum is narrower than the free-spectral-range of a centimeter FPE.

6.6.5 Comb structures

Radio frequency (RF) spectrum of the laser output is measured using a 13 GHz spectrum analyzer. Top plot in Figure 6.17 shows a RF spectrum of a standard mode-locked laser in the neighborhood of 6.8 GHz spectral region. The standard mode-locked train produces a flat-top RF spectrum with its mode spacing given by the repetition rate of the laser:

$$f_M = M \times f_{rep} \tag{6.59}$$

where M is an integer.

The spectrum of the nested-cavity mode-locked laser shown in the bottom plot in Figure 6.17 displays a bunch of modes in the neighborhood of 6.8 GHz. In comparison to the time domain profile in Figure 6.5, the mode structure around 6.8 GHz corresponds to inter-pulse period, $\tau_{fp} = 148$ ps, which is determined by the round-trip time of a pulse in the 15 mm fused-silica FPE. The width of spectral envelope is determined by the temporal extension of the bunch.

With the cavity length adjusted such that the mode spacing is equal to the standard mode-locked laser, the presence of an offset frequency is clearly visible, as can be seen more clearly in the inset plot. The offset is measured to be approximately 10 MHz.

This offset frequency is a direct consequence of the difference between the velocity of bunch envelope and the constituent pulses. As mentioned in the numerical simulations presented in Section 6.6.2, the bunch envelope travels slower than the constituent pulses. The slope of Figure 6.8 gives a relative delay, to be labelled as $\Delta\tau_{PB}$, between the bunch envelope and pulses per round-trip. The difference in their velocities results in a round-trip phase slippage between the bunch envelope and the pulses. In the frequency domain, a constant change in a phase becomes a frequency.

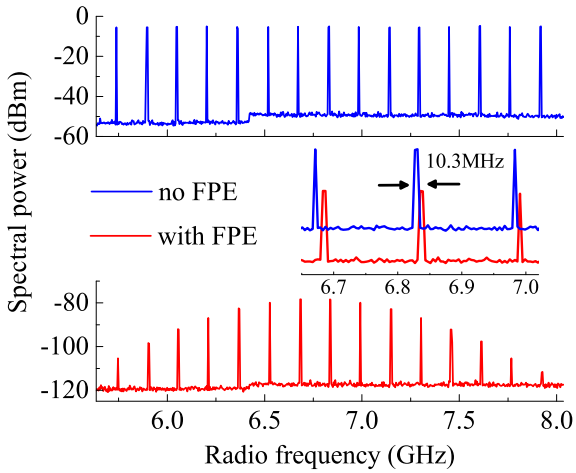

Figure 6.17: RF spectra of a single-pulse mode-locked laser with no FPE (top) and of the nested-cavity mode-locked laser with a 15 mm intracavity FPE (bottom). Both lasers are set to the same repetition rate. Inset: a zoom to indicate a shift of the spectrum of the pulse bunch train, resulted from the formation of the pulse bunches.

By deliberately applying the formula for the carrier-envelope offset (CEO) in the optical frequency comb arising from the difference between the carrier and group velocity [69], the offset frequency f_{PBO} can be given by

$$f_{PBO} = \frac{\Delta\phi_{PB}}{2\pi\tau_{rt}} = \frac{\Delta\tau_{PB}/\tau_{FP}}{\tau_{rt}} \tag{6.60}$$

To verify Eq. (6.60), f_{PBO} is estimated from the value of $\Delta\tau_{PB}$ obtained from the numerical simulation in Figure 6.8. For $\tau_{rt} = 1/155$ MHz $= 6.4$ ns and $\tau_{FP} = 1/6.8$ GHz $= 148$ ps, and $\Delta_{PB} = 8.5$ ps, $f_{PBO} = 9.0$ MHz is obtained, which is in good agreement with the measured offset in the RF spectrum in Figure 6.17.

6.7 Resonance condition of the nested-cavity

6.7.1 Link between high and low frequencies

The interference in FPE sets the resonance modes of FPE. Since these modes must add constructively at FPE after one round-trip in the laser cavity, they satisfy the resonance conditions of both the laser cavity and FPE simultaneously:

$$\frac{4\pi f L n_{pL}}{c} = 2\pi N_L \tag{6.61}$$

$$\frac{4\pi f d n_{pFP}}{c} = 2\pi N_{FP} \tag{6.62}$$

where f is the frequency of the mode, L and d are respectively length of the laser cavity and FPE, n_{pL} is the phase index of the laser, n_{pFP} is the phase index of FPE, and N_L and N_{FP} are integers. A ratio of Eq. (6.61) to Eq. (6.62) gives

$$\frac{n_{pL}}{n_{pFP}}\frac{L}{d} = \frac{N_L}{N_{FP}} \tag{6.63}$$

which is not necessarily an integer. The product of the repetition rate of FPE f_{FP} by the round-trip time in the laser cavity τ_{rt} gives a ratio of the high frequency (HF) component corresponding to f_{FP} and the low frequency (LF) component corresponding to f_{rep} of the RF spectrum:

$$f_{FP} \times \tau_{rt} = \frac{c}{2dn_{gFP}} \times \frac{2Ln_{gL}}{c} = \frac{n_{gL}}{n_{gFP}}\frac{n_{pFP}}{n_{pL}}\frac{N_L}{N_{FP}} = \frac{f_{FP}}{f_{rep}} \tag{6.64}$$

where n_{gL} and n_{gFP} are the group indices of the laser cavity and of FPE. Notice that both n_{gL} and n_{gFP} are different from the ordinary group indices determined by the material index of refraction, rather they are determined by the propagation though the nested-cavity as discussed in Section 6.6.2.

The ratio in Eq. (6.64) is very close to an integer. As outlined in Section 6.3.1, many round-trips ($p > 50$) are required to form the bunch of the high frequency (HF) pulse train. The construction of the high frequency pulse train can take place

only if the repetition rate of the HF train is near resonance with the laser cavity. This extraordinary additional resonance condition implies that the repetition rate of the laser, and that of the pulses constituting the HF train, are linked. The resonance condition of the HF train with the laser cavity can be expressed as

$$\frac{2f_{FP}n_{gL}L}{c} = M \tag{6.65}$$

where $M \sim L/d$ is very close to an integer, and the dependencies on the group index n_{gL} and the length L of the laser cavity are indicated explicitly. In the following sections, experimental observations of the coupling of HF and LF are presented.

6.7.2 Angular dependence

As described in Section 6.6.2, the group index of refraction of the laser cavity n_{gL} decreases with increasing angle of FPE, which dominates the angular dependence of the repetition rate (LF) that increases with the angle. Figure 6.18 shows the angular dependence of four modes of the RF (radio frequency) spectrum selected in the region around 6.8 GHz when a 15 mm fused-silica is placed in the laser. The ratio is approximately $L/d \sim 55$. In this plot, only every 5 modes are shown in order to indicate a change in the mode spacing. The high frequency mode corresponding to f_{FP} is centered around 6.8 GHz. The low frequency corresponding to the laser repetition rate is the spacing between the adjacent modes. The link between HF and LF is clearly seen. As LF increases with the angle, therefore with decreasing n_{gL}, HF increases in accordance with Eq. (6.65).

6.7.3 Dependence on the laser cavity length

If there were no coupling between the modes of the two cavities, HF would be unaffected by a change in the laser cavity length. However, due to the simultaneous

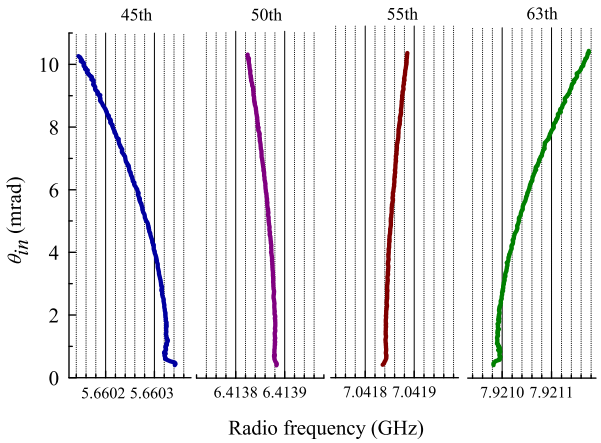

Figure 6.18: Angular dependence of high frequency modes around 6.8 GHz.

resonance conditions leading to Eq. (6.65), HF is affected by the laser cavity length. Figure 6.19 shows measurements of HF (left) and LF (right) while scanning the cavity length over 20 mm. LF, the laser repetition rate, varies linearly with the cavity length. Its slope agrees with the linear relationship between the repetition rate and the cavity length, given by $f_{rep} = c/2L$, as expected. Almost counter-intuitively, the HF mode also exhibits a linear dependence on the cavity length. The slope is found to be

$$\frac{\Delta f_{FP}}{\Delta L} = -\frac{f_{FP}}{L} \tag{6.66}$$

which is in excellent agreement with Eq. (6.65).

Direct time domain measurement

From Eq. (6.65), it is clear that when the laser cavity length is changed over one "wavelength ($= c/f_{FP}$)", M changes by ± 1. During a scan of the cavity length over several wavelength, therefore, an oscillatory behavior of the inter-pulse period, $1/f_{FP}$, should be observed. With a 1 m long laser cavity and a 6.5 mm long calcium

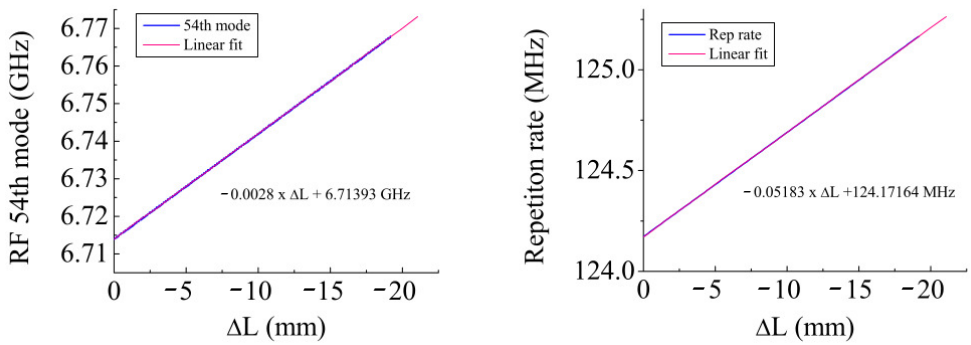

Figure 6.19: High frequency (left) and low frequency as a function of the cavity length.

fluoride (CaF_2) FPE, a maximum change in the inter-pulse period is approximately 0.5 ps. This value is close to the resolution of an auto-correlator available in our laboratories, therefore it is possible to measure the change in the inter-pulse period directly in the time-domain.

Figure 6.20 shows the inter-pulse period (τ_{fp}) of the HF train measured both in the time-domain and frequency-domain as a function of the laser cavity length. The time-domain measurements (red squares) are obtained by measuring the inter-pulse period using an auto-correlator. An 8 RPM synchronous motor is employed to scan the delay line over 5 cm, corresponding to a total scanning range of 330 ps. With a 6.5 mm CaF_2, the inter-pulse period is approximately $\tau_{fp} = 61.5$ ps. Therefore, 5 peaks of interferometric auto-correlation of the HF train are obtained in a single scan. The temporal separations between the peaks are determined by the maximum likelihood fitting method. The points plotted in the figure is the average of the 4 values determined by the method described above.

The frequency measurements are obtained for three RF modes around the HF mode of FPE ($f_{FP} \approx 16.2$ GHz), labelled as f_{126}, f_{127} and f_{128}. In order to compare with the time-domain measurements, the measured frequencies are converted into their inverse.

The time and frequency domain measurements seem to agree quite well. This result further supports our conclusion that the inter-pulse period is coupled to the laser cavity length. A systematic discrepancy between the two measurements, seen as lower values of the frequency measurements, is due to a calibration of the RF spectrum analyzer. By referencing it to a RF standard, this error should be removed.

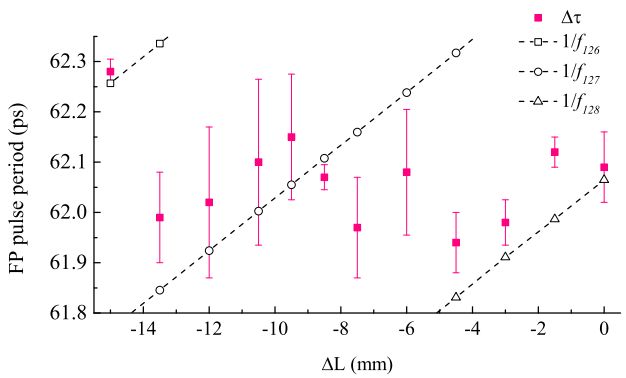

Figure 6.20: Experimental measurements of the inter-pulse period τ_{FP} of the HF pulse train, measured both in time-domain (solid squares) and in the frequency-domain.

6.8 Application for precision measurement of a change in index of refraction

6.8.1 Concept

The goal is to exploit the coupling of the high frequency of FPE and the low frequency of the repetition rate of the laser for a high resolution measurement of a small change in the index of refraction of FPE. As described above in Section 6.7, the coupling of HF and LF arises because of the simultaneous resonance of the two cavities. The

ratio of HF to LF as given as

$$\frac{f_{FP}}{f_{rep}} = \frac{n_{gL}}{n_{gFP}} \frac{n_{pFP}}{n_{pL}} \frac{N_L}{N_{FP}} \tag{6.67}$$

must be very close to an integer in order for the HF pulse train to form. The first term of the right hand side is a ratio of the group index of the laser cavity to that of FPE, which are predominantly determined by pulse dynamics due to gain-loss balance (Section 6.6.2) and to the condition for the build-up of the HF pulse train. The third term is a ratio of integers which are determined by the physical dimension of the cavities, L and d. Therefore, the first and the third terms remain the same as long as the cavity conditions, including pump power, alignment, and cavity length, are unchanged. Now, the second term is a ratio of the phase index of refraction of FPE to that of the laser cavity, which are unique physical quantities to the material of the object. Assuming the cavity conditions are unchanged, if there is a change in the index of refraction of FPE, it will be reflected to the ratio of HF to LF.

Index change due to radiation damage

It is known that a bombardment of high-energy particles, such as photons, neutrons, electrons and protons, onto an optical glass causes defects in the crystal structure and induces a change in the index of refraction [70, 71, 72]. For trial experiments, several samples of CaF_2 are to be irradiated by neutrons from a PuBe neutron source with different dosages.

6.8.2 Initial experiments

A detection of a change in the index due to radiation damage is based on difference of the HF-LF ratio between pre- and post-irradiation. Therefore, all the cavity conditions, including the cavity gain (loss) and cavity alignment, must be kept con-

stant over the course of measurement. The purpose of the initial experiments is to test the system's consistency. Three CaF_2 FPEs to are used for these experiments. Their physical thickness, measured based on mechanical measurement, are listed in Table 6.6. The mode-locked laser used in this experiment is the same as described throughout this chapter. Each FPE sample is placed on a mount which is fixed in the cavity, and the FPE high frequency mode and the laser's repetition rate are recorded using a 26 GHz RF spectrum analyzer and a frequency counter for 1 min. An example of the measurement of FPE mode is shown in the left panel in Fig. 6.21. After recording the two frequencies with one sample, another FPE sample is replaced without touching cavity optics, and the same measurements are repeated. Data for three samples comprises one data set. This procedures is repeated to make a total of 5 sets. Results are shown in the right panel of Figure 6.21. Over the course of the measurement, there is a systematic shift of the frequency of all three samples.

Sample #	Thickness (mm)
1	6.4727
2	6.4740
3	6.5120

Table 6.6: Mechanically measured thickness of CaF_2 FPE samples.

Differential measurement is more advantageous because it is less dependent on the cavity misalignment. Difference frequencies are calculated between the FPE high frequency mode for each sample within the same measurement set. For example, the difference frequency between the sample #1 and #3 in the measurement set #1 is $f_{13} \equiv f_1 f_3$. The result is shown in the left panel in Fig. 6.22. The same analysis is done for the repetition rate, shown in the right panel.

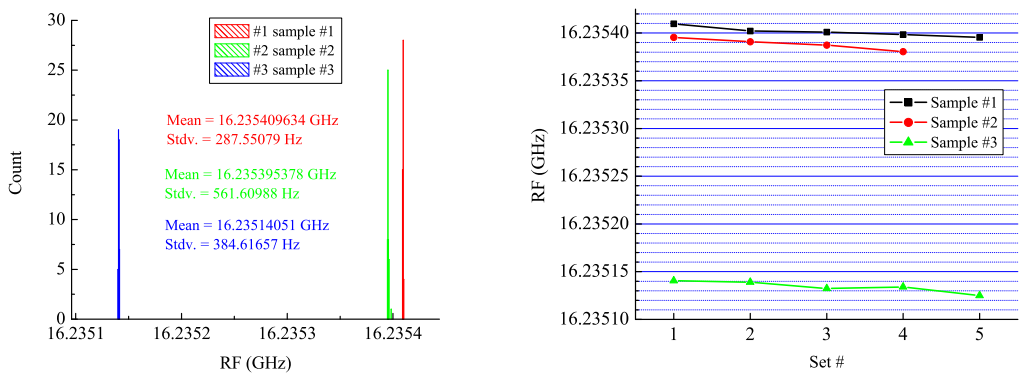

Figure 6.21: Measurements of the FPE high frequency mode for each sample, measured with a 26 GHz spectrum analyzer over 1 min. Left: a data from one set of the measurement. Right: data for all 5 measurement sets.

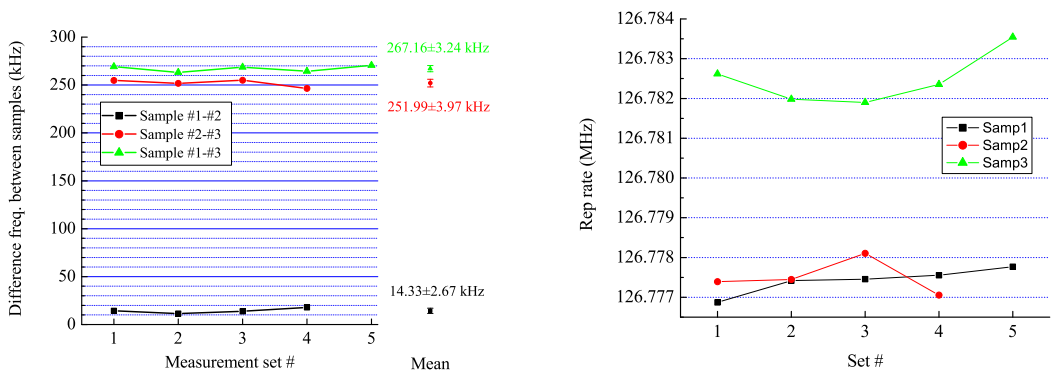

Figure 6.22: Difference of the high frequencies (left) and the repetition rate (right) between the the samples for each measurement set.

Results

The thickness of sample #3 is different from other two samples by approximately 0.5% of its thickness. From the high frequency measurement in Figure 6.22, the resolution can be determined as

$$\mathcal{R} \simeq \frac{f_{13}}{\Delta f_{13}} = \frac{267.16\text{kHz}}{3.24\text{kHz}} = 82.46 \tag{6.68}$$

In principle, it should be able to resolve $0.5\%/82.5 = 0.006\%$ change in thickness or equivalently in the index of refraction. For CaF_2 with $n = 1.4305$, it should be able to detect a change of

$$\Delta n = 0.00006 \times 1.4305 \approx 10^{-4} \tag{6.69}$$

The width Δf_{ij} is currently limited by the inaccuracy between the measurement sets. This can be improved by building more stable apparatus. If this was done, the ultimate width is given by the fluctuation of the measurement within a set, which in my current data is ≈ 300 Hz at best. With this value, the resolution improves by a factor of 10.

6.8.3 A method for better sensitivity

In Figure 6.23, the ratio of HF to LF is plotted as a function of the FPE angle for two different FPEs of the same index but with slightly different thickness. The angular dependence of the ratio is due to the change in the cavity group index (the first term in (6.67)), which is affected by the gain-loss balance. What is remarkable in this measurement is that the two curves are nearly parallel. It means that the angular dependence of the gain-loss balance has not been changed between the two measurements. The only change made between the two measurements are the thickness of the FPEs. The remarkable performance of this method implies that the sensitivity can be further improved by two orders of magnitude ($\Delta n \sim 10^{-6}$).

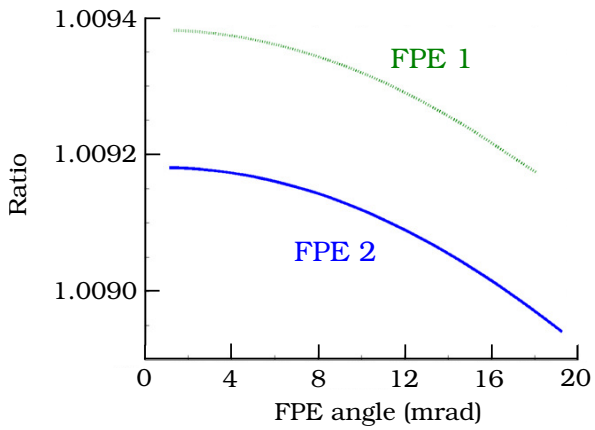

Figure 6.23: Ratio between the high RF and low RF as a function of the FPE angle.

6.9 Conclusion

In this chapter, the generation of the interwoven frequency comb from the nested-cavity mode-locked laser is demonstrated. The interwoven frequency comb is composed of two frequency combs with different mode spacing, with the low frequency from the repetition rate of the laser cavity and the high frequency from the mini-pulse train generated due to an intracavity FPE. The properties of the new class of mode-locked laser, including the frequency tunability, dependence of the comb spacing on the gain and loss, and the intricate coupling between the low and high frequencies due to a coupled-cavity resonance condition, are scrutinized. An exploitation of the relation between the high and low frequencies through the cavity resonance to a measurement of the index of refraction of FPE is proposed. A potential to measure a small change in the index of refraction due to a structural damage in a crystal by nuclear radiation is demonstrated.

Chapter 7

Conclusions

The contributions presented in this dissertation are centered around the development of ultra-sensitive mode-locked laser sensors based on a measurement of intracavity phase shift. Towards the realization of Intracavity Phase Interferometry (IPI) atomic magnetometor, experimental studies of interaction of a mode-locked pulse train with a ^{87}Rb vapor are performed in both extra- and intra-cavity configurations. Also, a new class of the frequency comb, the interwoven frequency comb, which is invented during this dissertation work, is extensively studied both experimentally and numerically, and its application for a precision measurement of index of refraction is presented.

Coherent population trapping (CPT) of a ^{87}Rb vapor is introduced as a method to prepare a long-lived macroscopic magnetization in the vapor using a mode-locked laser. CPT of ^{87}Rb occurs because of a strong coherence between the ground-state hyperfine sublevels which renders the atoms to be decoupled from the excitation electric field. With a mode-locked pulses, CPT of a ^{87}Rb vapor is realized when the repetition rate matches to a submultiple of the ground-state hyperfine splitting. Using a vapor cell with no buffer gas or anti-relaxation coatings, shielded from ambient

magnetic fields, a dark-line resonance (a dip in a fluorescence signal) with 11 kHz linewidth is observed when the repetition rate is scanned across the CPT resonance. By applying a longitudinal static magnetic field and using a train of circularly polarized pulses, optical pumping of the atomic population into a superposition of the magnetic field sensitive sublevels is achieved.

Further enhancement of the optical pumping is demonstrated by means of a spectral shaping using an intracavity Fabry-Perot etalon (FPE) which is placed in the mode-locked laser cavity. By choosing a FPE with low surface reflectivity and the free-spectral-range closely matching to the ground-state hyperfine states of ^{87}Rb, spectral overlap between the excitation pulse train and the atomic transitions is significantly increased. As a result, more spectral power is utilized in the preparation of CPT, and the contrast of the dark-line is improved by nearly a factor of 3. An improvement of the optical pumping is also achieved. Due to a emergence of an offset frequency in the spectrally shaped frequency comb, the resonance repetition rate is shifted by as much as 200 kHz compared to the resonance frequency induced by a standard mode-locked pulse train.

Preparation of CPT of a ^{87}Rb vapor using a sequence of pulses with alternating right and left circular polarizations is experimentally investigated. This pumping scheme, known as the push-pull optical pumping, simulates the pulse sequence encountered in a CPT-based IPI atomic magnetometer. With a delay between two orthogonal circular polarizations set to a half integer multiple of the inverse of the ground-ground state hyperfine splitting, a large fraction of the atomic population is pumped into the 0-0 superposition state using a cell containing N_2 buffer gas placed in a longitudinal static magnetic field. Consequently, a strong and narrow ($\sim$ 4 kHz) dark-line signal is obtained from the 0-0 superposition state which is insensitive to magnetic field, while a very small signal obtained from the field sensitive superposition states. This result suggests that an alternative pumping scheme, for example

pumping with a pulse train with unequal intensity between RCP and LCP, needs to be investigated for an application for a magnetometer.

Following the extracavity studies, coherent propagation of resonant picosecond pulses in a ^{87}Rb vapor inside the laser cavity are studied both experimentally and numerically. When the laser frequency is resonant with the D1 transition frequency, significant pulse shaping effects, including pulse broadening and amplitude and/or phase modulation, are observed. By varying the number density of the vapor, a linear dependence of the pulse group velocity, which is measured based on the laser repetition rate, is also observed. Those observations are consistent with the characteristics of coherent propagation of a resonant optical pulse in a two-level atomic system, particularly, the well-known nonlinear optical phenomenon of self-induced transparency. A simple numerical model based on propagation of a resonant picosecond pulse in a three-level atomic system agrees reasonably well with the experimental observation of the slow light propagation, although a discrepancy between the experimental and numerical data is not negligible. There is also a disparity between the measured area and the expected value of 2π which is known to be stable in some experimental conditions, which may not be applicable to the experiments presented in this dissertation.

A dark-line is observed in the intracavity vapor cell when the repetition rate is tuned to the CPT resonance. Surprisingly, the resonance line-shape is not very different from the dark-line observed in the extracavity experiments, despite the fact that the intracavity intensity is nearly 2 orders of magnitude larger. The occurrence of the intracavity CPT can be attributed to a return of the atomic population to the ground-state after coherent interaction with a picosecond pulse having sufficiently large area.

Finally, a new type of frequency comb, the interwoven frequency comb, is demonstrated. By placing a centimeter long Fabry-Perot etalon in a meter long laser cavity,

termed as the nested-cavity mode-locked laser, a frequency comb composed of 7 GHz high frequency modes surrounded by 100 MHz low frequency modes is generated. The counter-intuitive properties of the comb include the pronounced dependences of the group velocity on the FPE angle and the laser gain, the presence of an offset frequency and coupling of the high and low frequency modes. By exploiting the coupling of the modes, which arises because of the simultaneous resonance of the two cavities, a method to extract a relative change of the index of refraction of FPE is proposed, and a proof of principle measurement is demonstrated for its feasibility.

Appendices

Appendix A

Parameters in coherent interaction with ^{87}Rb

A.1 Dopper broadening of ^{87}Rb vapor

For a vapor state ^{87}Rb atoms, the inhomogeneous broadening is dominated by the Doppler broadening. A Doppler broadened inhomogeneous lineshape is represented by a Gaussian:

$$g(\omega_0' - \omega_{ih}) = \frac{2}{\Delta\omega_D}\sqrt{\frac{\ln 2}{\pi}}e^{-(\omega_0'-\omega_{ih})^2/\Delta\omega_D^2} \tag{A.1}$$

where $\Delta\omega_D$ is FWHM of the Doppler broadening width. The lineshape function g in Eq. (A.1) satisfies the normalization condition;

$$\int_{-\infty}^{\infty} g(\omega_0' - \omega_{ih})d\omega_0' = 1 \tag{A.2}$$

The Doppler width $\Delta\omega_D$ at a given temperature T is given by [73],

$$\Delta\omega_D = 2\omega\sqrt{2\ln 2\frac{k_B T}{mc^2}} = \frac{4\pi}{\lambda}\sqrt{2\ln 2\frac{RT}{M}} \tag{A.3}$$

The parameters in Eq. (A.3) for ^{87}Rb are summarized in Table A.1. For example, at $T = 297$ °K, the Doppler width is $\Delta\omega_D = 2\pi \times 499.3$ MHz.

Symbol	Relation	Value	Unit	Description
k_B	-	1.381×10^{-23}	J/°K	Boltzmann const.
N_{av}	-	6.022×10^{23}	mol^{-1}	Avogadro's num.
R	$N_{av} \times k_B$	8.3143×10^3	$\text{m}^2 \cdot \text{g/s}^2 \cdot$°K $\cdot$ mol	-
M	-	86.91	g/mol	Molar mass
m	M/N_{av}	-	g	Atomic mass
c	-	2.997925×10^8	m/s	Speed of light
λ	-	795×10^{-9}	m	Wavelength of light
ν	c/λ	377×10^{12}	Hz	Frequency of light

Table A.1: Parameters used to calculated the Doppler width in Eq. (A.3) of ^{87}Rb.

A.2 Absorption coefficient

A simple approximation to find the absorption coefficient α for an inhomogeneously broadened medium is to replace T_2 by T_2^* in the expression for the absorption coefficient. The absorption cross-section is then

$$\sigma = \frac{p^2 T_2 \mu_0 \epsilon_0 \omega^2 c}{\epsilon_0 \omega n \hbar} = \frac{p^2 T_2 \omega}{\epsilon_0 c n \hbar} = \frac{2\pi p^2 T_2}{\epsilon_0 \lambda n \hbar} \tag{A.4}$$

For a ^{87}Rb vapor at room temperature, and taking $T_2^* = 1/(2\pi \times 500 \text{ MHz}) = 0.318$ ns, we have

$$\sigma = 0.175 \times 10^{-10} \text{cm}^2 \tag{A.5}$$

where $p = 2.54 \times 10^{-29}$ C·m is the electric dipole moment of D1 transition of ^{87}Rb and $n = 1$ is the index of refraction of the ^{87}Rb vapor in vacuum.

The vapor pressure is calculated according to [5]:

$$\log_{10} \text{P}_\text{v} = 2.881 + 4.857 - \frac{4215}{\text{T}} \tag{A.6}$$

Appendix A. Parameters in coherent interaction with ^{87}Rb

At a room temperature, $T = 297$ K,

$$P_v = 3.575 \cdot 10^{-7}\text{Torr} = 4.766 \cdot 10^{-5}\text{Pa} \tag{A.7}$$

From the ideal gas law,

$$N = \frac{Pv}{k_B T} = \frac{4.766 \cdot 10^{-5}}{1.381 \cdot 10^{-23} \times 297} = 1.161 \cdot 10^{10}\ /\text{cm}^3 \tag{A.8}$$

The absorption coefficient is then,

$$\alpha_0 = \sigma_0 \times \text{N} = 0.20\ \text{cm}^{-1} \tag{A.9}$$

For a 7 cm long cell, $\alpha L = 0.2\ \text{cm}^{-1} \times 7.0\ \text{cm} = 1.4$.

Appendix B

Design consideration for a vapor cell for an intracavity use

B.1 Effects of the window design on mode-locking operation

There are several requirements for the design of the ^{87}Rb vapor cells used in the intracavity experiments. The most important one is a scattering loss on the windows, which must be minimized for a use inside a laser cavity. Several types of windows are examined; including Brewster-cut windows, anti-reflection (AR) coating on both outer and inner surfaces, a thin 1 mm window and a large-angle wedged window with AR coating only on the outer surfaces.

The Brewster-cut and the double-sided AR coating windows introduce the least loss and require less pumping power. However, it is found that both window types cause the laser frequency to become unstable and strongly dependent of the angle between the window surface and the beam. For the Brewster-cut window, it is most

likely due to the polarization-dependent bandwidth of the laser, which makes the laser frequency very sensitive to the incident angle of the beam. For the double-sided AR coated cell, it is due to a generation of multiple pulses, despite a very low reflectivity ($< 1\%$). The generation of intracavity multiple pulses is almost always encountered in intracavity experiments, therefore is treated in great detail in Chapter xx.The same effect of the multiple pulse generation is also observed with a thin 1mm windwo. Both effects of the polarization-dependent instability and the multiple pulse generation make a fine-tuning of the laser frequency to the atomic resonance very challenging. Figure B.1 shows auto-correlation traces of a pulse train when a cell with the double-sided AR coated widow (left) and the 1 mm thin-plate (right) windows is inserted in the laser cavity. Multiple pulses separated by a round-trip time of the respective windows are clearly visible in both cases.

To prevent the interference of the cell windows with the laser frequency, a cell with one-sided AR coated wedged widows is designed. The window has a wedge at 3° and AR coated on the outer surface only. Due to the wedge surfaces and one-sided AR coating, the cell does not generate multiple pulses or cause the polarization-dependent instability, although the large wedge produces more cavity loss. Only by pumping at high power (> 5 W), the laser can be mode-locked.

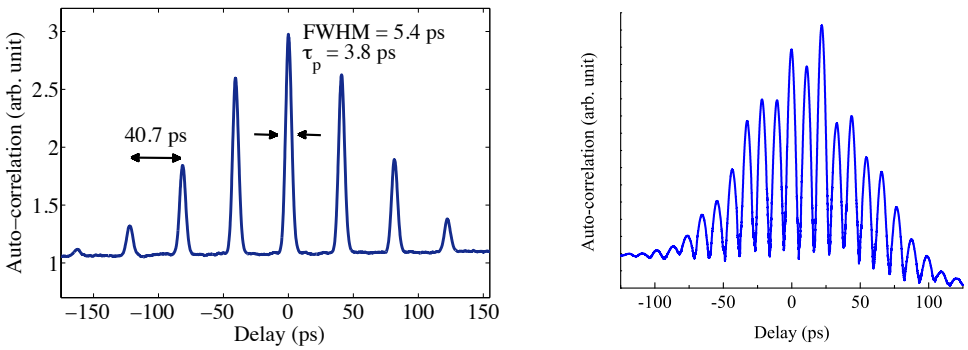

Figure B.1: Left: Intensity auto-correlation of a pulse train when a cell with 4.2 mm fused-silica windows with double-sided AR coating is placed in the cavity. Despite the double-sided AR coating on both outer and inner surfaces, the multiple pulses are generated, causing the intracavity Fabry-Perot interference effect. Right: The same multiple pulse generation is observed with a cell with 1 mm thin Pyrex windows.

Appendix C

Numerical simulation of the Fabry-Perot high frequency pulse train

C.1 Introduction

The goal of this numerical simulation is to study how a pulse bunch is formed from a single pulse in the presence of an intracavity FPE and how different parameters of both FPE and the laser affect its intracavity evolution and dynamics.

For simplicity, the nested-cavity mode-locked laser is modeled by the cavity elements including FPE, laser gain, saturable absorber, a bandpass filter and a linear loss of the whole cavity. A flow-chart of the simulation is shown in Figure C.1. Since some elements are described more conveniently in the time domain, while others in the frequency domain, the simulation domain is switched back and forth between time and frequency domain by using Fast Fourier Transform (FFT) functions.

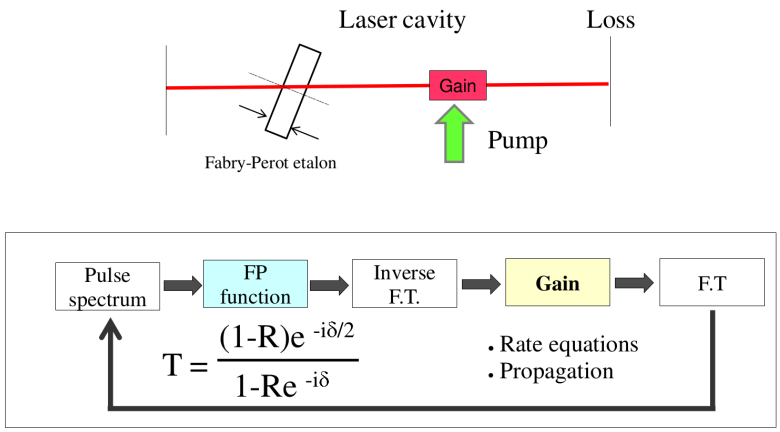

Figure C.1: A diagram indicating the cavity elements and a flow-chart of the numerical simulation of FPE pulse train.

C.2 Fabry-Perot etalon

For the purpose of our study, where only the forward propagation have a dominant effect, the transmitted fields are only considered and ignore the reflected fields. The linear transmission function of a Fabry-Perot etalon is described in the frequency domain as

$$\tilde{E}_{FP} = \tilde{E}(\Omega)\tilde{\mathcal{T}}(\Omega) \tag{C.1}$$

where

$$\tilde{\mathcal{T}}(\Omega) = \frac{(1-R)e^{-i\delta/2}}{1-Re^{-i\delta}} = |\tilde{\mathcal{T}}|e^{-i\psi} \tag{C.2}$$

where $\delta = 2\omega_0 n_p d\cos\theta_{in}/c$. Here, n_p is a linear phase index of refraction of the material, which is given by the Sellmeir's dispersion formula [50]:

$$n^2(\lambda) = 1 + \frac{B_1\lambda^2}{\lambda^2 - C_1} + \frac{B_2\lambda^2}{\lambda^2 - C_2} + \frac{B_3\lambda^2}{\lambda^2 - C_3} \tag{C.3}$$

Eq. (C.3) is an empirical formula and only applies to the wavelength region where the absorption is negligible.

As described in section 6.6.2, the additional loss term due to beam displacement must be included in order to accurately capture the effects of FPE *inside* the laser cavity. Repeating the procedures described in section 6.6.2, the initial transmitted beam is displaced with respect to the incoming beam by

$$X_0 = \frac{d\sin(\theta_{out} - \theta_{in})}{\cos\theta_{in}} \tag{C.4}$$

The displacement of N-th transmitted beam with respect to the position of the initial transmitted beam is given as

$$X_N = N \times 2d\tan\theta_{in}\cos\theta_{in} \tag{C.5}$$

Here, two assumptions simplify the problem. First, the beams have the fundamental Gaussian profile (TEM00). Second, lasing action can only occur along the optical path of the initial transmitted beam. These assumptions are of course a coarse approximation and maybe oversimplifying the problem. However, as shown in section 6.6.2, they are surprisingly good ones and capture the mechanism leading to the angle dependence of the repetition rate.

With these approximations, the coefficients accounting for the additional loss of the N-th beam can be identified as the amplitude of the Gaussian beam centered at X_N evaluated at the position of the initial transmitted beam:

$$A_N = e^{-X_N^2/w^2} \tag{C.6}$$

When $\theta_{in} = 0$, $X_N = 0$ and therefore $A_N = 1$, as expected for the case when all the multiply reflected beams are aligned along the optical path of the initial transmitted beam.

To find a modified transmission function containing the additional loss factor due to the beam displacement, all the transmitted fields are summed up:

$$\tilde{T}_{mod} = (1-\mathcal{R})e^{i\delta/2}(1 + A_1\mathcal{R}e^{i\delta} + A_2\mathcal{R}^2e^{i2\delta} + A_3\mathcal{R}^3e^{i3\delta} + \cdots) \tag{C.7}$$

As in the case of usual FPE transmission, the sum could be run infinity. However, it would be mathematically involved because of the exponential factor in Eq. (C.6). The problem is greatly simplified in a practical point of view. Instead of summing up to infinity, it can be truncated after finite terms. This is especially legitimate for a low reflectivity FPE, since after a few round-trips through the low-reflectivity FPE the intensity of the beam is nearly vanished and its contribution to the sum is negligible. A truncated version of the transmission function is then

$$\tilde{T}_N = A_N(1-R)e^{i\delta/2}\sum_{N=1}^{N'}(Re^{i\delta})^{N-1} \tag{C.8}$$

C.3 Gain medium: rate equation

The gain dynamics is described by the rate equations for the population of the laser medium. Our focus here is on the titanium-sapphire crystal. Titanium-sapphire is represented as a four-level system [74]. A green pump laser at 532 nm promotes the ground state population to the upper excited state, immediately followed by transition to the lower excited state via lattice relaxation. The lower excited state has a long lifetime of the order of microsecond before de-excited by spontaneous emission of a photon to the upper ground state which in turn quickly decays to the lower ground state. Therefore, suitable for creating population inversion. Ti:sapphire lasers operates on the transition from this lower excited state to the upper ground state. Once reaching the upper ground state, the population quickly decays to the lower excited state and is recycled in the process.

In a model of a cw mode-locked laser, the long period between pulses ($\sim$ns) and the ultrashort pulse width (fs $\sim$ ps) make the population in the fast decaying levels irrelevant. In those cases, the gain medium is represented as an effective two-level system. Moreover, a cw mode-locked pulse train has a constant intensity profile

from pulse to pulse. Thus, the saturation and recovery of the medium, which can be replaced by the effective lifetime, are also invariant from pulse to pulse basis. This is also true for a multi-GHz pulse train. On the other hand, if one of the following conditions is met:

- The pulse period is comparable to lifetime of short lived levels
- Inter-pulse intensity variations exist within the lifetime of these short-lived levels,

such as a pulse train generated from the nested-cavity mode-locked laser, then the two-level representation is no longer a good approximation.

In order to construct an accurate model for the interaction of the pulse bunch train with a Ti:Sapphire crystal, a short-lived third level must be added to the model. Figure C.2 shows the three level representation of Ti:sapphire being discussed here, along with relevant excitation and relaxation passages. The rate equation is then given as

$$\begin{aligned}
\frac{dN_1}{dt} &= \frac{I}{W_s}(N_2 - N_1) - \frac{I_p}{W_p}(N_1 - N_3) + \frac{N_2}{T_1} \\
\frac{dN_2}{dt} &= -\frac{I}{W_s}(N_2 - N_1) - \frac{N_2}{T_1} + \frac{N_3}{\tau_3} \\
\frac{dN_3}{dt} &= -\frac{I_p}{W_p}(N_1 - N_3) - \frac{N_3}{\tau_3}
\end{aligned} \tag{C.9}$$

where $W_p = h\nu_p/\sigma_p$ and $W_s = h\nu_l/\sigma_l$ are the saturation energy densities for the pump and for the laser, with ν_p, ν_l and σ_p, σ_l the cyclic frequency and the absorption (emission) cross-section of the pump and laser field, respectively, h the Plank's constant, $1/T_1$ the spontaneous emission rate of the upper laser level and $1/\tau_3$ the relaxation rate of $3 \rightarrow 2$ transition, which is assumed to be very fast, of the order of τ_{FP}. The laser field is amplified according to:

$$\frac{dI}{dz} = \sigma(N_2 - N_1)I = \sigma \Delta N I \tag{C.10}$$

where σ is the gain cross-section and $\Delta N = N_2 - N_1$ is the population inversion.

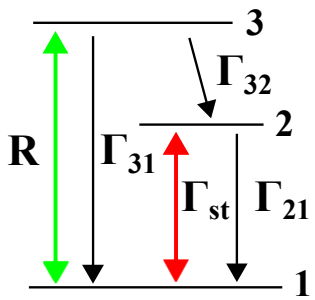

Figure C.2: Energy levels and transitions passages in a simplified Ti:sapphire.

Eq. (C.9) can be solved numerically. However, since the simulation involves a wide range of time scales, ranging from sub-picosecond for the structure of individual pulses to a few nanosecond of the cavity round trip time, to solve the differential equations for each smallest time step is computationally expensive and inefficient. Fortunately, owing to the nature of a pulse train, the rate equation can be greatly simplified and can be solved more efficiently. Our approach is to divide the problem into three different parts based on the time scale. In particular, inside a train of pulse bunches, there are three different time scales corresponding to 1) between bunches: $\sim$ 7 ns, 2) between pulses: $\sim$ 150 ps and 3) for the duration of a single pulse: $\sim$ 4 ps. The following is our treatment of the rate equation in each regions.

Region I: Between bunches

Since there is no pulse in the gain medium during this period, $I = 0$. Then,

$$\begin{aligned}
\frac{dN_1}{dt} &= -\frac{I_p}{W_p}(N_1 - N_3) + \frac{N_2}{T_1} \\
\frac{dN_2}{dt} &= -\frac{N_2}{T_1} + \frac{N_3}{\tau_3} \\
\frac{dN_3}{dt} &= \frac{I_p}{W_p}(N_1 - N_3) - \frac{N_3}{\tau_3}
\end{aligned} \tag{C.11}$$

However, since $\frac{I_p}{W_p} \ll 1/\tau_3$, which practically leaves the level 3 empty ($N_3 \approx 0$), it is reduced to two equations:

$$\begin{aligned}\frac{dN_1}{dt} &= -\frac{I_p}{W_p}N_1 + \frac{N_2}{T_1} \\ \frac{dN_2}{dt} &= \frac{I_p}{W_p}N_1 - \frac{N_2}{T_1}\end{aligned} \tag{C.12}$$

By taking the difference of the two equations above and setting $\Delta N = N_2 - N_1$, a differential equation for the population inversion is given by

$$\begin{aligned}\frac{d\Delta N}{dt} &= -\frac{2I_p}{W_p}N_1 - \frac{2}{T_1}N_2 \\ &= -\frac{2I_p}{W_p}\Delta N + \frac{2I_p}{W_p}N_2 - \frac{2}{T_1}N_2 \\ &= -\frac{2I_p}{W_p}\Delta N + \frac{2I_p}{W_p}\left(1 - \frac{W_p}{I_p T_1}\right)N_2 \\ &= -\frac{2I_p}{W_p}\Delta N + \frac{2I_p}{W_p}\Delta N_e\end{aligned} \tag{C.13}$$

where $\Delta N_e = N_2^{s.s} - N_1^{s.s}$ is the steady-state population inversion. To find ΔN_e, the left-hand side in Eq. (C.12) is set equal to zero and the fact that the total population is conserved, i.e $N_{tot} = N_1 + N_2$ is invoked. A relation between the total population and the steady-state population inversion is found as

$$\Delta N_e = \left(\frac{1 - \frac{W_p}{I_p T_1}}{1 + \frac{W_p}{I_p T_1}}\right) N_{tot} \tag{C.14}$$

The solution of Eq. (C.13) is

$$\Delta N(t) = (\Delta N_0 - \Delta N_e)e^{-\frac{2I_p}{W_p}t} + \Delta N_e \tag{C.15}$$

with ΔN_0 is the initial population inversion which is determined by the final value in the previous region.

Region II: Between pulses inside a bunch

Between pulses inside a bunch, $I = 0$. However, the slow decay rate of the level 2 does not contribute to the population dynamics during the pulse period, i.e. $\tau_{FP}/T_1 \ll 1$, which eliminates the terms proportional to $1/T_1$ in Eq. (C.11). Then, the rate equation is reduced to

$$\begin{aligned}
\frac{dN_1}{dt} &= -\frac{I_p}{W_p}(N_1 - N_3) \\
\frac{dN_2}{dt} &= \frac{N_3}{\tau_3} \\
\frac{dN_3}{dt} &= \frac{I_p}{W_p}(N_1 - N_3) - \frac{N_3}{\tau_3}
\end{aligned} \tag{C.16}$$

The first and last equation make a simple system of first-order differential equations that can be solved analytically:

$$\dot{N}_1 = -\frac{I_p}{W_p}N_1 + \frac{I_p}{W_p}N_3 \tag{C.17}$$

$$\dot{N}_3 = \frac{I_p}{W_p}N_1 - \left(\frac{I_p}{W_p} + \frac{1}{\tau_3}\right)N_3 \tag{C.18}$$

Rearranging Eq. (C.17) gives the solution form of N_3,

$$N_3 = \frac{W_p}{I_p}\dot{N}_1 + N_1 \tag{C.19}$$

Our task now is to find the solution for N_1. By taking the derivative on both sides of Eq. (C.17) and using Eq. (C.18) and Eq. (C.19), one can obtain the equation for N_1,

$$\ddot{N}_1 + (\alpha + \beta)\dot{N}_1 + \frac{\alpha\beta}{2}N_1 = 0 \tag{C.20}$$

where

$$\alpha = 2I_p/W_p \tag{C.21}$$

$$\beta = 1/\tau_3 \tag{C.22}$$

The solution of Eq. (C.20) has a form of

$$N_1(t) = Ae^{m_1 t} + Be^{m_2 t} \tag{C.23}$$

with

$$m_{1,2} = \frac{-(\alpha+\beta) \pm \gamma}{2} \tag{C.24}$$

$$\gamma = \sqrt{\alpha^2 + \beta^2} \tag{C.25}$$

The initial condition, $N_1(0) \equiv N_{10} = A + B$, gives

$$A = N_{10} - B \tag{C.26}$$

where N_{10} is determined by the final value from the previous region. Substituting into Eq. (C.19), the solution for N_3 is obtained:

$$N_3(t) = \frac{2}{\alpha}\left[m_1 A e^{m_1 t} + m_2 B e^{m_2 t}\right] + Ae^{m_1 t} + Be^{m_2 t} \tag{C.27}$$

With the initial condition,

$$N_3(0) \equiv N_{30} = \left(\frac{2}{\alpha} + 1\right) A + \left(\frac{2}{\alpha} m_2 + 1\right) B, \tag{C.28}$$

and Eq. (C.26) gives

$$B = \frac{1}{m_2 - m_1}\left[\frac{\alpha}{2} N_{30} - \left(\frac{\alpha}{2} + m_1\right) N_{10}\right] \tag{C.29}$$

Finally, using the conservation of population, N_2 is obtained:

$$N_2(t) = N_{tot} - N_1 - N_3 \tag{C.30}$$

Case III: For the duration of the pulse

During the pulse duration, the spontaneous rate T_1 of the upper level has negligible contribution to the population dynamics. Furthermore, since $\tau_p \ll \tau_3$ for which the

population dynamics is dominantly driven by the pulse energy, the variation of the pulse intensity can be neglected. In this case, the pulse energy, $W = \int I(t)dt$, is a relevant parameter. Integrating Eq. (C.9) over the pulse duration gives[1],

$$\begin{aligned}
\Delta N_1 &= \frac{W}{W_s}(N_{20} - N_{10}) - \frac{I_p}{W_p}(N_{10} - N_{30})\tau \\
\Delta N_2 &= -\frac{W}{W_s}(N_{20} - N_{10}) + \frac{N_{30}\tau}{\tau_3} \\
\Delta N_3 &= \frac{I_p}{W_p}(N_{10} - N_{30})\tau - \frac{N_{30}\tau}{\tau_3}
\end{aligned} \tag{C.31}$$

where ΔN_1, ΔN_2 and ΔN_3 are the changes in population of the levels induced by a pulse of duration τ and energy W, N_{10}, N_{20} and N_{30} are the values of N before the pulse's arrival. Note that the equations still satisfy the conservation of total population; $\Delta N_1 + \Delta N_2 + \Delta N_3 = 0$. To calculate the time-dependent gain, only the first two equations are required. Since the gain varies linearly in time

$$G(t) = \sigma \Delta z \left[\left(N_{20} + \frac{\Delta N_2}{\tau} t \right) - \left(N_{10} + \frac{\Delta N_1}{\tau} t \right) \right], \tag{C.32}$$

the change in intensity is

$$\Delta I(t) = G(t) I_0 = \sigma I_0 \Delta z \left[\left(N_{20} + \frac{\Delta N_2}{\tau} t \right) - \left(N_{10} + \frac{\Delta N_1}{\tau} t \right) \right] \tag{C.33}$$

The intensity is then given as

$$I(t, \Delta z) = I(t, 0) + \Delta I(t) = I_0 e^{(t/\tau)^2} + \Delta I(t) \tag{C.34}$$

Eq. (C.34) indicates that the time-dependent gain shifts the center of gravity of

[1]Integration is run over the full period of the pulse which is approximately 4 times longer than the intensity FWHM. Integration over the intensity FWHM will result in $\sim 25\%$ less energy.

a pulse given as

$$\begin{aligned}\langle t\rangle &= \frac{\int_{-\infty}^{\infty} tI(t,\Delta z)dt}{\int_{-\infty}^{\infty} I(t,\Delta z)dt} \\ &= 0 + \frac{\int_{-\infty}^{\infty} t\Delta I(t)dt}{\int_{-\infty}^{\infty} I(t,\Delta z)dt} \\ &\approx \frac{\sigma I_0 \Delta z(\Delta N_2 - \Delta N_1)}{W}\int_{-\tau/2}^{\tau/2}\frac{t^2}{\tau}dt \\ &= \frac{\sigma I_0 \Delta z(\Delta N_2 - \Delta N_1)2\tau^2}{3W} \\ &= \frac{2\sigma\Delta z(\Delta N_2 - \Delta N_1)\tau}{3}\end{aligned} \tag{C.35}$$

One can substitute the values of ΔN_1 and ΔN_2 from Eq. (C.31). The numerator in Eq. (C.35) should be equal to the energy lost by the medium: $\Delta W = -(\Delta_2 - \Delta_1)/2(\hbar\omega)$. The time shift is simply $\langle t\rangle = 2\tau\Delta W/3W$.

This time shift is a fraction of the pulse duration, and therefore can be quite large if the inversion is large. The size of the inversion depends on τ_3. The inversion is largest if $\tau_3 = 0$, and that makes also the largest shift of $\langle t\rangle$. If τ_3 is larger than the interpulse period, or even as large as the nanosecond pulse bunch, but smal compared to the cavity round-trip time, the gain recovery will vary along the pulse train, causing a decrease in the value of $|\langle t\rangle|$. With realistic values of the parameters, Eq. (C.31) shows that ΔN_1 is positive, and ΔN_2 is negative.

References

[1] VM Baev, T. Latz, and PE Toschek. Laser intracavity absorption spectroscopy. *Applied Physics B: Lasers and Optics*, 69(3):171–202, 1999.

[2] A. Schmitt-Sody, K. Masuda, A. Velten, and J.C. Diels. Intracavity mode locked laser magnetometer. *Optics Communications*, 283(17):3339–3341, 2010.

[3] R Wynands, A Nagel, S Brandt, D Meschede, and A Weis. Selection rules and line strengths of zeeman-split dark resonances. *Physical Review A*, 58(1):196, 1998.

[4] Y.Y. Jau, E. Miron, AB Post, NN Kuzma, and W. Happer. Push-pull optical pumping of pure superposition states. *Physical review letters*, 93(16):160802, 2004.

[5] Daniel A Steck. Rubidium 87 d line data, 2001.

[6] Norman C. Peterson, Michael J. Kurylo, Walter Braun, Arnold M. Bass, and Richard A. Keller. Enhancement of absorption spectra by dye-laser quenching. *J. Opt. Soc. Am.*, 61(6):746–750, Jun 1971.

[7] T. Hansch, A.L. Schawlow, and P. Toschek. Ultrasensitive response of a cw dye laser to selective extinction. *Quantum Electronics, IEEE Journal of*, 8(10):802–804, 1972.

[8] John David Jackson. *Classical electrodynamics*. Wiley, New York, NY, 3rd ed. edition, 1999.

[9] Anthony E. Siegman. *Lasers*. University Science Books, 1986.

[10] J. Ye and S.T. Cundiff. *Femtosecond optical frequency comb: principle, operation, and applications*. Springer Verlag, 2005.

[11] Magnus W Haakestad, Tobias P Lamour, Nick Leindecker, Alireza Marandi, and Konstantin L Vodopyanov. Intracavity trace molecular detection with a broadband mid-ir frequency comb source. *JOSA B*, 30(3):631–640, 2013.

[12] L. Arissian and J.C. Diels. Investigation of carrier to envelope phase and repetition rate: fingerprints of mode-locked laser cavities. *Journal of Physics B: Atomic, Molecular and Optical Physics*, 42(18):183001, 2009.

[13] A. Velten, A. Schmitt-Sody, and J.C. Diels. Precise intracavity phase interferometry in an optical parametric oscillator with two pulses per cavity round trip. *Optics letters*, 35(8):1181–1183, 2010.

[14] Dmitry Budker and Michael Romalis. Optical magnetometry. *Nature Physics*, 3(4):227–234, 2007.

[15] H. G. Dehmelt. Modulation of a light beam by precessing absorbing atoms. *Phys. Rev.*, 105:1924–1925, Mar 1957.

[16] William E. Bell and Arnold L. Bloom. Optical detection of magnetic resonance in alkali metal vapor. *Phys. Rev.*, 107:1559–1565, Sep 1957.

[17] William E Bell and Arnold L Bloom. Optically driven spin precession. *Physical Review Letters*, 6(6):280, 1961.

[18] M. Stähler, S. Knappe, C. Affolderbach, W. Kemp, and R. Wynands. Picotesla magnetometry with coherent dark states. *EPL (Europhysics Letters)*, 54:323, 2001.

[19] Peter D. D. Schwindt, Svenja Knappe, Vishal Shah, Leo Hollberg, John Kitching, Li-Anne Liew, and John Moreland. Chip-scale atomic magnetometer. *Applied Physics Letters*, 85(26):6409–6411, 2004.

[20] JC Allred, RN Lyman, TW Kornack, and MV Romalis. High-sensitivity atomic magnetometer unaffected by spin-exchange relaxation. *Physical review letters*, 89(13):130801–130801, 2002.

[21] D. Sheng, S. Li, N. Dural, and M. V. Romalis. Subfemtotesla scalar atomic magnetometry using multipass cells. *Phys. Rev. Lett.*, 110:160802, Apr 2013.

[22] Marlan O Scully and Michael Fleischhauer. High-sensitivity magnetometer based on index-enhanced media. *Physical review letters*, 69(9):1360–1363, 1992.

[23] D.A. Steck. Cesium d line data. *Los Alamos National Laboratory (unpublished)*, 2003.

[24] J. P. Marangos. Electromagnetically induced transparency. *Journal of Modern Optics*, 45(3):471–503, 1998.

[25] E. Arimondo. V coherent population trapping in laser spectroscopy. *Progress in optics*, 35:257–354, 1996.

[26] J. Vanier. Atomic clocks based on coherent population trapping: a review. *Applied Physics B: Lasers and Optics*, 81(4):421–442, 2005.

[27] A. Nagel, L. Graf, A. Naumov, E. Mariotti, V. Biancalana, D. Meschede, and R. Wynands. Experimental realization of coherent dark-state magnetometers. *EPL (Europhysics Letters)*, 44:31, 1998.

[28] A. S. Zibrov, M. D. Lukin, D. E. Nikonov, L. Hollberg, M. O. Scully, V. L. Velichansky, and H. G. Robinson. Experimental demonstration of laser oscillation without population inversion via quantum interference in rb. *Phys. Rev. Lett.*, 75:1499–1502, Aug 1995.

[29] S.E. Harris. Electromagnetically induced transparency. *Physics Today*, 50:36, 1997.

[30] Robert W Boyd and Paul Narum. Slow-and fast-light: fundamental limitations. *Journal of Modern Optics*, 54(16-17):2403–2411, 2007.

[31] Chien Liu, Zachary Dutton, Cyrus H Behroozi, and Lene Vestergaard Hau. Observation of coherent optical information storage in an atomic medium using halted light pulses. *Nature*, 409(6819):490–493, 2001.

[32] J. Vanier and C. Audoin. *The quantum physics of atomic frequency standards*. Number v. 1 in The Quantum Physics of Atomic Frequency Standards. A. Hilger, 1989.

[33] GAML Alzetta, A Gozzini, L Moi, and G Orriols. An experimental method for the observation of rf transitions and laser beat resonances in oriented na vapour. *Il Nuovo Cimento B Series 11*, 36(1):5–20, 1976.

[34] CJ Hawthorn, KP Weber, and RE Scholten. Littrow configuration tunable external cavity diode laser with fixed direction output beam. *Review of Scientific Instruments*, 72(12):4477–4479, 2001.

[35] KB MacAdam, A. Steinbach, and C. Wieman. A narrow-band tunable diode laser system with grating feedback, and a saturated absorption spectrometer for cs and rb. *American Journal of Physics*, 60:1098–1098, 1992.

[36] Carl E. Wieman and Leo Hollberg. Using diode lasers for atomic physics. *Review of Scientific Instruments*, 62(1):1–20, 1991.

[37] S Knappe, P Schwindt, V Shah, L Hollberg, J Kitching, L Liew, and J Moreland. A chip-scale atomic clock based on 87rb with improved frequency stability. *Optics express*, 13(4):1249–1253, 2005.

[38] J. Mlynek, W. Lange, H. Harde, and H. Burggraf. High-resolution coherence spectroscopy using pulse trains. *Phys. Rev. A*, 24:1099–1102, Aug 1981.

[39] T. Udem, J. Reichert, R. Holzwarth, and TW Hänsch. Absolute optical frequency measurement of the cesium d˜ 1 line with a mode-locked laser. *Physical review letters*, 82(18):3568–3571, 1999.

[40] S.A. Diddams, D.J. Jones, J. Ye, S.T. Cundiff, J.L. Hall, J.K. Ranka, R.S. Windeler, R. Holzwarth, T. Udem, and TW Hänsch. Direct link between microwave and optical frequencies with a 300 thz femtosecond laser comb. *Physical Review Letters*, 84(22):5102–5105, 2000.

[41] D. Felinto, LH Acioli, and SS Vianna. Accumulative effects in the coherence of three-level atoms excited by femtosecond-laser frequency combs. *Physical Review A*, 70(4):043403, 2004.

[42] L. Arissian and J.C. Diels. Repetition rate spectroscopy of the dark line resonance in rubidium. *Optics communications*, 264(1):169–173, 2006.

[43] C.J. Foot. *Atomic physics*. Oxford master series in physics. Oxford University Press, 2005.

[44] L. Arissian. *Dark line resonance in Rb-87 due to coherent interaction with mode-locked lasers*. PhD thesis, University of New Mexico, 2007.

[45] C. Cohen-Tannoudji, J. Dupont-Roc, and G. Grynberg. *Atom-photon interactions: basic processes and applications*. Wiley Online Library, 1992.

[46] L. Allen and J.H. Eberly. *Optical resonance and two-level atoms*. Dover Publications, 1987.

[47] *Modern Quantum Mechanics*. Pearson Education, 2006.

[48] R.W. Boyd. *Nonlinear Optics*. Nonlinear Optics Series. Elsevier Science, 2008.

[49] William Happer. Optical pumping. *Reviews of Modern Physics*, 44:169–249, 1972.

[50] M. Born and E. Wolf. *Principles of Optics: Electromagnetic Theory of Propagation, Interference and Diffraction of Light*. Cambridge University Press, 1997.

[51] F.L. Pedrotti, L.S. Pedrotti, and L.M. Pedrotti. *Introduction to Optics*. Pearson Prentice Hall, 2007.

[52] D. Budker, D.F. Kimball, and D.P. DeMille. *Atomic Physics: An Exploration Through Problems and Solutions*. Oxford University Press, 2004.

[53] MV Romalis, E. Miron, and GD Cates. Pressure broadening of rb d1 and d2 lines by 3he, 4he, n2, and xe: Line cores and near wings. *Physical Review A*, 56(6):4569, 1997.

[54] J. Vanier, M. W. Levine, D. Janssen, and M. Delaney. Contrast and linewidth of the coherent population trapping transmission hyperfine resonance line in rb-87: Effect of optical pumping. *Phys. Rev. A*, 67:065801, Jun 2003.

[55] S. Brandt, A. Nagel, R. Wynands, and D. Meschede. Buffer-gas-induced linewidth reduction of coherent dark resonances to below 50 hz. *Phys. Rev. A*, 56:R1063–R1066, Aug 1997.

[56] F. Levi, A. Godone, J. Vanier, S. Micalizio, and G. Modugno. Line-shape of dark line and maser emission profile in cpt. *The European Physical Journal D - Atomic, Molecular, Optical and Plasma Physics*, 12(1):53–59, 2000.

[57] SL McCall and EL Hahn. Self-induced transparency. *Physical Review*, 183(2):457, 1969.

[58] J.C. Diels and W. Rudolph. *Ultrashort laser pulse phenomena: fundamentals, techniques, and applications on a femtosecond time scale*. Academic Pr, 2006.

[59] F. Bloch. Nuclear induction. *Phys. Rev.*, 70:460–474, Oct 1946.

[60] Joseph Thomas Verdeyen. *Laser electronics*. Prentice Hall, Englewood Cliffs, NJ, 3 edition, 1995.

[61] RE Slusher and HM Gibbs. Self-induced transparency in atomic rubidium. *Physical Review A*, 5(4):1634, 1972.

[62] H. Giessen, A. Knorr, S. Haas, SW Koch, S. Linden, J. Kuhl, M. Hetterich, M. Grün, and C. Klingshirn. Self-induced transmission on a free exciton resonance in a semiconductor. *Physical review letters*, 81(19):4260–4263, 1998.

[63] Muhammad Anisuzzaman Talukder and Curtis R Menyuk. Self-induced transparency modelocking of quantum cascade lasers in the presence of saturable nonlinearity and group velocity dispersion. *Optics express*, 18(6):5639–5653, 2010.

[64] J.C. Diels. Light pulse propagation in homogeneously broadened amplifiers. *Physics Letters A*, 31(1):26 – 27, 1970.

[65] J.-C. Diels and E. Hahn. Pulse propagation stability in absorbing and amplifying media. *Quantum Electronics, IEEE Journal of*, 12(7):411–416, Jul 1976.

[66] A. Lipson, S.G. Lipson, and H. Lipson. *Optical Physics*. Cambridge University Press, 2010.

[67] A. Poppe, R. Holzwarth, A. Apolonski, G. Tempea, Ch. Spielmann, T.W. Hnsch, and F. Krausz. Few-cycle optical waveform synthesis. *Applied Physics B*, 72(3):373–376, 2001.

[68] F. W. Helbing, G. Steinmeyer, U. Keller, R. S. Windeler, J. Stenger, and H. R. Telle. Carrier-envelope offset dynamics of mode-locked lasers. *Opt. Lett.*, 27(3):194–196, Feb 2002.

[69] D.J. Jones, S.A. Diddams, J.K. Ranka, A. Stentz, R.S. Windeler, J.L. Hall, and S.T. Cundiff. Carrier-envelope phase control of femtosecond mode-locked lasers and direct optical frequency synthesis. *Science*, 288(5466):635–639, 2000.

[70] William Primak. Radiation-induced changes of dimensions, index of refraction, and dispersion of lithium fluoride. *Phys. Rev.*, 112:1075–1083, Nov 1958.

[71] Andrei I. Gusarov, Dominic Doyle, Alex Hermanne, Francis Berghmans, Michel Fruit, Gerd Ulbrich, and Michel Blondel. Refractive-index changes caused by proton radiation in silicate optical glasses. *Appl. Opt.*, 41(4):678–684, Feb 2002.

[72] S. Girard, J. Kuhnhenn, A. Gusarov, B. Brichard, M. Van Uffelen, Y. Ouerdane, A. Boukenter, and C. Marcandella. Radiation effects on silica-based optical fibers: Recent advances and future challenges. *Nuclear Science, IEEE Transactions on*, 60(3):2015–2036, June 2013.

[73] P.W. Milonni and J.H. Eberly. *Lasers*. Wiley Series in Pure and Applied Optics. Wiley, 1988.

[74] P. F. Moulton. Spectroscopic and laser characteristics of ti:al2o3. *J. Opt. Soc. Am. B*, 3(1):125–133, Jan 1986.